HYDROGEN EFFECTS ON DISSOLUTION OF SPENT NUCLEAR FUEL UNDER REDUCING REPOSITORY CONDITIONS—LITERATURE REVIEW AND LABORATORY EXPERIMENTS

Prepared for

U.S. Nuclear Regulatory Commission
Contract NRC–HQ–12–C–02–0089

Prepared by

Pavan K. Shukla[1]
Tae Ahn[2]
Jude McMurry[3]
Michael J. Rubal[4]
Darius Daruwalla[4]
Yi-Ming Pan[1]

[1]Center for Nuclear Waste Regulatory Analyses
San Antonio, Texas

[2]U.S. Nuclear Regulatory Commission
Washington, DC

[3]Former Employee
Center for Nuclear Waste Regulatory Analyses

[4]Southwest Research Institute®
San Antonio, Texas

October 2016

CONTENTS

FIGURES

FIGURES

Figure Page

TABLES

ACKNOWLEDGMENTS

This report was prepared to document work performed by the Center for Nuclear Waste Regulatory Analyses (CNWRA®) for the U.S. Nuclear Regulatory Commission (NRC) under Contract No. NRC–HQ–12–C–02–0089. The activities reported were performed on behalf of the NRC Office of Nuclear Material Safety and Safeguards, Division of Spent Fuel Management. The report is an independent product of CNWRA and does not necessarily reflect the views or regulatory position of NRC. The NRC staff views expressed herein are preliminary and do not constitute a final judgment or determination of the matters addressed or of the acceptability of any licensing action that may be under consideration at NRC. The authors thank David Pickett, Osvaldo Pensado, and Stuart Stothoff for technical reviews and Wesley Patrick for programmatic and editorial reviews. The authors also appreciate Arturo Ramos and Lora Neill for providing word processing support in preparation of this document.

QUALITY OF DATA, ANALYSES, AND CODE DEVELOPMENT DATA

DATA, ANALYSES AND CODES: All CNWRA-generated data contained in this report meet quality assurance requirements described in the Geosciences and Engineering Division Quality Assurance Manual. Sources of other data should be consulted for determining the level of quality of those data.

The computer software PHREEQCI (USGS, 2003) and MATLAB (MATLAB, 2008) were used in the analyses contained in this report. PHREEQCI and MATLAB are commercial software controlled under the CNWRA Technical Operating Procedure (TOP)–018, Development and Control of Scientific and Engineering Software. Documentation for experimental data, geochemistry, and dissolution rate calculations can be found in Scientific Notebooks 1022 (Jung et al., 2010); 1228E (McMurry, 2014), 1196 (Shukla et al., 2013), 1230 (Barron and Shukla, 2014), and 1250 (Poerner and Shukla, 2015).

REFERENCES:

Barron, S. and P. Shukla. "Conduct Electrochemical and Other Experiments To Determine Dissolution of SIMFUEL Under Various Conditions." Scientific Notebook 1230. San Antonio, Texas: Center for Nuclear Waste Regulatory Analyses. pp. 1–108. 2014.

Jung, H., B. Derby, R. Pabalan, and D. Pickett. "Electrochemical Measurement of Spent Nuclear Fuel (SNF) Dissolution Rate Using Simulated Spent Fuel (SIMFUEL)." Scientific Notebook 1022. San Antonio, Texas: Center for Nuclear Waste Regulatory Analyses. pp. 1–104. 2010.

McMurry, J. "Synthesis of Groundwater Test Solutions." Scientific Notebook 1228E. San Antonio, Texas: Center for Nuclear Waste Regulatory Analyses. pp. 1–36. 2014.

MATLAB. "MATLAB User's Guide." Natick, Massachusetts: The MathWorks, Inc. 2008.

Poerner, M. and P. Shukla. "Conduct Electrochemical and Other Experiments To Determine Dissolution of SIMFUEL Under Various Conditions." Scientific Notebook 1250. San Antonio, Texas: Center for Nuclear Waste Regulatory Analyses. pp. 1–70. 2015.

Shukla, P., B. Derby, and S. Barron. "Conduct Experiments To Determine Dissolution of SIMFUEL in Various Environments." Scientific Notebook 1196. San Antonio, Texas: Center for Nuclear Waste Regulatory Analyses. pp. 1–108. 2013.

USGS. "PHREEQCI v. 2.8." Reston, Virginia: U.S. Geological Survey. 2003.

EXECUTIVE SUMMARY

Dissolution of spent nuclear fuel (SNF) is an important technical issue in high-level waste (HLW) disposal. As the SNF matrix dissolves, radionuclides are released congruently. For high-solubility radionuclides such as Tc-99, C-14, Cl-36, and I-129, the radionuclide release rate is primarily determined by the SNF dissolution rate in congruency. For low-solubility radionuclides such as Pu-239 and Np-237, the release rate is primarily determined by the solubility limit, and groundwater flow rate for a given SNF dissolution rate. Therefore, in performance assessments of repository systems, the SNF dissolution rate is an important parameter needed to estimate the release to the biosphere of both high- and low-solubility radionuclides.

The dominant factors controlling the SNF dissolution rate inside a failed waste container following disposal will be the redox condition at the SNF surface, temperature, and the chemical composition of the contacting aqueous solution. The redox conditions partly depend on the dissolved oxygen plus other oxidizing species, such as hydrogen peroxide, in the aqueous solution contacting the SNF. The redox conditions also depend on reducing species such as dissolved hydrogen. The oxidizing species concentrations are affected by the radiolysis rate of the aqueous solution, whereas dissolved hydrogen concentrations predominantly depend on the anaerobic corrosion of the waste package materials, such as steel and copper. In the literature, the presence of hydrogen in the repository environment is generally referred to as a reducing condition. If the repository environment lacks oxygen, the condition is usually referred to as anoxic. If the repository environment includes predominantly oxygen, it is referred to as an oxidizing condition, regardless of whether or not hydrogen is present.

The radiolysis rate depends on alpha, beta, and gamma activity. After HLW is placed in a repository, and the repository is permanently closed, beta and gamma activities will decrease by three orders of magnitude within a few thousand years, whereas the alpha activity will persist at high levels for several hundred thousand years. Thus, oxidizing species concentrations are expected to decrease with time because of the reduction in beta and gamma activity. Literature information suggests that SNF dissolution will be significantly reduced or completely inhibited by dissolved hydrogen, even with a small amount of oxidizing species present, which could be generated by radiolysis. Furthermore, there are no systematic quantitative data in the literature on the combined effects of oxidizing species and hydrogen.

This report presents data from a literature survey and results of experimental studies on the combined effects of dissolved hydrogen and oxidizing species on SNF dissolution rates. The experiments were conducted using simulated, unirradiated SNF, commonly referred to as SIMFUEL, in reducing aqueous solutions representative of groundwater from granitic geologic media. SIMFUEL contains chemically equivalent, nonradioactive elements and a few surrogate elements representing fission products, activation products, and actinides. Hydrogen peroxide and hydrogen have been shown to be the primary radiolytic species that affect SNF dissolution after the containment period. In the experimental studies, oxygen is used as a substitute for hydrogen peroxide. To simulate radiolysis caused by highly radioactive SNF, the hydrogen and oxygen concentrations were varied in the test solutions.

The literature varies widely on the dissolution rate of SNF under reducing conditions. Some studies show that SNF dissolution rates will be completely suppressed in the presence of hydrogen, while other studies suggest that the effect is more limited. Regarding the former, there is no consensus on the level of dissolved hydrogen needed to completely suppress SNF dissolution. One set of literature data suggests that complete suppression would occur when

the dissolved hydrogen concentration is as low as 0.1 μmole/L, whereas other studies suggest that suppression occurs when the dissolved hydrogen concentration is approximately 1 mmole/L. Thus, literature varies by four orders of magnitude (i.e., 0.1 μmole/L to 1 mmole/L) on the dissolved hydrogen concentration needed to suppress SNF dissolution under reducing conditions with or without waste package corrosion products in the groundwater. Regarding the latter, there is no consensus on quantifying the effect of hydrogen on dissolution rates. On the one hand, one set of literature data indicates that dissolution rates under reducing conditions are decreased by a factor of 10 compared to oxidizing conditions. On the other hand, some studies conclude that hydrogen suppresses dissolution rates by a factor of 1,000 or more compared to oxidizing conditions. Never the less, all studies conclude that SNF dissolution would decrease under reducing conditions compared to oxidizing conditions. However, there is no agreement among the various studies on the extent to which dissolution rates are decreased.

For this study, electrochemical dissolution studies were conducted with SIMFUEL in contact with a simulated groundwater based on published reference compositions for deep groundwaters in granitic rocks at 22 ± 2 °C [72 ± 4 °F]. Experiments involved the following three SIMFUEL types: (i) pure UO_2, (ii) 35 GW-day/MTU burnup equivalent, and (iii) 60 GW-day/MTU burnup equivalent. The electrochemical experiments were conducted by immersing one of the three SIMFUEL specimens (as a working electrode) in the granitic groundwater solution, which had a near-neutral pH, bicarbonate ions, and elevated concentrations of Na^+ and Cl^- ions. The solution composition was selected to be representative of groundwater associated with a hypothetical deep geologic repository in crystalline rock. The solution was purged with various combinations of compressed air and a mixture of 4 percent hydrogen plus 96 percent nitrogen. For each SIMFUEL specimen, the electrochemical experiments were conducted under the following groundwater conditions:

1. Saturated oxygen condition by bubbling the solution with 1.02 atmg [15 psig] compressed air.

2. Saturated oxygen and hydrogen condition by bubbling the solution with 1.02 atmg [15 psig] compressed air and a 8.84 atmg [130 psig] of 4 percent H_2 plus 96 percent N_2 gas mixture.

3. Unsaturated oxygen and hydrogen condition by bubbling the solution with 0.14 atmg [2 psig] compressed air and a 1.02 atmg [15 psig] 4 percent H_2 plus 96 percent N_2 gas mixture, or with 0.70 atmg [10 psig] compressed air and a 1.02 atmg [15 psig] 4 percent H_2 plus 96 percent N_2 gas mixture.

4. Reduced oxygen and saturated hydrogen condition by bubbling the solution with a 8.84 atmg [130 psig] 4 percent H_2 plus 96 percent N_2 gas mixture.

The above conditions are identified based on the exit pressure of the gases from gas tanks and do not represent the gas pressure in the test cell. Oxygen concentration for each condition was measured, and dissolved hydrogen concentration was estimated for Conditions 2, 3, and 4. The estimated dissolved hydrogen concentration in Conditions 2 and 3 was 15.5 μmole/L, and in Condition 4 was 31 μmole/L. Electrochemical impedance spectroscopy and potentiodynamic polarization curves were used to record the electrochemical response of the working/SIMFUEL electrode for various combinations of the purging rate of gas and the solution temperature. The collected electrochemical impedance spectroscopy data were analyzed using an electrical

circuit model to estimate dissolution rates. Potentiodynamic polarization curves also were analyzed to obtain the dissolution rates.

Besides the electrochemical tests, leaching experiments were conducted to determine the dissolution rates using the leachate concentrations. The objective of these experiments was to measure the dissolution rate under the higher hydrogen fugacity (compared to 2.0×10^{-2} to 4.0×10^{-2} atm [0.29–0.59 psi] of the electrochemical tests), causing the dissolved hydrogen concentration to be near 1 mM. Such a level of dissolved hydrogen can be achieved when the fugacity of the hydrogen is near 1.3 atm [19.1 psi]. These experiments were conducted using two pipe reactors pressurized with 4 percent H_2, plus 96 percent N_2 gas mixture at approximately 30.6 atmg [450 psig].

The experimental results indicate that although dissolved hydrogen is unlikely to completely suppress SNF dissolution under reducing repository conditions, it will decrease dissolution rate of SNF compared to the oxidizing condition. Specifically, the dissolution rates decreased by one to three orders of magnitude, i.e., by a factor of 10 to 1000, under reducing conditions compared to the oxidizing condition. The decrease in dissolution rate under the reducing conditions is found to be consistent with some literature that reported a decrease by a factor of 10-1000 compared to oxidizing conditions. However, the absolute values of the dissolution rates under the reducing conditions are not sufficient to achieve the fraction release rate of 10^{-6}/year for a fragmented fuel pellet with fuel fragments sizes equivalent to 3 mm [0.12 inch] cube or less.

1 INTRODUCTION

One potential disposal option for high-level radioactive waste (HLW), including spent nuclear fuel (SNF), is to place it in a deep geologic repository. Although other options have been and continue to be considered from time to time, for at least 40 years, a deep geologic repository has been the favored disposal option by virtually all nations with commercial nuclear power plants. The United States, as well as many other countries, including Canada, Finland, France, Germany, Japan, Korea, Sweden, and Switzerland are exploring and considering deep geologic repositories to dispose of their HLW. This disposal concept typically includes an engineered barrier system (e.g., waste package and buffer) and natural barriers (i.e., geologic medium) that contribute to long-term confinement of radionuclides. In many of the repository concepts that have been proposed internationally, the waste package may consist of copper, or carbon steel canisters. The buffer, if exists, may consist of bentonite clay, whose function is to prevent or limit groundwater (which is required for significant corrosion to progress) from reaching the canisters, limit water flow rates, provide a slow diffusive transport medium that limits the migration of radionuclides from a leaking canister (Kursten et al., 2004; Swedish National Council for Nuclear Waste, 2010), and provide sorption of certain radionuclides. The engineered and natural barriers limit the ability of groundwater to reach waste packages and transport radionuclides to the biosphere.

Over the prolonged period when containment and isolation are required, the engineered barriers may fail and expose the SNF to groundwater. Failure of the engineered barriers could result in a breach of waste packages, allowing direct contact between the aqueous solution and SNF. Engineered barriers are designed to remain intact for several thousands to hundreds of thousands of years, perhaps even longer. In certain situations, however, the waste package may experience early failure due to manufacturing defects. Because of the long period between repository closure and when an engineered barrier is expected to fail, the groundwater (in a reducing environment) is not expected to contain any significant part of the initial dissolved oxygen from the ambient operating-repository atmosphere. The oxygen that would have been initially present will have been rapidly depleted within a few hundred years as a result of reaction with the waste package or buffer materials. Thus, after a few hundred years any groundwater contacting the SNF is not expected to contain any oxidizing species from the initial ambient environment (King, 2007).

After the containers fail, the SNF could dissolve in the groundwater that enters. The dominant factors controlling the SNF dissolution rate inside a failed waste container are the redox condition at the SNF surface, temperature, and the chemical composition of the contacting aqueous solution (groundwater). Redox conditions partly depend on the dissolved oxidizing species and hydrogen concentrations, which are expected to evolve with time due to radiolysis and hydrogen generated from a corrosion reaction. As the groundwater comes in proximity to the SNF, it will undergo radiolysis by alpha, beta, and gamma radiation. During the first few thousand years following disposal, when radiolysis from beta and gamma decay is effective, radiolysis of water can produce high levels of dissolved oxidizing species, such as oxygen and hydrogen peroxide. After the first few thousand years, alpha radiation is expected to dominate. During this period, the radiolysis of water will still persist, albeit at lower rates compared to the time period when beta and gamma radiation are expected to dominate. Radiolysis also will produce hydrogen in an amount equal to that of oxidizing species. However, the dominant source of hydrogen is expected to be the anaerobic corrosion of the steel or copper vessel (with steel insert), according to a reaction such as that shown in Eq. (1-1).

$$3Fe + 4H_2O \rightarrow Fe_3O_4 + 4H_2 \quad (1\text{-}1)$$

Hydrogen production by the reaction shown in Eq. (1-1) will commence as soon as groundwater contacts the HLW container. Shoesmith (2007, 2008) states that dissolved hydrogen concentrations as high as 0.038 M at approximately 49 bar [706 psi] of hydrogen partial pressure are anticipated in sealed repositories.

The SNF could dissolve in the groundwater containing oxidizing species (Ox) such as oxygen and hydrogen peroxide, according to Eq. (1-2)

$$UO_2(s) + Ox \rightarrow UO_2^{2+}(aq) + Red \quad (1\text{-}2)$$

In Eq. (1-2), the term "Red" denotes the reduced form of the dissolved oxidizing species. If the groundwater contains HCO_3^- ions, the formation of complexes between uranyl and HCO_3^- enhances the dissolution of $UO_2(s)$ even further (Grenthe et al., 1984; de Pablo et al., 1999; Grandstaff, 1976; Pierce et al., 2005; Wilson and Gray, 1990). The oxidative dissolution of both UO_2 and SNF has been studied and extensively reported in the literature (e.g., Shoesmith, 2000; Roth and Jonsson, 2008).

Literature studies indicate that dissolved hydrogen decreases the SNF dissolution rate (Shoesmith, 2007; 2008; Carbol et al., 2005). It has been suggested (Shoesmith, 2007, 2008; Trummer et al., 2009) that there are two possible pathways for H_2 to decrease the dissolution rate: (i) by consuming oxidants (Ox) in competition with UO_2 and (ii) by the reduction of oxidized UO_2, according to Eqs. (1-3) and (1-4)

$$Ox + H_2 \rightarrow Red + 2H^+ \quad (1\text{-}3)$$

$$H_2 + UO_2^{2+}(aq) \rightarrow UO_2 + 2H^+ \quad (1\text{-}4)$$

Reduction of oxidizing species by H_2 usually requires a noble-metal catalyst. Although UO_2 has little or no catalytic effect on the reduction of oxidants in the reaction shown in Eq. (1-3), the SNF matrix contains nanometer-sized clusters of noble metal fission products, such as molybdenum, ruthenium, technetium, rhodium, palladium, and tellurium. These fission products are responsible for catalyzing the reactions shown in Eqs. (1-1) to (1-3) and are often referred to as ε-particles (Shoesmith, 2007, 2008; Trummer et al., 2009). The reaction shown in Eq. (1-4) can occur in solution and on the surface of SNF. The literature states that the combined effects of the reactions in Eqs. (1-3) and (1-4) decrease the rate of fuel dissolution.

Although the details on SNF dissolution in the presence of dissolved oxidizing species and hydrogen have been widely reported in the literature, the bulk of the information does not quantify the combined effect of the oxidizing species and hydrogen. Furthermore, the literature results are not uniform and consistent. For example, reports generated by the Canadian disposal program (Shoesmith, 2007, 2008) state that a small quantity of hydrogen will completely suppress spent fuel dissolution irrespective of the oxidizing species concentration. However, information from the Swedish disposal program (Carbol et al., 2005) states that the effect is expected to be more limited. It should be noted that both Canadian and Swedish disposal programs plan deep geologic repositories in reducing conditions with copper as the waste package container material. Similarly, published corrosion potential data (Shoesmith, 2007, 2008) under various redox conditions suggest that SNF dissolution rates are also influenced by dissolved oxygen and hydrogen peroxide even in the presence of dissolved hydrogen.

The overall goal of this work was to estimate the uncertainties in the performance of waste form in modern repository designs. Specifically, the objective of this work is to identify the range of SNF dissolution rates under various oxidizing and reducing conditions, and use the dissolution rates to estimate the fractional release rates. The release rates may be used to assess performance of waste form in modern repository designs.

This report presents experimental results, together with a supporting literature review, of SNF dissolution under reducing aqueous groundwater solutions found in granitic media. The experiments were performed using SIMFUEL, which is an unirradiated, simulated SNF containing chemically equivalent nonradioactive surrogate elements for fission products, activation products, and actinides. A literature review on the effects of dissolved hydrogen on dissolution rates of the UO_2−based fuel is provided in Chapter 2. Specific objectives and the scope of the experimental study are provided in Chapter 3. Details of the experimental system and experimental results are presented in Chapter 4. Chapter 5 presents experimental data, analysis, and estimated values of dissolution rates. A summary and discussion of this work, along with conclusions and recommendations for future work, is presented in Chapter 6.

2 LITERATURE REVIEW

This chapter is organized into two parts: (1) spent nuclear fuel (SNF) dissolution rates under reducing conditions and (2) hydrogen buildup in deep geological repository systems. The first part summarizes reported SNF dissolution rates when the solution contacting the SNF contains both oxidizing species and hydrogen. This review is motivated by the fact that alpha radiolysis of water near the fuel surface will generate oxidizing species such as hydrogen peroxide. Furthermore, dissolved hydrogen will also be present in the solution, primarily due to generation of hydrogen from corrosion reactions. The literature reviewed is organized based on the following sources: (1) Canadian, (2) Swedish, (3) French, (4) European Commission, and (5) miscellaneous disposal programs. The second part of the literature review examines and documents studies focused on the buildup of hydrogen in the near field environment of a geologic repository.

2.1 Spent Nuclear Fuel Dissolution under Reducing Conditions

2.1.1 Canadian Studies

Wu et al. (2012, 2014) used a model for water radiolysis by alpha decay and the dissolution kinetics of SNF to predict the dissolved hydrogen and iron effects on SNF dissolution. The iron is simulated as ferrous ions in the groundwater from corrosion of waste package container material and steel liner within the waste package. They stated that the fuel dissolution rate is very sensitive to the dissolved ferrous ion concentration, and the hydrogen produced by the corrosion of the steel liner. Wu et al. (2012, 2014) reported that dissolved hydrogen alone can suppress SNF dissolution without ferrous ions. However, presence of ferrous ions lowered the bulk hydrogen concentration needed to suppress SNF dissolution. For CANDU fuel 1,000 years old or more, the authors stated that when the bulk iron concentration in the solution is greater than 4.2 μmol/L, even the radiolytically produced H_2 alone can completely suppress fuel corrosion, without assistance from external H_2. The ability of H_2 to decrease the fuel dissolution rate was shown to be sensitive to fuel burnup. Further, H_2 was able to completely suppress fuel dissolution at bulk H_2 concentrations on the order of 0.1 to 15 μmol/L. Wu et al. (2014) did not comment on the presence of dissolved oxidizing species. However, it appears that oxidizing species had no effect on the dissolution rates of SNF in the presence of sufficient amount of dissolved hydrogen. The kinetic model developed by Wu et al. (2012, 2014) showed that oxidizing species, produced by radiolysis, are reduced by dissolved hydrogen and ferrous ions in the solution.

Shoesmith (2007, 2008) provided a comprehensive summary of the literature on fuel dissolution rates in the presence of dissolved hydrogen. Other studies by Shoesmith and his coworkers, such as Broczkowski et al. (2005), are captured in the two references by Shoesmith (2007, 2008). The summary by Shoesmith (2007, 2008) included mechanisms to explain the ability of dissolved H_2 to decrease fuel dissolution rates. Shoesmith (2007, 2008) states that the presence of even a small amount of dissolved hydrogen will completely suppress the dissolution of SNF. Regarding the mechanisms, Shoesmith (2008) summarized that the primary reductant leading to the protection of the fuel against dissolution is the H• radical species, which can be produced by a number of activation steps depending on the composition of the fuel and the form of the radiation present. For example, a combination of γ-radiation and dissolved hydrogen can produce H• radicals on the UO_2 surface. This may involve the adsorption of gamma energy at the surface to produce high energy excitons, which decompose water to OH• and H• radical species at the fuel surface. Scavenging of OH• by the hydrogen can then create an additional H•. These radicals can then decrease the dissolution rate and

scavenge radiolytic oxidants. Similar inhibition and scavenging processes are possible when only α-radiation is present. Shoesmith (2007, 2008) also stated that in the absence of any radiation fields, experiments on SIMFUELs show that H_2 activation can occur rapidly on epsilon (ε) particles. Because these particles are galvanically coupled to the conducting UO_2 matrix, they act as anodes forcing the matrix to adopt a low potential. For either a sufficiently high extent of simulated burnup (number density of particles) at low hydrogen concentration [H_2], or a sufficiently high [H_2] at a low extent of simulated burnup, this galvanic coupling can render the UO_2 unreactive. Shoesmith (2007, 2008) states it is also possible that the UO_2 could activate H_2 in the presence of H_2O_2. However, he noted that evidence for this is weak at best. If oxidation/dissolution of the surface by H_2O_2 involves OH•, the hydroxyl species could be scavenged by reaction with H_2 and, hence, prevented from causing fuel oxidation. Shoesmith (2007, 2008) concluded that even small partial pressures of H_2 {0.1 to 1 bar [0.01 to 0.1 MPa (1.45 to 14.5 psi)]} can effectively decrease the SNF dissolution rate.

Shoesmith (2007, 2008) states that the production of H_2 will commence as soon as waste containers fail and groundwater contacts the carbon steel liner. Further, he noted that in a sealed repository, hydrogen partial pressures could be up to 50 atm [734.8 psi], and that at these levels of hydrogen partial pressures and associated dissolved [H_2], fuel dissolution could potentially decrease rapidly to zero. This suppression will be at least partially effective even for early failure when oxidizing conditions would be maintained by gamma and beta radiolysis of water. It is possible that the conditions for extremely slow chemical dissolution of fuel would be rapidly established and that dissolution and radionuclide release would be extremely slow almost from the time of container failure, irrespective of when it occurred.

Sunder et al. (1997a,b) studied the dissolution of UO_2 nuclear fuel by the products of the alpha radiolysis of water (as a function of the alpha flux and solution pH) using electrochemical techniques. The solution was purged with high purity argon to remove any dissolved oxygen. Further, Sunder et al. (1997a) used unirradiated CANDU UO_2 fuel, having a uranium isotopic composition that was the same as naturally occurring uranium, and used an external alpha source to irradiate and radiolyze the solution contacting the UO_2 electrode. The authors found that dissolution rates increase with increasing alpha dose rate, and reported a linear relationship between the dissolution rate and alpha dose rates. Sunder et al. (1997a) also reported that the corrosion potential of the UO_2 was higher in the lower pH solutions, indicating that the dissolution rate increases with decreasing pH. Because the alpha dose is expected to produce oxidizing conditions, the dissolution rates they reported indicate predominantly oxic conditions. Sunder et al. (1997a), however, did not quantify the effect of hydrogen on the dissolution rates.

2.1.2 Swedish Studies

Carbol et al. (2005) studied the effects of dissolved hydrogen on the dissolution of U-233 doped UO_2(s), high burnup spent fuel, and mixed oxide (MOX) fuel. The UO_2 samples were doped with U-233 to simulate the effects of alpha decay. Carbol et al. (2005) conducted static leaching, autoclave, and electrochemical tests to study such effects, using commercial carbonate water. They used this water because the bicarbonate ion concentration in the commercial carbonate water is comparable to the bicarbonate ion concentration in granitic groundwater. The authors used the following three fuel samples: (i) undoped UO_2, (ii) UO_2 pellets doped with 1 percent U-233, and (iii) UO_2 pellets doped with 10 percent U-233. The last two samples were used to simulate the alpha radiation field. In the static leaching tests, Carbol et al. (2005) found the following:

- For the undoped UO_2 samples under the reducing conditions, there was no significant dissolution. The authors found that the initial release occurred due to initial surface preoxidation conditions occurring before sample immersion. The initial release was observed during the first 50 days of the approximately 345-day experiment. The U-233 and U-238 concentration in the solution remained unchanged after initial dissolution (Carbol et al., 2005, Figure 2-12 and Table 2-5).

- In the case of UO_2 with 10 percent U-233 under reducing conditions, the measured concentration of the U-238 in the test solution was more than one order of magnitude higher than for undoped UO_2. Moreover, the data seem to indicate a small amount of additional dissolution after the initial release. This experiment was also conducted for approximately 345 days. The initial release occurred during the first 50 days of the experiment.

In addition, Carbol et al. (2005) reported dissolution rates of 10 percent and 1 percent U-233 doped pellets in 10 mM NaCl solution using electrochemical impedance tests [see Tables 2-12 and 2-13 in Carbol et al. (2005)]. For the 10 percent U-233 doped samples, Carbol et al. (2005) reported that the dissolution rate is approximately 35 mg/m^2/day in the solution purged with nitrogen for 162 hours, and the dissolution rate is approximately 3.4 mg/m^2/day in the solution purged with 8 percent H_2 plus 92 percent N_2 for 2,082 hours. However, for the period of approximately 162 hours, the dissolution rates under the two conditions (anoxic and reducing) are the same (close to 35 mg/m^2/day). For the 1 percent U-233 doped samples, Carbol et al. (2005) reported that the dissolution rate is approximately 8 mg/m^2/day in the solution purged with nitrogen for 600 hours, and the dissolution rate is approximately 0.2 mg/m^2/day in the solution purged with 8 percent H_2 plus 92 percent N_2 after 1,944 hours. However, the dissolution rates of the 1 percent U-233 doped samples for the same period of approximately 600 hours under the two conditions (anoxic and reducing) are close to 8 mg/m^2/day. The dissolution rate data in Carbol et al. (2005) suggest that initial rates under the anoxic and reducing conditions are same. However, the dissolution rates of the 1 and 10 percent U-233 doped pellets decrease under the reducing condition, compared to the anoxic condition, when the pellets are exposed for approximately 2,000 hours.

Carbol et al. (2005) found that the SNF dissolution rates under reducing conditions are approximately three orders of magnitude lower than those Marx (2000) measured under oxic conditions. Further, the 10 percent U-233 doped material has a dissolution rate about 10 times higher than the 1 percent U-233 doped material under the reducing conditions. The authors attributed this to the higher radiolysis in the interfacial water layers of the 10 percent doped material. Carbol et al. (2005) concluded that the purging of the solution with N_2/H_2, instead of N_2, decreases the dissolution rate by an order of magnitude in the 10 percent U-233 doped material and possibly even more in the 1 percent doped material in the long-term (approximately 2,000 hours) leaching tests.

Carbol et al. (2005) also conducted experiments with irradiated SNF and MOX fuel in the presence of dissolved H_2. The test results showed that the release rates of spent fuel components in concentrated 5 molal NaCl solutions decrease almost linearly with increasing partial pressure of hydrogen in the system, reaching release rates on the order of 10^{-9}/day [2.74×10^{-12}/year] at relatively low partial pressures of hydrogen {between 0.1 and 1 bar [0.01 and 0.1 MPa (1.45 and 14.5 psi)]}. The hydrogen solubility was in the range of 2.7×10^{-5} to 2.7×10^{-4} M at the hydrogen partial pressures between 0.1 and 1 bar [1.45 and 14.5 psi]. Carbol et al. (2005) concluded that molecular hydrogen is activated and participates in reactions with radiolytic oxidants, and thus decreases the fuel dissolution rate. Carbol et al. (2005)

quantified that 43 mM dissolved hydrogen at the hydrogen partial pressure of 53 bar [769 psi] in bicarbonate-containing solutions inhibited the oxidation and dissolution of MOX fuel, and stated that it was not possible to measure any light water reactor or MOX fuel dissolution rates. The authors stated that very low levels of hydrogen concentrations are not sufficient to completely hinder the oxidative dissolution of the fuel matrix. Carbol et al. (2005) concluded that the experimental results with α-doped UO_2, high burn-up spent fuel, and MOX fuel, together with literature data, provided justification to use fractional dissolution rates, i.e., fractional release rate, for spent fuel on the orders of 10^{-6}/yr–10^{-8}/yr with a recommended value of 4×10^{-7}/yr for dissolved hydrogen concentrations above 10^{-3} M and Fe(II) concentrations typical for European repository concepts. It is noted that 10^{-3} M of dissolved hydrogen concentration is expected at the hydrogen partial pressure of 1.28 atm [18.8 psi].

Oversby and Konsult (1999) provided a comprehensive summary of literature information on SIMFUEL, unirradiated uranium dioxide, and SNF dissolution rates under various conditions, including oxic, anoxic, and reducing conditions. Oversby and Konsult (1999) found that the SIMFUEL dissolution rates vary by a factor of 100 (0.04 to 4.6 mg/m^2/d) for conditions that should be expected to give similar dissolution rates. Oversby and Konsult (1999) stated that in many cases, it is not possible to determine whether the results are affected by oxidation on the surface of the starting materials or due to buildup of uranium in the solution (which could lower the dissolution rates). Oversby and Konsult (1999) also found that for the conditions where different dissolution rates were expected, little or no difference in the dissolution rates was found. The dissolution rates in Oversby and Konsult (1999) for unirradiated uranium dioxide seem to provide a clearer picture than those for SIMFUEL. However, ambiguities persisted concerning the effects of oxygen in the system on the dissolution rate, and on the variation of the solution chemistry at a constant bicarbonate concentration. Oversby and Konsult (1999) reported that the lowest dissolution rates were found for unirradiated UO_2 in dilute $NaClO_4$, with or without oxygen in the system. In addition, Oversby and Konsult (1999) reported lower dissolution rates under anoxic conditions with a variety of solution chemistry compared to those under oxic conditions. Oversby and Konsult (1999) reported that the lowest dissolution rates were in the range of 0.1 to 0.2 mg/m^2/day.

Trummer et al. (2008, 2009) studied radiation-induced dissolution of UO_2 in the presence of hydrogen. Trummer et al. (2008, 2009) focused on the catalytic effect of fission product noble metal inclusions on the kinetics of radiation-induced dissolution of SNF. They performed experimental studies using UO_2 pellets that contained 0, 0.1, 1, and 3 percent palladium, which was added to represent the noble fission product cluster of the SNF. The pellets were immersed in an aqueous solution containing H_2O_2 to simulate radiolytic oxidants. The solution was pressurized with hydrogen partial pressures ranging from 0 to 40 bar [0 to 4 MPa (0 to 580.2 psi)]. Trummer et al. (2008) found that the presence of hydrogen depresses the uranium dissolution rate. Trummer et al. (2008) stated that the presence of noble metal particles catalyzes H_2 oxidation which, in turn, inhibits the radiation-induced oxidizing species from oxidizing and dissolving the SNF.

Trummer et al. (2009) further studied the effect of hydrogen on radiation-induced dissolution of SNF using the same samples as in Trummer et al. (2008). The catalytic effect of palladium particles on the kinetics of radiation-induced dissolution of UO_2 during γ-irradiation in HCO_3^- containing solutions purged with N_2 and H_2 was studied in Trummer et al. (2009). The authors found that under a N_2 atmosphere, dissolution rates of the pellets with 3 percent palladium were negligible due to reduction of uranium with the radiolytically produced H_2. But, the pellets with 0–1 percent palladium dissolved at about 32 mg/m^2/day under the N_2 atmosphere. However, under a H_2 atmosphere, the dissolution rates of the pellets with 0.1 percent palladium or more

were negligible. The dissolution rate of the pellet without palladium was close to 30 mg/m^2/day under a H_2 atmosphere. Based on the experimental results, Trummer et al. (2009) concluded that the 100-year-old fuel, with a burnup of 38 GWd/MTU, will not dissolve if the hydrogen partial pressure is 0.1 bar [0.01 MPa (1.5 psi)]. This conclusion was based on the assumption that the ε-particle surface concentration is 1 percent of SNF. Trummer et al. (2009) also estimated that ε-particle surface coverage of only 1 ppm would be sufficient to completely stop the SNF dissolution at a hydrogen partial pressure of 40 bar [4 MPa (580 psi)]. Trummer et al. (2009) also reported that the noble metal particles (ε-particles) catalyze the oxidation of the UO_2 matrix by the oxidants H_2O_2 and O_2. The authors found that the increase in the rate constant for oxidative dissolution of UO_2 by O_2 is approximately 250 times greater than the uncatalyzed reaction. In summary, Trummer et al. (2008, 2009) reported that the ε-particles are responsible for accelerating dissolution under oxidizing conditions and decreasing dissolution under reducing conditions. Trummer et al. (2008, 2009) described the catalytic effects through the increases in oxidation and reduction kinetic rates. The catalytic effects described by Trummer et al. (2008, 2009) are consistent with the Wu et al. (2012, 2014) description.

Rollin et al. (2001) investigated spent UO_2 dissolution rates under oxic, anoxic, and reducing conditions. Rollin et al. (2001) used a flow-through experiment to measure the dissolution rates. Rollin et al. (2001) found that the dissolution rates are about 3 mg/m^2/day under oxidizing conditions, and dissolution occurs congruently for uranium, neptunium, barium, technetium, cesium, and strontium. These rates are valid when the solution pH is greater than 6. Under anoxic conditions, the dissolution rates were found to be the same as under oxidizing conditions. Rollin et al. (2001) found that the dissolution rates of spent fuel with H_2 (g) saturated solutions dropped by up to four orders of magnitude when compared to dissolution rates in oxidizing and anoxic conditions. Rollin et al. (2001) also stated that dissolution rates are congruent for Am-241, U-238, and Cs-137 if the pH is greater than 6, when dissolved hydrogen is present.

Trummer and Jonsson (2010) studied the effect of hydrogen on alpha-radiation-induced dissolution of UO_2-based SNF. Specifically, Trummer and Johnson (2010) focused on the impact of H_2 on the H_2O_2 concentration in an alpha-irradiated aqueous solution using a computer model. The model accounted for the effects of H_2 pressure, alpha-dose rate, and HCO_3^- concentration. The authors stated that the H_2 effect on H_2O_2 concentration is strongly alpha-dose rate dependent. Trummer and Jonsson (2010) conducted computer simulations to show that H_2 affects the H_2O_2 concentration under alpha radiolysis. The magnitude of the effect depends on the dose rate and the H_2 pressure, as well as on the concentration of HCO_3^-. Trummer and Jonsson (2010) stated that at sufficiently high hydrogen partial pressures, the H_2O_2 concentration reaches steady-state upon alpha radiolysis. Further, the critical hydrogen partial pressure required to suppress the H_2O_2 concentration during alpha radiolysis, as well as the steady-state concentration of H_2O_2, are strongly dose rate dependent. In addition, due to the alpha-radiolytic H_2 effect, i.e., H_2 produced due to water radiolysis, the steady-state concentration of H_2O_2 is lower than the H_2O_2 steady-state concentration expected in alpha-radiation-induced dissolution of SNF in the absence of H_2. Consequently, even the radiolytic H_2 will decrease the alpha-radiation-induced dissolution rate of SNF. In a final analysis, Trummer and Johnson (2010) concluded that H_2 will decrease the dissolution rate of UO_2 in the presence of alpha radiation.

2.1.3 European Commission and French Studies

Poinssot et al. (2001) reported on the effects of the radiolysis of water on the dissolution of UO_2 and irradiated fuels. Poinssot et al. (2001) discussed the work conducted by Eriksen (1995),

who studied the dissolution of fragments of irradiated fuel, with an α and β dose rate estimated at 252 Gy/hr at the fuel surface, immersed in deionized water purged with argon to remove any dissolved oxygen. As an example, a 150-hour static leach test under irradiation with measured concentrations of final O_2 of 1×10^{-7} M, H_2 of 9.6×10^{-6} M, and H_2O_2 of 6.4×10^{-7} M, produced a dissolved uranium concentration of 6.7×10^{-10} M. The authors attempted to account for the imbalance between the amount of observed oxidizing and reducing species and the oxidative dissolution rates. However, they could not establish a direct relationship between the dissolution rate of the SNF matrix and the concentrations of oxidants (produced by the radiolysis of water), including O_2, and H_2, with certainty. Poinssot et al. (2001) determined that the production of radiolytic species depended on the mass of irradiated fuel, and consumption of the species depended on the surface area of the fuel.

Another review by Poinssot et al. (2005) consisted of a combination of experimental-data-derived conclusions and modeling to determine the radionuclide source terms for SNF in geologic disposal conditions. However, the effect of hydrogen was not included in the modeling component. Poinssot et al. (2005) reported that pellets of alpha-doped uranium oxide with U-233 (1 percent or 10 percent) were evaluated by (i) static leach testing in deionized water under an atmosphere of 6 percent H_2 and 94 percent Ar, (ii) autoclave leach testing in a solution of 10 mM NaCl and 2 mM $NaHCO_3$ under varying amounts of H_2 in Ar {from 16 bar [1.6 MPa (232.1 psi)] of H_2 to eventually an all Ar environment}, and (iii) electrochemical testing in a 10 mM NaCl solution under headspace filled with 8 percent H_2 and 92 percent N_2. Results from the static leach testing and autoclave leach testing showed an initial release of uranium into the solution due to surface preoxidation of the sample prior to immersion. However, no additional uranium dissolution was observed during the course of the experiments (almost 1 year for the static test, with 6 percent H_2 plus argon, and 2 years for the autoclave test under varying amounts of H_2 in argon from 16 bar [1.6 MPa (232.1 psi)] of H_2 to eventually an all Ar environment). Poinssot et al. (2005) reported that the dissolution rates, calculated using Faraday's law for the electrochemical tests, were 1,000 times lower under the influence of hydrogen as compared to the oxic conditions that Marx et al. (2000) reported earlier.

Poinssot et al. (2005) also reported on other static leach test data of SNF (designated K8 with an average burnup of 50 GW-day/MTU) in a brine solution (5 M NaCl), under an externally applied H_2 pressure of 3.2 bar [0.32 MPa (46.4 psi)], over a 3-year period. The uranium concentrations (along with other redox-sensitive radionuclides) during this study decreased from about 10^{-6} M to about 10^{-9} M due to a reduction of their oxidized forms from the test solution. Furthermore, Poinssot et al. (2005) reported on additional autoclave leach tests of irradiated (α-dose rate of 13 Gy/s and β-dose rate of 2 Gy/s) MOX (burnup of 48 MWd/kg U) in 10 mM NaCl and 2 mM HCO_3^- under a H_2 pressure of 53 bar [5.3 MPa (769 psi)] for 494 days. As with the previous experiments Poinssot et al. (2005) reported, no dissolution rate was calculated, because no uranium was oxidized after the initial dissolution presumably from the preoxidized UO_{2+x} layer. The experimental data obtained from this project suggested the use of a dissolution fraction for spent fuel on the order of 10^{-6}/yr to 10^{-8}/yr, with a recommended value of 4×10^{-7}/yr for dissolved hydrogen above 10^{-3} M, and Fe(II) concentrations of 1×10^{-7} to 3×10^{-4} M. The Fe(II) concentrations are typical for European repository conditions.

Ferry et al. (2005, 2006) summarized the studies on the impact of hydrogen on SNF dissolution rates. Ferry et al., (2005 and 2006) conducted experiments with the UO_2-based fuel with a burnup of 43 GW-day/MTU in a solution containing 10 mM of NaCl and 2 mM of HCO_3^- under 50 bars [5 MPa (725 psi)] of hydrogen and at 25 and 70 °C [77 and 158 °F]. The measured uranium concentration of $<10^{-9}$ M in the leaching solution remained constant throughout the duration of the experiment (approximately 400 days). Thus, fuel dissolution rates were

unobtainable. The hydrogen effect was also observed at lower pressures {5 bars [0.5 MPa (73 psi)] H_2 with 0.03 percent CO_2}. Ferry et al. (2005, 2006) concluded that SNF dissolution is completely inhibited above 0.8 mmol/L of dissolved hydrogen in solution. The dissolved hydrogen concentration of 0.8 mmol/L is expected at a hydrogen fugacity of approximately 1.03 atm [15.1 psi].

Ferry et al. (2005, 2006) proposed the following two possibilities on the inhibition effect of H_2 on the SNF dissolution mechanism:

1. U(VI) generated on the fuel surface could be reduced to U(IV) in the presence of hydrogen. The reduction reaction would be catalyzed by UO_2(s) according to Eq. (2-2)

$$UO_2(CO_3)_3^{4-} + H_2 \rightarrow UO_2(s) + 2\ HCO_3^- + CO_3^{2-}\ (\text{catalyzed by } UO_2(s)) \quad (2\text{-}2)$$

2. H_2 and H_2O_2 may also recombine in a chemical chain reaction with the aid of H• and OH• radicals, according to Eqs (2-3), (2-4), and (2-5)

$$OH\cdot + H_2 \rightarrow H\cdot + H_2O \quad (2\text{-}3)$$

$$H\cdot + H_2O_2 \rightarrow OH\cdot + H_2O \quad (2\text{-}4)$$

$$H_2 + H_2O_2 \rightarrow 2\ H_2O \quad (2\text{-}5)$$

Furthermore, Ferry et al. (2005, 2006) elaborated on the work that Spahiu et al. (2004) conducted. This work investigated the effect of hydrogen on alpha radiolysis alone through static leach tests on UO_2 pellets doped with U-233 {in an H_2/Ar atmosphere, initial H_2 aqueous concentration of 10^{-2} M at a hydrogen fugacity of approximately 12.8 atm [188.1 psi]} in a solution containing 10 mM of NaCl and bicarbonate ions. The uranium concentrations measured after several months of leaching was very low, with a negligible dissolution rate, and independent of the hydrogen pressure which was in the range of 0.16 to 16 bars [0.016 to 1.6 MPa (2.3 to 232 psi)]. Thus, as described in Ferry et al. (2006), a hydrogen concentration at the hydrogen fugacity of approximately 0.16 bar [2.3 psi] effectively inhibited the oxidation of the alpha-doped UO_2 pellet exhibiting a dose rate of 680 Gy/h. The dissolved hydrogen concentration at the hydrogen fugacity of 0.16 bar [2.3 psi] is expected to be 1.25×10^{-4} M. As Ferry et al. (2006) concluded, the dissolved hydrogen consumed the oxidants produced by radiolysis (O_2) and in effect reduced the traces of U(VI) in solution to U(IV). The reductive capacity of H_2 was activated by the presence of ε-particles in irradiated UO_2(s) and the reaction of oxygen and hydrogen catalyzed at the solid surface.

Jegou et al. (2005) investigated the following two experimental conditions in the presence of an external gamma irradiation source (Co-60 = 260 Ci, ionizing radiation dose rate = 650 Gy h^{-1}) in deionized water sparged with either air or 4 percent H_2 in argon for up to 16 days:

1. Leaching experiments performed on UO_2 pellets doped with alpha emitters (Pu-238/239, 0.011 percent Pu-238, and 0.206 percent Pu-239) with an alpha activity of $0.7 Bq/g_{UO_2}$ to reproduce the evolution of the alpha activity in a spent fuel sample with a burnup of 47 GW-day/MTU and equivalent aging of 1,500 years

2. Leaching experiments on spent fuel with a burnup of 60 GW-day/MTU (designated as UOX60)

Jegou et al., (2005) deduced the following from the study. For the doped UO_2 pellets, the nature of the dissolved gas clearly had a major role on the effect of gamma radiolysis, because the presence of oxygen accelerated the decomposition of water into molecular products, such as hydrogen peroxide (H_2O_2), superoxide ion (O_2^-), and hydroperoxyl radical (HO_2). The presence of these oxidizing species in proximity to the surface is likely to oxidize UO_2, thus increasing the dissolution rate. As Jegou et al. (2005) reported, the uranium dissolution rate in the aerated medium was 83 mg/m^2/day compared to 6 mg/ m^2/day in 4 percent H_2/Ar. Furthermore, the rate drop was accompanied by a reduction of about four orders of magnitude in the hydrogen peroxide concentrations after 14 days of gamma irradiation. The experiments were conducted with air as a cover gas, and had a H_2O_2 concentration of 1.25×10^{-4} M compared to 3.4×10^{-8} M for the 4 percent H_2/Ar as a cover gas. Additionally, due to uranium/plutonium species precipitation onto the surface of the UO_2 pellets, dissolution rates could not be used to obtain matrix alteration rates under gamma irradiation. Jegou et al. (2005) also measured the dissolution rate of spent fuel (UOX60) to be 34 mg/m^2/day in the aerated medium as compared to 6.5 mg/m^2/day for the experiment conducted under a 4 percent H_2/Ar cover gas. The dissolution rates of actinides from spent fuel and doped UO_2 pellets under gamma irradiation in aerated media were identical. In addition, the quantities of H_2O_2 under gamma irradiation in aerated media were also identical. Thus, the fuel chemistry had no appreciable effect on alteration under these conditions and was predominantly a product of gamma irradiation and dissolved oxygen content.

2.1.4 Miscellaneous Studies

Johnson and Smith (2000) used a process model for SNF dissolution (called as oxidative dissolution model) to estimate the release of radionuclides from a generic engineered barrier system. The process model included the radiolytic effect of the SNF, and assumed that molecular radiolytic oxidants that are produced following canister failure react with SNF. The authors noted that essentially constant concentrations of fission products were observed when the hydrogen partial pressure was 5 MPa [725 psi]. That is to say, the dissolution rates could not be derived from the change in concentration in solution of a matrix dissolution indicator, such as Sr-90. Furthermore, uranium concentrations well below 10^{-8} M were observed, which could have indicated that the less soluble U(IV) was the dominant oxidation state in solution. Johnson and Smith (2000) noted that the mechanism may have involved scavenging of radiolytic oxidants by hydrogen or a catalytic effect of the UO_2 surface on dissolved hydrogen. The effect of dissolved hydrogen on the decreased dissolution rates of UO_2 and spent fuel was acknowledged by the authors, but the authors were unable to infer an appropriate G value (defined as molecules of H_2O decomposed per 100 electron-V of radiation energy) to be used in the oxidative dissolution model under irradiation. Therefore, a conservative value of $G \geq 0.01$ was used in the oxidative dissolution model. The authors listed model results in the form of fuel fractional release rates [see Johnson and Smith (2000) Table 2] with time. These release rates were estimated using the assumption that radiolytic oxidants react with the fuel. The estimated release rates were less than 10^{-6} /yr for both low and high burnup light water reactor SNF after 3,000 years, whereas the MOX SNF dissolution rates were less than 10^{-6} /yr after 22,000 years.

El Aamrani et al. (2007) characterized uranium sorbed onto commercial magnetite (Fe_3O_4) using x-ray photon spectroscopy (XPS), and extended x-ray absorption fine structure (EXAFS) spectroscopic techniques. Using a recirculating reactor, powdered magnetite samples were put into contact with a U(VI) solution (10^{-4} M) under a nitrogen atmosphere and acidic pH conditions [0.1 M $NaClO_4$)]. XPS analysis was conducted for samples exposed for 85 days, while EXAFS analysis was conducted for samples exposed for 30 days. While the results obtained from XPS failed to indicate the presence of reduced uranium on the magnetite surface, the results

obtained from EXAFS indicated that the uranium sorbed onto magnetite was a mixture of U(IV) and U(VI), thus confirming the capacity of magnetite to reduce U(VI) to U(IV) to some extent in acidic, anoxic conditions. The study by Aamrani et al. (2007) suggests that magnetite could reduce dissolved U and other actinides by their sorption on its surface, thereby, limiting the effect of SNF dissolution.

Duro et al. (2008) investigated the effects of anoxic and reducing environments on U(VI) solutions (with uranium initial concentrations of ~8×10^{-6} to 1.1×10^{-5} M) in the presence of solid magnetite (Fe_3O_4), the final corrosion product on SNF canisters. Solutions were continuously purged at 1 atm {0.1 MPa [14.5 psi]} with a gas mixture of N_2 and CO_2 for anoxic conditions. For reducing conditions, test solutions were purged with either H_2 or a mixture of H_2 and CO_2. The study showed that under both anoxic conditions and reducing conditions a reduction in uranium concentration, due presumably to precipitation onto the (solid) magnetite, was observed over the 25-day test period. However, unlike in the anoxic conditions, under reducing conditions the uranium concentration decreased to a greater extent. Measured redox potential values of the solution evolved toward reducing values, which corresponded to the presence of tetravalent UO_2 compounds that are essentially insoluble in groundwater. Further, an experiment was conducted by increasing the amount of magnetite (i.e., the surface/volume ratio is increased). The rate of removal of uranium from solution under these conditions, was also increased. The same is also true for the experiment in which the H_2 pressure {measured up to a $p(H_2)$ = 7.5 atm [0.76 MPa (110 psi)]} was increased. Furthermore, the increased hydrogen content resulted in a lower uranium concentration value at steady state. In summary, Duro et al. (2008) concluded that the concentration of H_2 and the surface area of magnetite contribute to the reduction of U(VI) compounds to U(IV) insoluble oxides.

Grambow et al. (2011) evaluated the reliability of existing models to assess the corrosion behavior of spent fuels in groundwater. Gambrow et al. (2011) stated that modelling of the SNF behavior under disposal conditions was usually based on the oxidative dissolution of the UO_2 matrix, where oxidative conditions produced by radiolysis were assumed. Gambrow et al. (2011) also stated that the majority of radiolytic source term models that integrated the H_2 inhibition effect did so by assuming that the H_2 consumes the oxidative species that occur in solution. Other models, as discussed next, accounted for the hydrogen effect: the Kungliga Tekniska Högskolan (KTH) model used the presence of catalytic, noble metal inclusions, and the Maksim-Trar model used reductions in corrosion potential. Gambrow et al. (2011) also claimed there was a relationship between the U(VI) dissolution and its removal via secondary phases or sorption, but Gambrow et al. (2011) had difficulty quantifying this result. Thus, as Gambrow et al. (2011) suggested, residual rates between 0.03 and 2.6 $\mu g/m^2$/day can be proposed for reducing conditions at near-neutral pH. However, data on MOX fuel were still rather limited and could not be used to realistically predict fuel performance in a repository under hydrogen-saturated and iron-rich conditions.

Ollila et al. (2013) measured dissolution rates of uranium dioxide in the presence of alpha radiation and trace elements in natural groundwaters under reducing conditions. The authors used 0, 5, and 10 percent U-233 doped UO_2 samples in contact with brackish (moderately saline) groundwater. The groundwater samples were taken from a borehole in the Olkiluoto site in Finland. The authors established the reducing conditions by using metallic iron in solution and an argon atmosphere in the glove box. The authors stated that strong reducing conditions were established by the metallic iron. The authors varied the surface area to volume ratio of the samples in the experiments, and used samples with a 5 and 15 m^{-1} [1.5 and 4.6 ft^{-1}] surface area to volume ratio. Ollila et al. (2013) reported that the effect of alpha doping was not evident in the dissolution rates for samples with lower surface area to volume ratios

($5\ m^{-1}$), but found that the dissolution rates were higher for the 10 percent U-233 doped UO_2. It was noted that samples with a higher surface area ratio also suggested the effect of alpha radiolysis under these conditions.

Loida et al. (2005) investigated the effects of hydrogen on the dissolution rates of high burnup fuel (50 GW-day/MTU). The dissolution experiments were carried out in 5.6 M NaCl solution. The authors introduced the hydrogen by pressurizing the solution with 0.0001 to 2.8 bar {1×10^{-5} to 0.28 MPa [1.45×10^{-3} to 40.6 psi]} of hydrogen. With increasing final H_2 overpressure, a slowdown of strontium, cesium, plutonium, and uranium release rates at several orders of magnitude were observed. The results of related experimental work under the external application of 3.2 bar {0.32 MPa [46.4 psi]} H_2 overpressure, revealed a slowdown of matrix dissolution, as reflected by the total Sr release. This observation was found to be supported by a very low release of fission gases (below detection limit) and low concentrations of important radionuclides, when compared to spent fuel corrosion under only an argon atmosphere.

2.2 Hydrogen Buildup

In a deep geological repository for radioactive waste, hydrogen would be generated by the anoxic corrosion of metallic components and by the radiolysis of water (King, 2007). The hydrogen generated would take the form of dissolved hydrogen. Once the solution saturates with dissolved hydrogen, excess hydrogen will form a gaseous phase that could migrate away from a waste package. The ratio between the hydrogen fugacity in an existing gas phase and the dissolved hydrogen concentration in the liquid phase is governed by Henry's Law, with a Henry's constant of approximately 125 atm/M for the ratio of the partial pressure of hydrogen in the gas phase to dissolved hydrogen concentration in the groundwater (Young, 1981).

Additional complexities arise due to the potential formation of a hydrogen gas phase in presence of a buffer material. It is energetically more favorable for a gas phase to form in bulk water (i.e., when no porous medium is present), when dissolved gas species are supersaturated (Tanaka et al., 2003). If no gas phase is present (i.e., the buffer is completely water saturated), the dissolved hydrogen will spontaneously form gas bubbles once the dissolved hydrogen concentration reaches supersaturation. Supersaturation occurs when the sum of the fugacities from all dissolved gas species (e.g., H_2, O_2, N_2, and CO_2), and the water vapor pressure, exceeds the water liquid pressure. However, gas is not physically able to enter pore spaces unless the radius of curvature of the gas–water interface is small enough to fit into the pore. Thus, a gas phase is precluded from forming in a porous medium unless the gas pressure exceeds the air entry pressure for the porous medium. The air entry pressure accounts for the pressure increase across a curved interface (it increases as the pore size decreases). The air entry pressure for cracks, fractures, and gaps is much smaller than the air entry pressure for a typical buffer or host rock porous medium, so hydrogen bubbles will preferentially form in the largest openings (e.g., inside a waste package or at surface cracks) or at the edge of a porous medium (e.g., the contact between a metal surface and the porous medium) rather than in low-permeability porous media. Hydrogen generated at a metal surface will diffuse away from the source in the water phase, reducing dissolved hydrogen buildup at the source. If hydrogen generation is sufficiently rapid, the dissolved hydrogen concentration will increase beyond the air entry pressure at some locations and hydrogen bubbles will form. As long as there is sufficient space for bubble expansion, it is energetically favorable for hydrogen to diffuse towards and into the bubble. Conversely, if the gas bubble is restrained from expanding or moving (e.g., because of low permeability of the surrounding backfill or geologic medium), both the dissolved hydrogen concentration and the gas pressure in the bubble will increase.

Eventually, either the gas pressure in the bubble becomes large enough to rupture the restraining medium (i.e., form micro-cracks or transient dilational pathways) and escape, or additional bubbles will be created at other energetically favorable locations.

Shoesmith (2007) argued that hydrogen fugacity could become as high as 50 bar [725.2 psi] in deep geological repositories. High hydrogen fugacity is commonly cited as having the beneficial effect of reducing SNF dissolution, as discussed in Section 2.1. An important aspect for determining the hydrogen concentration in groundwater, and for evaluating the effects of hydrogen on spent fuel dissolution is the extent of possible hydrogen pressure buildup and the fugacity of hydrogen in deep geological repository settings.

Bonin et al. (2000) provided a comprehensive review and analysis of various scenarios leading to the possible accumulation of hydrogen and pressure buildup in deep geological repository systems. In particular, they noted that the deep geological repository designs presently considered by many countries tend to inhibit migration of chemical species originating within the repository, by including long-lived watertight waste containers, and low permeability engineered barriers. If the repository environment becomes saturated with water, the hydrostatic pressure —and therefore the hydrogen pressure—could be approximately proportional to the depth of the repository. Thus, the design features that limit ingress of water and migration of radionuclides, also prevents hydrogen migration, and may cause the pressure to build up in the near-field.

For an actual repository, it is not clear whether the hydrostatic pressure will be proportional to the repository depth. If a repository environment is hydraulically connected to the ambient air in the repository and is not saturated with water, the hydrostatic pressure may not be proportional to the depth of the repository. In addition, geomechanical properties of the host medium and clay buffer materials (which would swell in response to resaturation) could significantly influence the potential for hydrogen pressure buildup. If the pressure reaches a sufficiently high level, then the host rock or buffer material may develop micro-cracks that could serve as pathways for gas leakage, provided they intercept regions of higher hydraulic conductivity in the host rock. Small-scale laboratory experiments conducted under the Fate of Repository Gases (FORGE) program suggest that gas-phase migration occurs through dilational pathways in the rock. However, the metrics defining travel time and breakthrough conditions are difficult to determine (Graham and Harrington, 2014). Furthermore, larger scale field experiments conducted at the Äspö Hard Rock Laboratory in Sweden do not suggest a consistent pattern of gas migration (Cuss et al., 2010). At this time, it is uncertain whether high levels of hydrogen fugacity in the near-field could be sustained for very long periods. Additional studies have been considered to review literature and estimate the pressure buildup, and hydrogen migration in deep geological repository systems.

3 OBJECTIVE AND SCOPE OF EXPERIMENTS

The objective of this work is to evaluate the effects of dissolved hydrogen and oxidizing species on spent nuclear fuel (SNF) dissolution rates. As discussed in Chapter 2, the literature information on either complete suppression or partial reduction of SNF dissolution in the presence of hydrogen is not consistent. There is no clear consensus on the concentration of dissolved hydrogen needed to completely suppress SNF dissolution under reducing conditions. For example, Wu et al. (2012, 2014) reported that 0.1 to 15 µmole/L of dissolved hydrogen is sufficient to completely suppress SNF dissolution, but Poinssot et al. (2005) and Ferry et al. (2006) concluded that approximately 1 mmole/L of dissolved hydrogen is needed for that aim. Also, literature information on the decrease in SNF dissolution rate under reducing conditions varies widely. Carbol et al. (2005) stated that SNF dissolution rates under reducing conditions are three orders of magnitude lower than under oxidizing conditions. This implies that SNF dissolution rates are on the order of 10–100 µg/m^2/day. Oversby and Konsult (1999) suggested SNF dissolution rates are in the range of 0.1 to 0.2 mg/m^2/day under reducing conditions, while Grambow et al. (2000) concluded that rates between 0.03 and 2.6 µg/m^2/day are reasonable.

Because the overall objective of this work is to evaluate the effects of dissolved hydrogen and oxidizing species on SNF dissolution rates, new experimental studies were devised and conducted. The scope of the experiments was limited to evaluating SNF dissolution rates when the dissolved hydrogen concentration is in the range of 10-30 µmole/L and the dissolved hydrogen concentration is close to 1 mmole/L. The focus of these experiments was not to replicate deep underground repository conditions; rather, it was to identify the concentrations of dissolved hydrogen needed to observe the reduction or suppression of SNF dissolution, and evaluate whether the release fraction rate for radionuclides is in the range of 10^{-6}/yr to 10^{-8}/yr under the reducing conditions.

4 EXPERIMENTAL DETAILS

Electrochemical dissolution studies were conducted with SIMFUEL in contact with simulated granitic groundwater. Experiments involve three SIMFUEL types: (i) UO_2, (ii) 35 GW-day/MTU burnup equivalent, and (iii) 60 GW-day/MTU burnup equivalent. The electrochemical experiments were conducted by immersing one of the three SIMFUEL specimens in the simulated granitic groundwater solution which is described in this chapter. The solution was purged with various combinations of compressed air and a mixture of 4 percent hydrogen plus 96 percent nitrogen. Electrochemical impedance spectroscopy and potentiodynamic polarization measurements were used to record the impedance and polarization curves of the SIMFUEL specimens at various combinations of purging rates of gas at room temperature and slightly above the atmospheric pressure. Leaching experiments were also conducted at a hydrogen fugacity of approximately 1.3 atm [19.1 psi]. This Chapter presents details concerning the (1) SIMFUEL material, (2) simulated granitic groundwater chemistry, (3) electrochemical setup and experimental procedure, and (4) SIMFUEL leaching tests.

4.1 SIMFUEL Material

The SIMFUEL samples were procured from the Korea Atomic Energy Research Institute (KAERI), which provided the following information on the fabrication of the SIMFUEL pellets. The simulated fission product powders were prepared by mixing and milling the additives of surrogate oxides in a jar containing zirconia balls and alcohol. The prepared powder mixture was added to UO_2 (natural uranium) powders, and was mixed and ball-milled again. The powder mixture was compacted and sintered at 1,730 °C [3,150 °F] for 10 hours in a flowing argon plus 4 percent H_2 atmosphere. The specifications obtained from KAERI of the pure UO_2, and SIMFUEL samples (with equivalent burnups of 35 GW-day/MTU and 60 GW-day/MTU) are listed in Table 4-1.

4.1.1 Microstructure Characterization

The microstructure of the SIMFUEL pellets was characterized using optical and scanning electron microscopy. To reveal grain boundaries and other microstructural features, the SIMFUEL samples were polished and then chemically etched by immersion for 3 minutes in an etchant composed of sulfuric acid (10 volume percent), hydrogen peroxide (20 volume percent), and distilled water (70 volume percent) at room temperature. Figure 4-1 presents reflected light optical micrographs of the UO_2, 35 GW-day/MTU burnup, and 60 GW-day/MTU burnup SIMFUEL samples. The left-hand side images (collected before etching) show the pore structure of the samples, whereas the right-hand side images (collected after etching) display the grain structure. As seen in Figure 4-1, all samples exhibited the same fine-grained microstructure with an average grain size of approximately 7.5 μm. For the SIMFUEL pellets, small-sized precipitates (approximately 1 μm in diameter) with a bright, spherical shape in Figure 4-1 were primarily distributed along the grain boundaries. It is clear that the 60 GW-day/MTU burnup SIMFUEL sample had more precipitates than the 35 GW-day/MTU burnup SIMFUEL sample. [The large oval spot in the 60 GW-day/MTU (BU60) pore image is an inclusion similar in character to the small bright inclusions.]

Figures 4-2 and 4-3 show a scanning electron micrograph and energy dispersive X-ray (EDX) spectra at certain locations of the 35 GW-day/MTU burnup SIMFUEL sample. An elemental map of the 35 GW-day/MTU burnup SIMFUEL sample is presented in Figure 4-4. Precipitates containing molybdenum, ruthenium, and palladium are evident in the elemental maps.

Table 4-1. Specification of the Fabricated SIMFUEL Pellets			
Parameter	**UO_2**	**35 GW-day/MTU**	**60 GW-day/MTU**
Density	10.70 ± 0.02 g/cm^3	10.38 ± 0.11 g/cm^3	10.31 ± 0.04 g/cm^3
Average grain size	7.6 μm	7.3 μm	7.7 μm
Oxygen/Uranium molar ratio	<2.0003	<2.0003	<2.0003
Diameter	8.30 mm	8.30 mm	8.30 mm
Length	9.04 ± 0.03 mm	9.34 ± 0.05 mm	8.70 ± 0.02 mm
Mass	5.22 ± 0.02 g	5.21 ± 0.04 g	4.78 ± 0.04 g

Figure 4-5 shows a scanning electron micrograph of the 60 GW-day/MTU burnup SIMFUEL sample, revealing a number of precipitates, as well as an EDX analysis at one precipitate location. The EDX spectrum for the second location is presented in Figure 4-6. Both precipitates A and B, mapped using EDX, primarily contain molybdenum, ruthenium, rhodium, and palladium. Elemental maps of the 60 GW-day/MTU burnup SIMFUEL sample in Figure 4-7 show precipitates containing molybdenum, ruthenium, and palladium. The elemental maps and EDX spectra confirm the presence of epsilon particles containing molybdenum and noble metals. As per the literature survey, the epsilon particles play an essential role in decreasing spent nuclear fuel (SNF) dissolution under reducing conditions. Because the SIMFUEL samples used in this study contain epsilon particles, the results are relevant.

Lucuta et al. (1991) reported a similar microstructure of SIMFUEL, showing spherical, intergranular metallic precipitates along the grain boundary. The authors found that the metallic precipitates consisted mainly of ε-phase Mo–Ru–Pd–Rh alloy, in agreement with the observations of precipitates A and B reported here for 35 GW-day/MTU (BU35) and 60 GW-day/MTU (BU60) samples (Figures 4-2, 4-3, 4-5, and 4-6). The microstructures of the SIMFUEL samples observed in this study were consistent with those from prior research on SIMFUEL by Lucuta et al. (1991), Park et al. (2008), and Jung et al. (2011).

4.1.2 Chemical Composition

There are two sources for the chemical composition of the SIMFUEL specimens: (i) Inductively Coupled Plasma Atomic Emission Spectroscopy (ICP-AES) data provided by KAERI and (ii) in-house ICP-AES confirmatory analyses. The chemical composition data on the SIMFUEL specimens from the two sources are listed in Table 4-2.

The KAERI data did not include ICP-AES analysis on the UO_2 sample. Confirmatory ICP-AES analysis of the UO_2 sample indicated that the metallic element in the sample is 100 percent uranium. KAERI stated that the impurity levels in the UO_2 powder used to prepare the specimen are below 200 ppm. Impurities were not detected in the ICP-AES analysis, even though the detectability of ICP-AES is approximately 20 ppm.

The KAERI data on the 35 GW-day/MTU and 60 GW-day/MTU samples included the initial fission product composition that was used to prepare the SIMFUEL samples and the composition obtained by ICP-AES. There is some difference between the initial fabrication composition and the ICP-AES composition measured by KAERI and the in-house confirmatory analyses. However, the difference in the initial composition and the ICP-AES data is less than

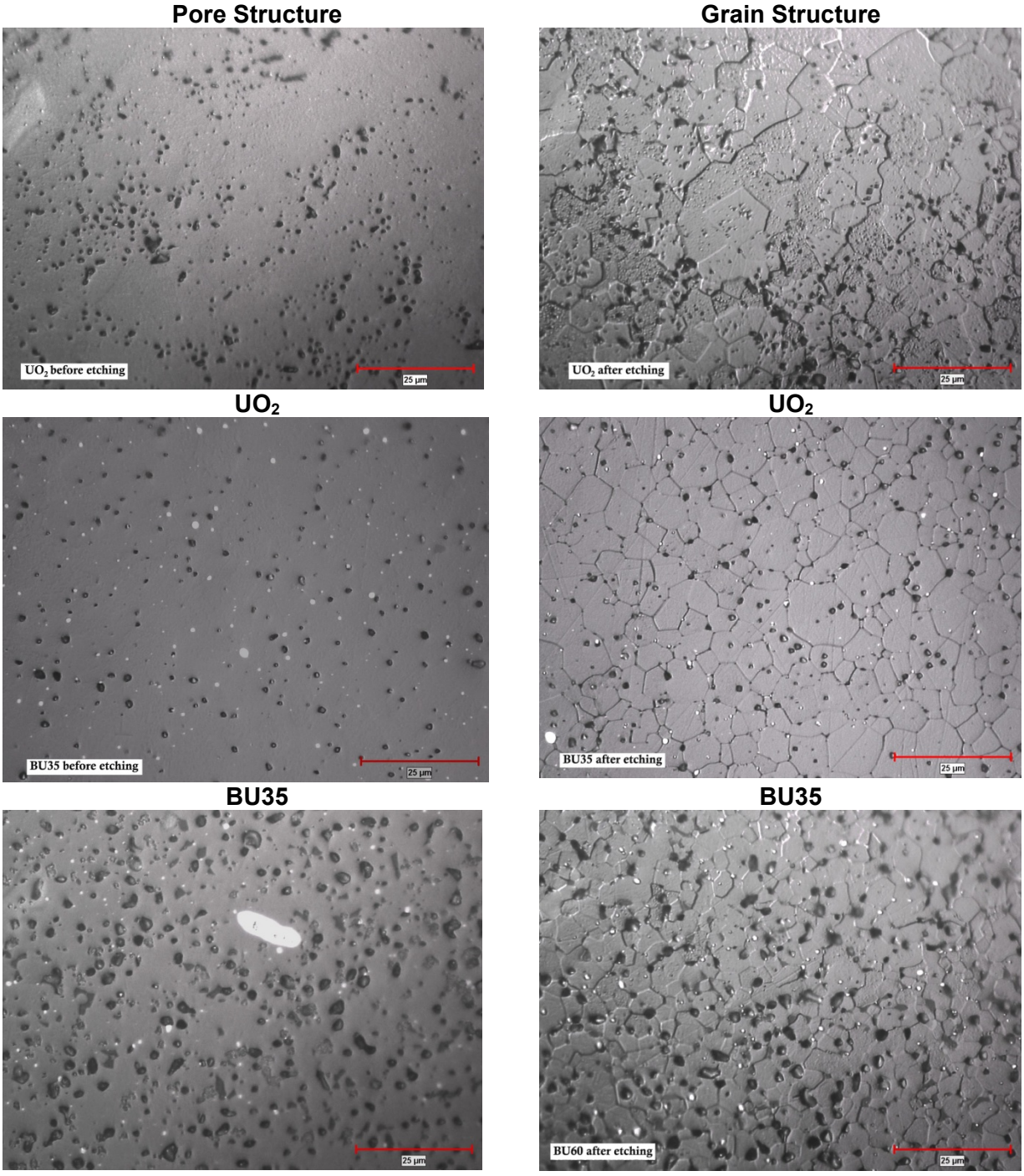

Figure 4-1. Optical Micrographs of UO_2, 35 GW-day/MTU (BU35), and 60 GW-day/MTU (BU60) SIMFUEL Samples. The Left-Hand Side Images Show the Pore Structure, and the Right-Hand Side Images Show the Grain Structure of the Samples.

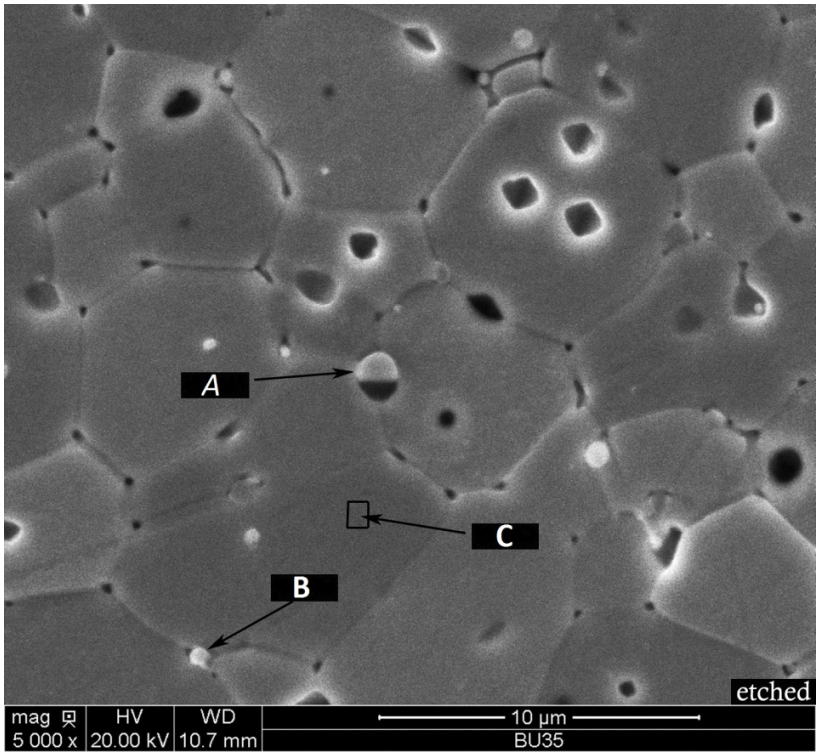

(a) Scanning Electron Micrograph of BU35 Sample

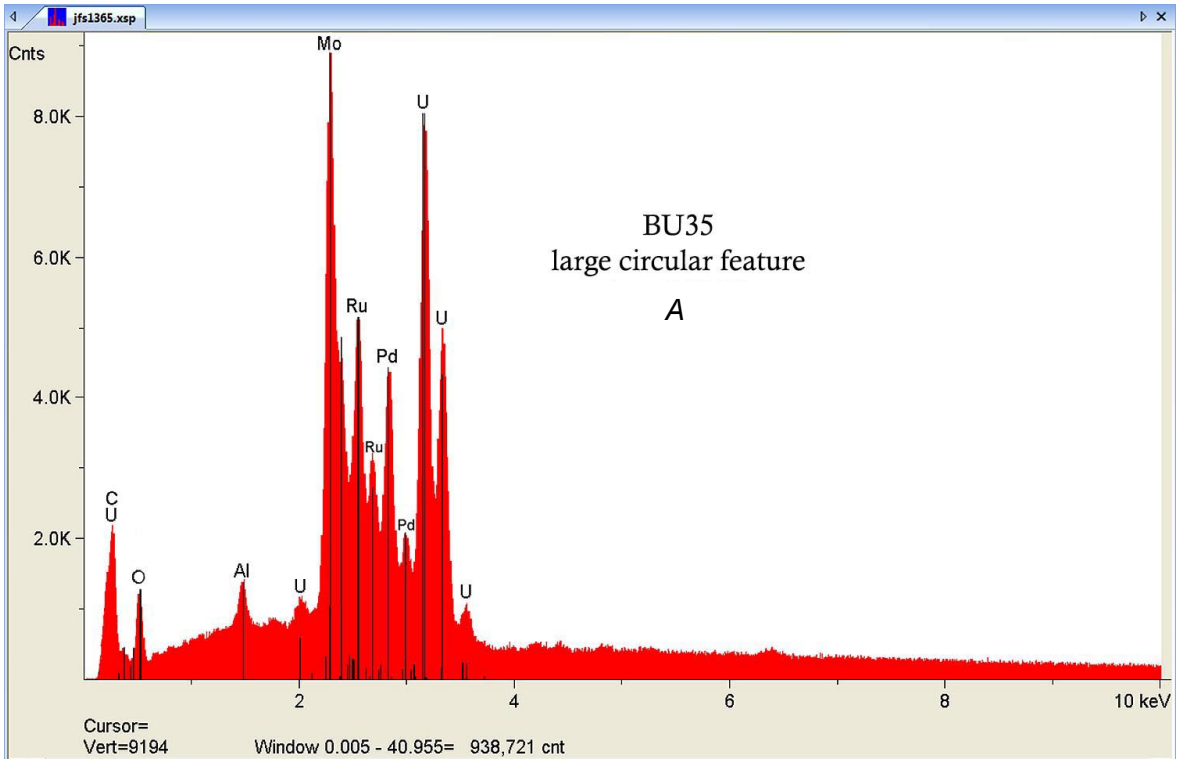

(b) EDX Spectrum at Location A

Figure 4-2. (a) Scanning Electron Micrograph of the 35 GW-day/MTU (BU35) and (b) EDX Spectrum at Location A of the SIMFUEL Sample

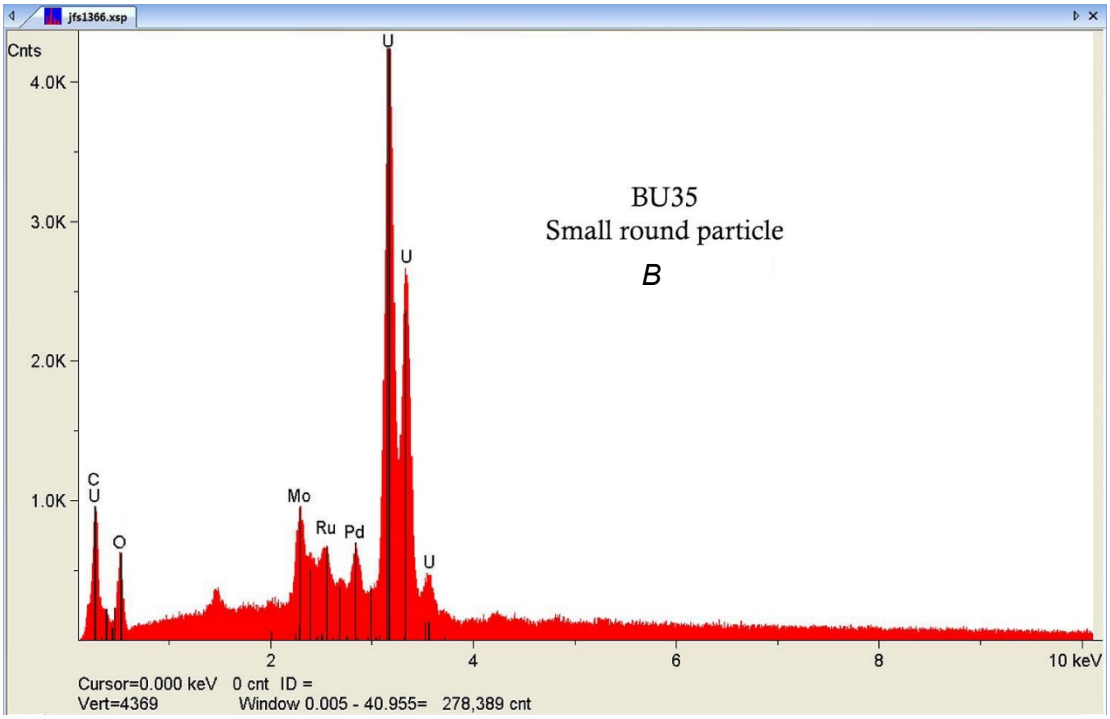

(a) EDX Spectra at Location B

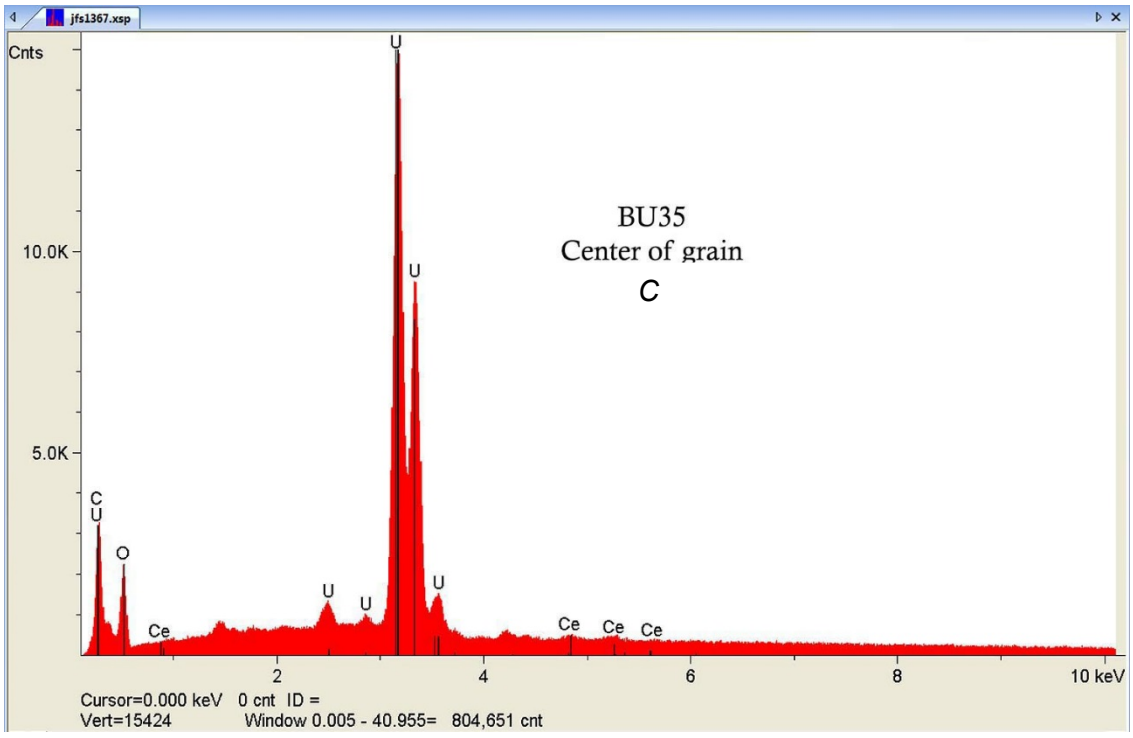

(b) EDX Spectra at Location C

Figure 4-3. EDX Spectra at Locations B and C of the SIMFUEL Sample Scanning Electron Micrograph of the 35 GW-day/MTU (BU35) Presented in Figure 4-2.

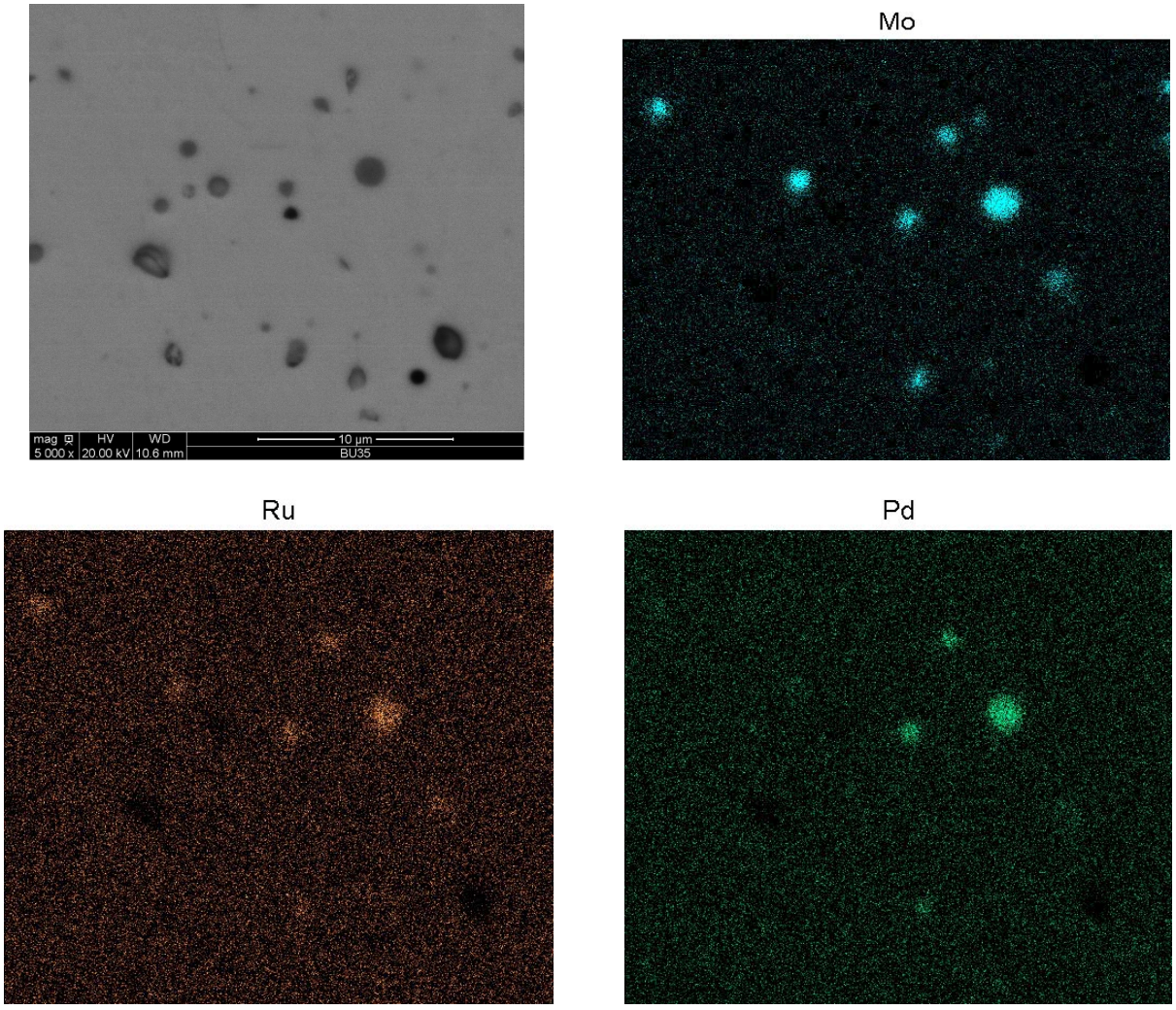

Figure 4-4. Scanning Electron Micrograph and EDX Elemental Maps [Molybdenum (Mo), Ruthenium (Ru), and Palladium (Pd)] of the 35 GW-day/MTU (BU35) SIMFUEL Sample

0.1 weight percent for all elements, except for uranium. The difference in uranium content of the initial and the ICP-AES data was approximately 0.14, and 0.3 weight percent for the 35 GW-day/MTU and 60 GW-day/MTU samples, respectively. The uranium content of the confirmatory ICP-AES data is in good agreement with the KAERI data. It is also noted that the noble metal element concentration in both 35 GW-day/MTU (BU35) and 60 GW-day/MTU (BU60) samples is above the threshold value of 0.1–3 percent reported by Trummer et al. (2009). The combined concentration of Pd, Ru, and Rh is 0.43 to 0.54 weight percent in 35 GW-day/MTU (BU35) and 0.73 to 0.92 weight percent in 60 GW-day/MTU (BU60). These concentration values for the noble metals are considered sufficient to study the effect of epsilon particles on SIMFUEL dissolution in the presence of dissolved hydrogen.

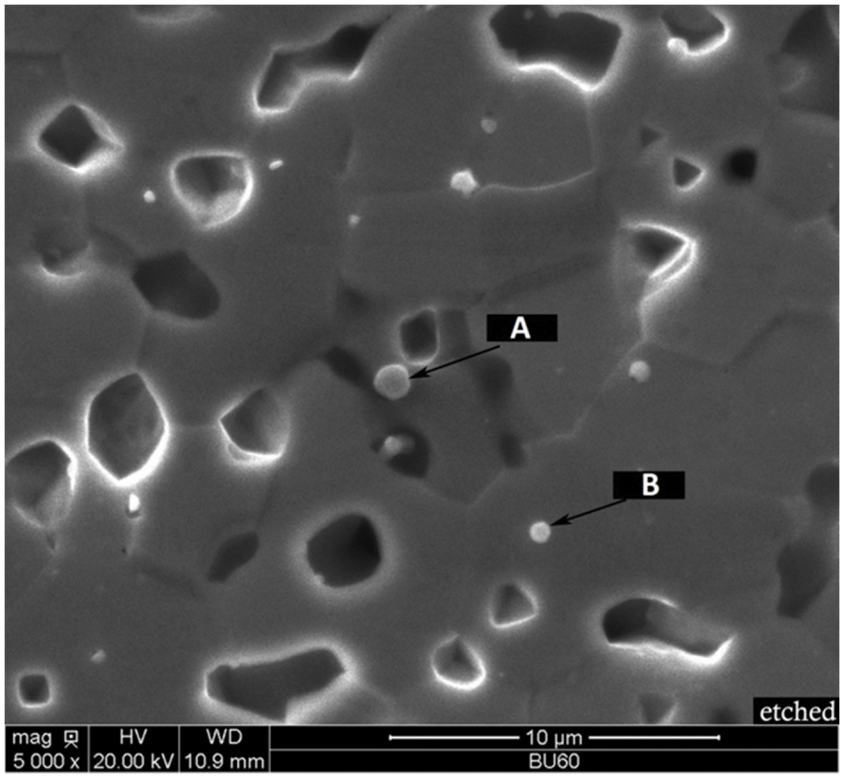

(a) Scanning Electron Micrograph of BU60 Sample

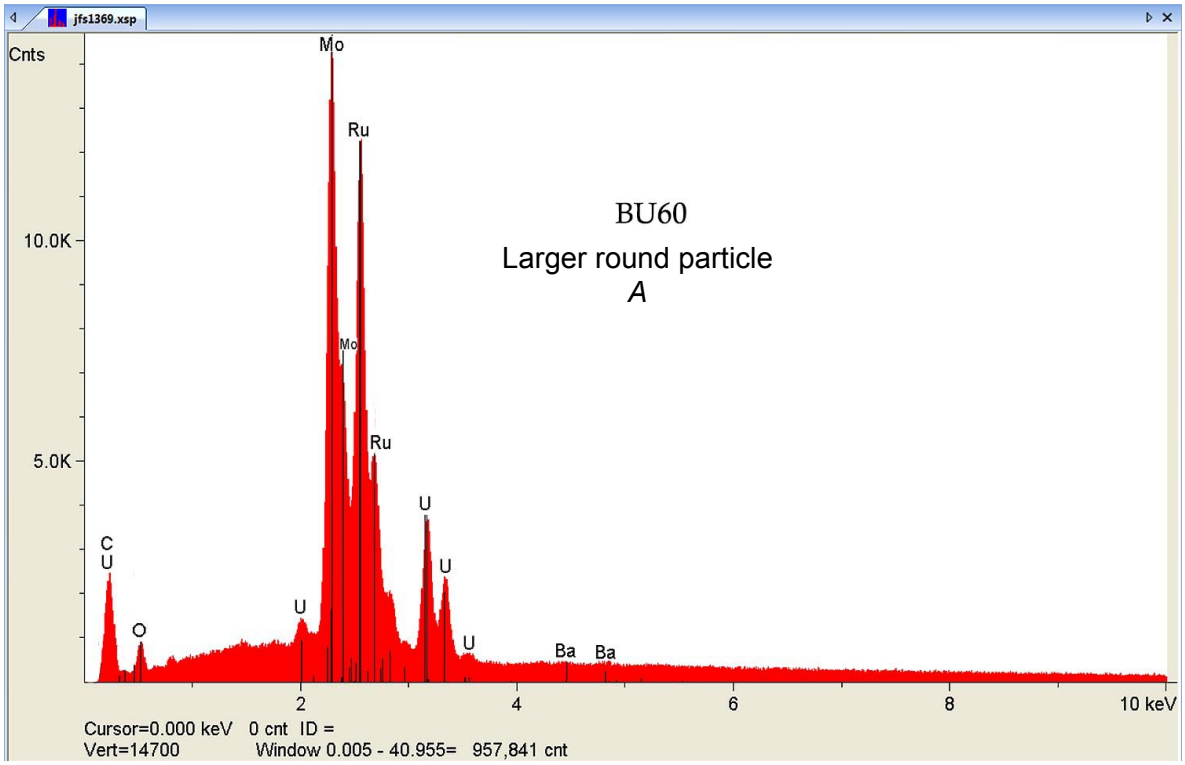

(b) EDX Spectrum at Location A

Figure 4-5. (a) Scanning Electron Micrograph and (b) EDX Spectrum at Location A in the 60 GW-day/MTU (BU60) SIMFUEL Sample

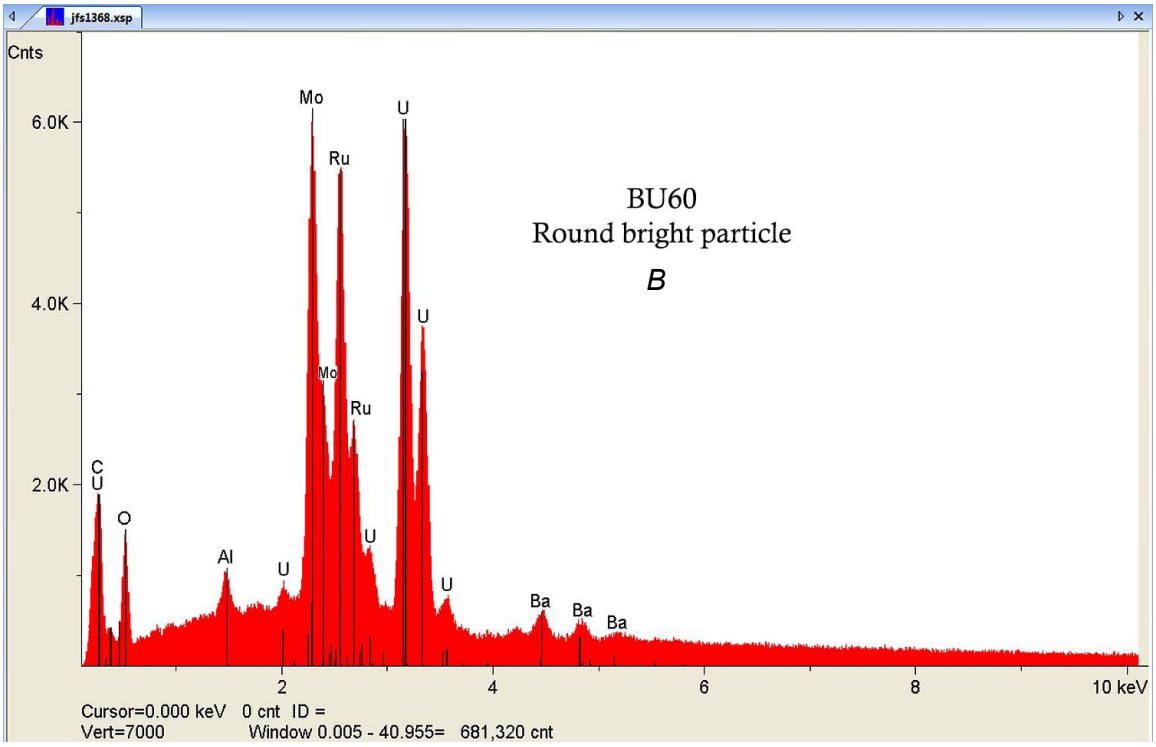

Figure 4-6. EDX Spectrum of Round Bright Particle at Location B in the Scanning Electron Micrograph of 60 GW-day/MTU (BU60) Sample Presented in Figure 4-5.

The contents of uranium measured using ICP-AES are in good agreement with the data reported in the literature for increasing SIMFUEL burnup (Lucuta et al., 1991; Rondinella et al., 1996). The reported uranium content for SIMFUEL simulating 6 percent burnup was 94.87 weight percent, which is very close to the uranium content in the 60 GW-day/MTU sample in Table 4-2. The compositions of other elements (except uranium) increase with burnup. This is also consistent with the values that Lucuta et al. (1991) and Rondinella et al. (1996) reported.

4.1.3 Electrode Preparation

The SIMFUEL specimens were used to prepare the electrodes for the electrochemical experiments. The SIMFUEL pellets were potted in hollow Teflon cylinders using a two-part epoxy material. An image of the potted electrode assembly is shown in Figure 4-8(a). The cylindrical electrode assembly was approximately 10.8 cm [4.25 in] long and 1.9 cm [0.75 in] in diameter. The surface of the SIMFUEL pellet was made flush to the Teflon cylinder as shown in Figure 4-8(b). The flushed surfaces of the pellets were exposed to the test solution during the experiments. The surface area of the electrode was approximately 0.54 cm^2 [8.4×10^{-2} in^2]. The other flat surface of the pellet in a potted electrode assembly was bonded to copper wire with a highly conductive silver epoxy. After curing the epoxy for 24 hours, the Teflon cylinder electrode assembly was ready for testing. Prior to each use of the electrode assembly, the SIMFUEL electrode was polished to a 600-grit finish, cleaned with ethanol, and dried.

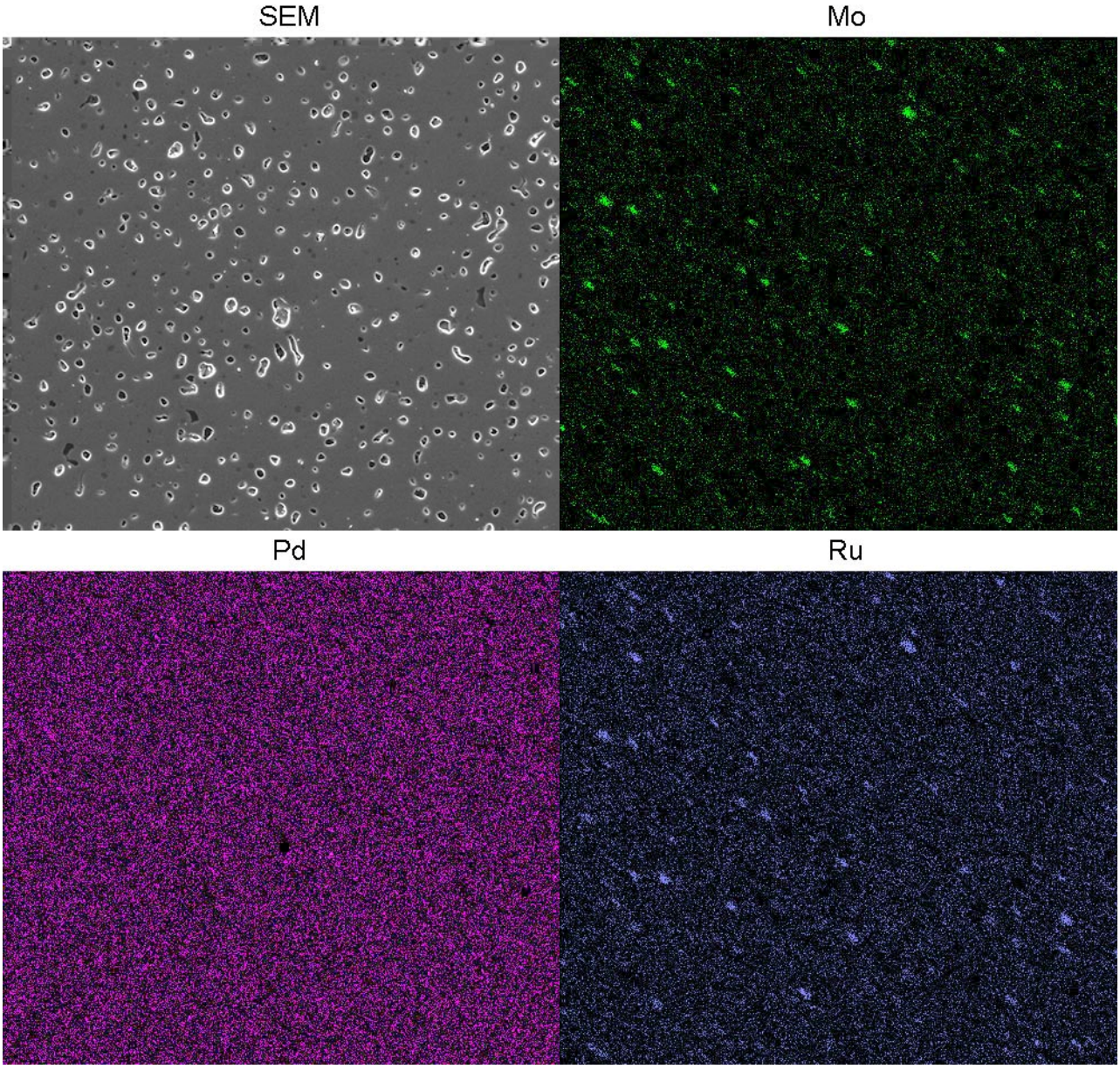

Figure 4-7. Scanning Electron Micrograph and EDX Elemental Maps [Molybdenum (Mo), Ruthenium (Ru), and Palladium (Pd)] of the 60 GW-day/MTU (BU60) SIMFUEL Sample

4.2 Simulated Granitic Groundwater Chemistry

Electrochemical dissolution studies reported here have been conducted with SIMFUEL specimens in contact with a saline simulated granitic groundwater of a near-neutral pH and elevated concentrations of Na^+ and Cl^- ions along with bicarbonate ions. The solution composition was selected to be representative of deep saline groundwater in granitic rocks, and is based on reference groundwater compositions identified in nuclear waste management research programs (McMurry, 2014). The selected solution composition is similar to the reference synthetic groundwater, identified as WN-1m, initially developed for use by the Atomic

Table 4-2. Chemical Compositions of SIMFUEL Specimens (in weight percent)								
Metallic Elements*	UO_2		35 GW-day/MTU			60 GW-day/MTU		
	Added	Confirmatory ICP-AES Analysis†	Added	ICP-AES Analysis By KAERI	Confirmatory ICP-AES Analysis†	Added	ICP-AES Analysis By KAERI	Confirmatory ICP-AES Analysis†
U	100	100	96.33	96.47	96.515	94.06	94.36	94.359
Y	—	—	0.05	0.07	0.051	0.08	0.13	0.112
La	—	—	0.13	0.12	0.132	0.22	0.21	0.224
Ce††	—	—	1.35	1.40	1.427	1.91	1.89	2.010
Nd†††	—	—	0.59	0.58	0.515	1.03	1.05	0.888
Sr	—	—	0.09	0.08	0.097	0.16	0.15	0.157
Zr	—	—	0.37	0.36	0.438	0.65	0.62	0.721
Ba	—	—	0.15	0.14	0.132	0.28	0.23	0.204
Mo	—	—	0.35	0.32	0.265	0.61	0.56	0.593
Ru††††	—	—	0.35	0.33	0.317	0.59	0.55	0.471
Rh	—	—	0.05	0.01	0.036	0.07	0.02	0.053
Pd	—	—	0.14	0.10	0.076	0.26	0.20	0.208
Te	—	—	0.05	0.01	<0.002	0.09	0.01	<0.002

*U-uranium; Y-Yttrium; La-Lanthanum; Ce-Cerium; Nd-Neodymium; Sr-Strontium; Zr-Zirconium; Ba-Barium; Mo-Molybdenum; Ru-Ruthenium; Rh-Rhodium; Pd-Palladium; Te-Tellurium;
†Confirmatory ICP-AES analysis was conducted by the Chemistry and Chemical Engineering division of Southwest Research Institute.
††Cerium (Ce) is used as surrogate element for Plutonium (Pu) and Neptunium (Np).
†††Neodymium (Nd) is used as surrogate element for Praseodymium (Pr) and Samarium (Sm).
††††Ruthenium (Ru) is used as surrogate element for Technetium (Tc).

(a) (b)

Figure 4-8. Images of the (a) Potted Electrode Assembly and (b) SIMFUEL Electrode Surface in the Potted Electrode Assembly

Energy of Canada Limited (AECL) for sorption experiments using groundwater data collected between 350 and 800 m [1,150 and 2,600 ft] below the surface in crystalline rocks of the Canadian Shield (Gascoyne, 1988). The selected solution composition also is similar to other reference deep groundwaters cited by the Nuclear Waste Management Organization (NWMO) in Canada as representative of saline conditions at a depth of 500 m [1,600 ft] or more (NWMO, 2012; McMurry, 2004).

Table 4-3 lists the calculated recipe for producing a 10× concentrate of the saline simulated groundwater test solution. The target concentration of the reference (i.e., diluted) saline simulated groundwater is compared with examples of two other deep granitic groundwaters in Table 4-4.

Table 4-3. Recipe for Preparing a 10× Concentration of Simulated Granitic Groundwater	
Reagent	**Amount of Reagent (Grams/Liter Solution)**
NaCl	38.0
KCl	0.3
Na_2SO_4	10.0
$CaCl_2 \cdot 2H_2O$	15.0
$MgCl_2 \cdot 6H_2O$	6.0
$NaHCO_3$	0.75

Table 4-4. Comparison of Three Reference Groundwaters for Deep Crystalline Rocks			
Species	**Concentration (M)**		
	Reference Simulated Groundwater (This Study)	**Synthetic Groundwater WN-1m***	**Reference Deep Groundwater CR-10†**
Na^+	8.0×10^{-2}	8.0×10^{-2}	8.0×10^{-2}
Ca^{+2}	1.0×10^{-2}	5.0×10^{-2}	5.0×10^{-2}
Mg^{+2}	3.0×10^{-3}	3.0×10^{-3}	2.5×10^{-3}
K^+	4.0×10^{-4}	4.0×10^{-4}	3.8×10^{-4}
Cl^-	9.2×10^{-2}	2.0×10^{-1}	2.0×10^{-1}
SO_4^{-2}	7.0×10^{-3}	9.0×10^{-3}	1.0×10^{-2}
HCO_3^-	8.9×10^{-4}	1.0×10^{-3}	1.1×10^{-3}
*Gascoyne, M. "Reference Groundwater Composition for a Depth of 500 m in the Whiteshell Research Area—Comparison With Synthetic Groundwater WN-1." Report AECL TR-463. Pinawa, Canada: Atomic Energy of Canada Limited. 1988. †NWMO. "Used Fuel Repository Conceptual Design and Postclosure Safety Assessment in Crystalline Rock." Pre-Project Report NWMO TR-2012-6. Toronto, Canada: Nuclear Waste Management Organization. 2012.			

As stated previously, the groundwater composition was selected to be representative of the water chemistry that generally is expected to be present at a nominal repository depth of about 500 m [1,600 ft] below the surface in crystalline bedrock such as granite. Groundwaters worldwide tend to become increasingly saline with depth (with high chloride concentrations), and they are characterized by reducing conditions. In granitic groundwaters, carbonate concentrations are variable but typically are low at nominal repository depth, and the groundwaters commonly are close to thermodynamic equilibrium with secondary mineral phases such as calcite (calcium carbonate) or gypsum (calcium sulfate). Another factor potentially influencing the water chemistry in a repository environment is the reaction of groundwater with engineered materials in the repository. Repository designs in granitic rocks that are being considered by various programs such as Canada, Sweden, and Finland, typically include the use of an engineered barrier material such as bentonite (a swelling clay product) to reduce the likelihood of advection near the waste containers. To some extent, interactions between the bentonite and the groundwater will alter the composition of near-field water contacting the container and, if the container fails, the water contacting the spent fuel waste form. For example, dissolution of minor amounts of calcite or gypsum in the bentonite may increase the concentration of carbonate or sulfate ions in the bentonite porewater, and cation exchange reactions in the bentonite may increase the concentration of sodium ions in solution while decreasing the concentration of the calcium ion. While these effects are more

pronounced in the early stages of saturation of the bentonite, gradually the near-field water evolves to a composition more similar to the surrounding groundwaters. The chemistry of the proposed test solution is expected to be within the likely range of variation for a saline groundwater that has interacted with bentonite (McMurry, 2014).

4.3 Electrochemical Setup and Experimental Procedure

The SIMFUEL dissolution experiments were conducted using a three-electrode electrochemical corrosion cell. A glass vessel was used as the container for the cell. The working electrode was one of the three electrodes that were prepared using the UO_2, the 35 GW-day/MTU, and the 60 GW-day/MTU burnup equivalent SIMFUEL pellets. The experiments used a platinum counter electrode and a saturated calomel electrode (SCE) as a reference electrode. The cell had ports for bubbling various gases through the solution.

Two 350-mL glass vessels were used as the corrosion cell in this work (Figure 4-9). The experimental data for the 35 GW-day/MTU and the 60 GW-day/MTU burnup SIMFUELs were collected using the cell depicted in Figure 4-9(a). In this cell, the electrode was placed upside down in the vessel depicted. For the cell in Figure 4-9(a), it was sometimes observed that a few gas bubbles were trapped at the SIMFUEL electrode surface and either partially or completely blocked this surface from contacting the solution. To mitigate this problem, a new glass cell design was developed as depicted in Figure 4-9(b). The SIMFUEL electrode was inserted through a side port in the cell in Figure 4-9(b). The electrode surface became vertical with respect to the cell bottom as depicted in Figure 4-9(b). This eliminated the formation and accumulation of gas bubbles at the electrode surface. The experimental data for the UO_2 SIMFUEL electrode were collected using the cell in Figure 4-9(b).

The electrochemical tests were conducted at room temperature {22 ± 2 °C [72 ± 4 °F]} in one of the two glass cells depicted in Figure 4-9. A saturated calomel reference electrode was interfaced to the test cell via a salt bridge filled with the test solution. The working, counter, and reference electrodes were interfaced with a potentiostat plus a frequency response analyzer (VMP3 model) controlled by EC-Lab software. A schematic of the test cell with the potentiostat plus frequency response analyzer and computer are depicted in Figure 4-10.

For each experiment, approximately 250 mL of the granitic water solution was poured into the glass cell so that all the electrodes were fully immersed in the solution. The dissolved hydrogen and oxygen conditions in the test solution for each experiment were controlled by bubbling compressed air and/or 4 percent H_2 plus 96 percent N_2 mixture. The bubbling rate of the gases depended on the test conditions. The inlet gases through the solution were allowed to escape through the gaps between the cell and cell head. The cell was placed inside a glovebox. Nitrogen was flowed through the glovebox to minimize intrusion of any extraneous oxygen in the test solution. An image of the corrosion cell placed inside the glovebox is presented in Figure 4-11.

Electrochemical measurements were carried out according to the following steps:

1. The working electrode was first polarized at −1 V_{SCE} for 10 minutes to cathodically remove any oxide layer at the working electrode surface.

2. The working electrode was left at the open circuit potential for 16 hours following the cathodic polarization. The potential of the working electrode with respect to the saturated calomel electrode was measured in this step.

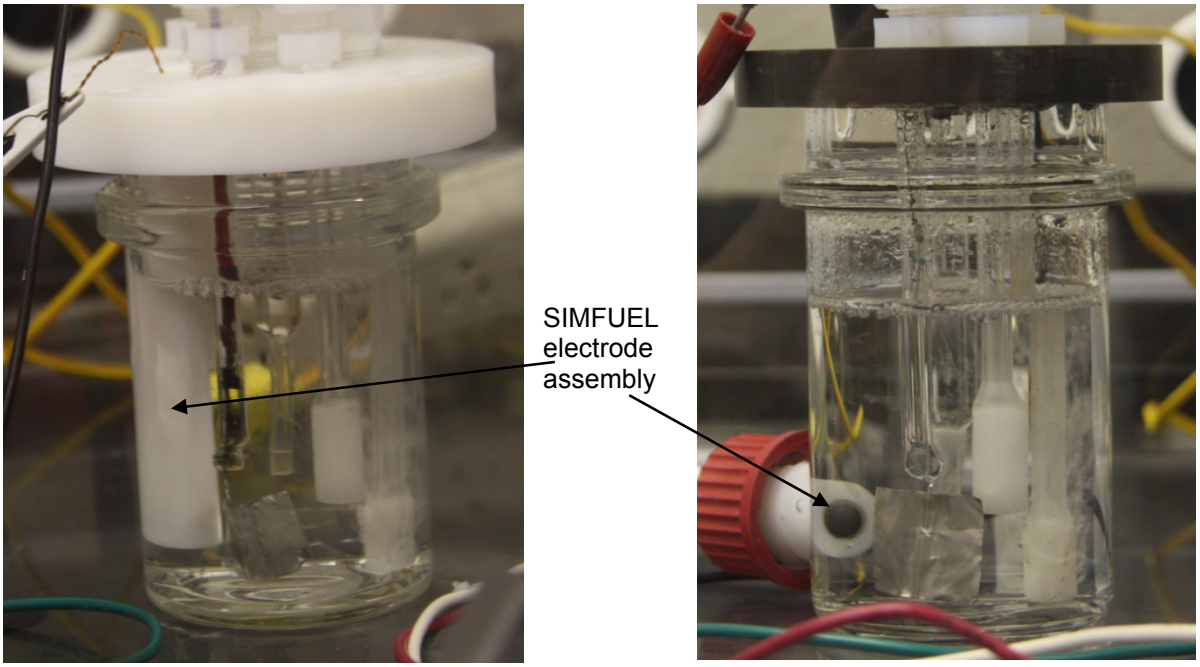

Figure 4-9. Corrosion Cells Used for the SIMFUEL Dissolution Experiments. (a) Corrosion Cell With Vertically Hanging SIMFUEL Electrode; (b) Corrosion Cell With the SIMFUEL Electrode Inserted From Side.

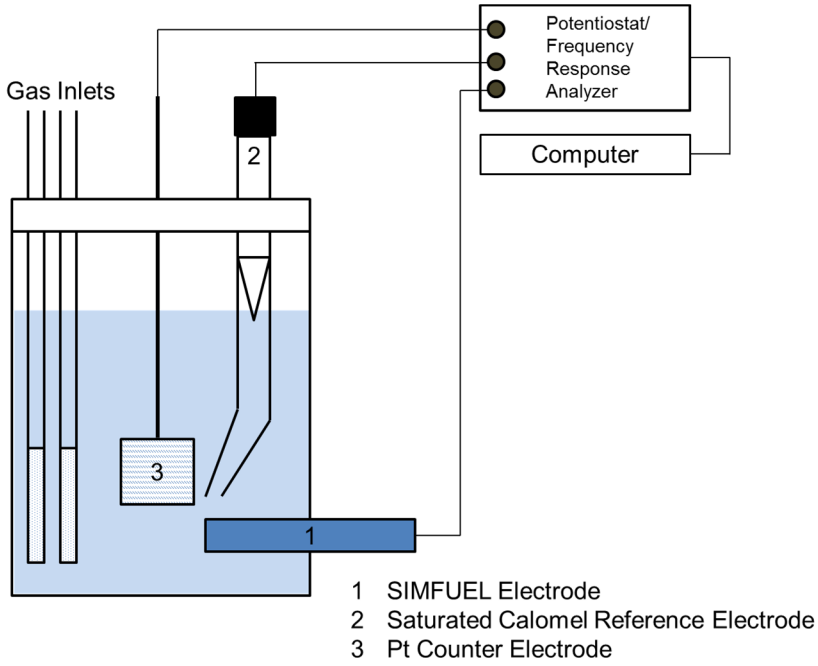

Figure 4-10. Schematic of the Test Cell With the VMP3 Potentiostat Plus Frequency Response Analyzer and Computer

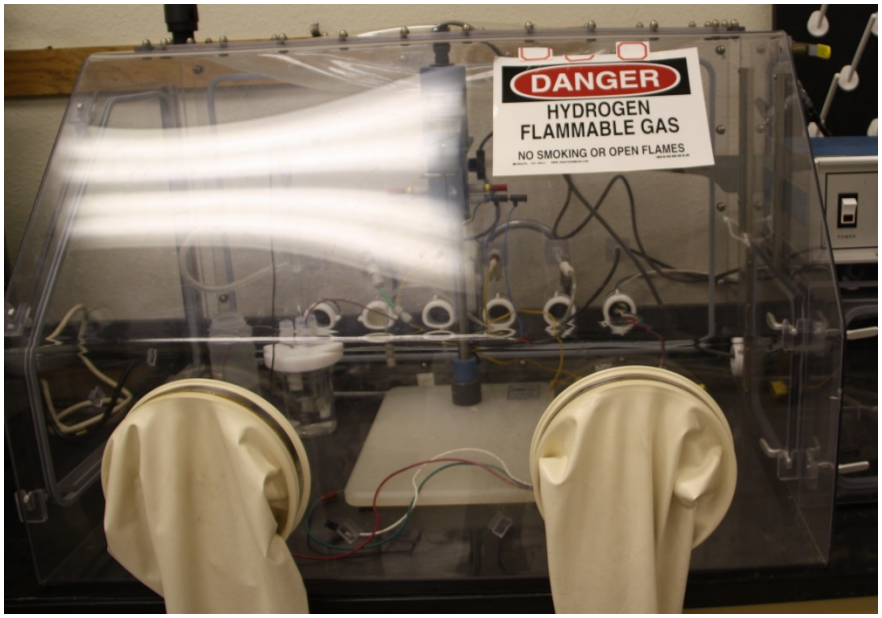

Figure 4-11. Image of the Glove Box Used in the Experiments

3. Electrochemical impedance spectroscopy (EIS) measurements were carried out in the frequency range of 100 kHz to 0.02 mHz with an alternating current voltage amplitude of 20 mV near the corrosion potential. Approximately 5–10 points were recorded per frequency decade. Only one spectrum was collected per test.

4. The open circuit potential of the working electrode continued to be measured for approximately 2–10 hours after completion of the EIS measurements.

After completion of the EIS measurements, cathodic and anodic potentiodynamic polarization measurements were conducted for some tests. For these cases, the electrode was allowed to be at the open circuit potential for 5 hours after EIS measurements were completed, and before beginning the potentiodynamic polarization measurements. Following this, the electrode was potentiodynamically polarized in the cathodic direction at 2 mV/sec with a terminal potential value of −1 V with respect to the open circuit potential. The electrode was again allowed to rest at the open circuit potential for 15 hours after completion of the cathodic potentiodynamic polarization measurements. The electrode was then potentiodynamically polarized in the anodic direction at 2 mV/sec with a terminal potential value of 0.5 V with respect to the open circuit potential. The electrode was left at the open circuit potential for several hours after completion of the anodic potentiodynamic polarization measurements.

The total exposure time for each cell was 4–6 days. After completing each experiment, three 40-mL [1.4-fl oz] samples of each test solution were taken in three glass vials. One of the samples was acidified by adding 250 µL [8.5×10^{-3} fl oz] of concentrated nitric acid and used in chemical analysis. With the remaining two samples, two sorption tests were conducted. One sorption test will be conducted using a 316 L stainless steel disk and the other with a 304 L stainless steel disk.

4.3.1 Test Matrix for Electrochemical Tests

For each SIMFUEL specimen, the electrochemical experiments were conducted under the following conditions:

1. Saturated oxygen condition by bubbling the solution with 1.02 atmg [15 psig] compressed air.

2. Saturated oxygen and hydrogen condition by bubbling the solution with 1.02 atmg [15 psig] compressed air and a 8.84 atmg [130 psig] of 4 percent H_2 plus 96 percent N_2 gas mixture.

3. Unsaturated oxygen and hydrogen condition by bubbling the solution with 0.14 atmg [2 psig] compressed air and a 1.02 atmg [15 psig] 4 percent H_2 plus 96 percent N_2 gas mixture, or unsaturated oxygen and hydrogen condition by bubbling the solution with 0.70 atmg [10 psig] compressed air and a 1.02 atmg [15 psig] 4 percent H_2 plus 96 percent N_2 gas mixture.

4. Reduced oxygen and saturated hydrogen condition by bubbling the solution with a 8.84 atmg [130 psig] 4 percent H_2 plus 96 percent N_2 gas mixture.

In Conditions 1 and 2, air was injected at the bottom of the test solution at approximately 80-90 L/minute [2.8–3.2 ft^3/minute]. In Condition 3, air was injected at approximately 5–10 L/minute [0.2–0.4 ft^3/minute] when the air discharge pressure was 0.14 atmg [2 psig]. In Condition 3, it was noticed that the air discharge flow rate fluctuated when the discharge pressure was 0.14 atmg [2 psig]. Therefore, the air discharge pressure was increased to 0.70 atmg [10 psig] for experiments conducted during fiscal year (FY) 2015. The air was injected at the flow rate of 40–50 L/min when the air discharge pressure was 0.70 atmg [10 psig] in Condition 3. In Conditions 2, 3, and 4, the 4 percent H_2 plus 96 percent N_2 gas mixture was injected at approximately 100–130 L/minute [4–4.6 ft^3/minute]. The air and 4 percent H_2 plus 96 percent N_2 gas mixture flow rates for Conditions 2 and 3 were used to control the dissolved oxygen concentrations in the test solutions.

The above conditions are identified based on the exit pressure of the gases from the gas tanks, and do not represent the gas pressure in the test cell. N_2 was used as the cover gas in the glovebox for all conditions except under the saturated oxygen condition with 1.02 atmg [15 psig] of compressed air. In Condition 1, the glovebox was left at the ambient condition. The oxygen concentration in the test solution was measured before and after completion of the experiment. However, the dissolved hydrogen concentration was not measured. The oxygen concentration was measured using the Oakton® oxygen meter.

The dissolved hydrogen concentration in the test solution was not directly measured, but it was estimated. The experiments were conducted at room temperature, and dissolved hydrogen concentration is given by Henry's law

$$C_H = k_H p_H \tag{4-1}$$

where

C_H — Dissolved hydrogen concentration [mole/L]
k_H — Henry's coefficient for hydrogen [mole/L/atm]
p_H — Partial pressure of hydrogen [atm]

k_H at room temperature is estimated to be 0.00078 mole/L/atm using the data in Young (1981). In the glovebox, the gauge pressure of the cover gas was slightly above zero. The gases were injected in the solution at higher pressure than the cover gas pressure. In addition, the volume of the glovebox is much larger than the head space in the test cell. Therefore, gas pressure in the head space is conservatively assumed to be 1 atm [14.7 psi], and the head space is assumed to be occupied by the gases injected in the solution. This head space pressure is used to estimate the dissolved hydrogen concentration in the test solution in Conditions 2, 3, and 4.

In Condition 4, the hydrogen concentration is 4 percent, the hydrogen plus nitrogen mixture (i.e., the partial pressure of hydrogen) is 0.04 atm [0.59 psi] based on the above assumptions and the corresponding C_H is estimated to be 31 μmole/L using Eq. 4-1. This value of C_H is above the threshold value of 0.1–15 μmole/L reported by Wu et al. (2012, 2014). In Conditions 2 and 3, both air and the hydrogen/nitrogen mixture were injected into the solution. For both Conditions 2 and 3, the flow rate of the hydrogen/nitrogen mixture was higher than the air flow rate in the test cell. Therefore, the partial pressure of the hydrogen in the head space of the test cell is conservatively assumed to be 0.02 atm [0.29 psi], and the corresponding C_H is estimated to be 15.5 μmole/L using Eq. 4-1 This dissolved hydrogen concentration is also within the range reported by Wu et al. (2012, 2014).

The test matrix is summarized in Table 4-5 for the experiments. A total of 32 experiments were conducted. Of these, 12 were conducted in FY 2014, and the remaining 20 were conducted in FY 2015. Starting dates of the experiments are included in Table 4-5 to aid in the verification of experimental data used in this report. When the starting date of an experiment was 2014, it was conducted in FY 2014; otherwise, the experiment was conducted in FY 2015. The experimental data and their analyses are presented in Section 5.

Various tests (Condition 1–4 tests) undertaken in FY 2015 were conducted using the corrosion cell depicted in Figure 4-9(b). In this cell, the electrode surface was vertical with respect to the ground. This ensured that the gas bubbles did not accumulate on the electrode surface during the test. Furthermore, the Condition 4 tests, undertaken in 2015, were conducted using a piece of carbon steel inside the corrosion cell. The carbon steel piece was used to remove traces of dissolved oxygen from the test solution. An image of the corrosion under Condition 4 with the carbon steel piece is shown in Figure 4-12. The reddish brown deposits that developed on the heads of the gas diffusers and on the internal surface of the glass vessel indicate that the carbon steel reacted with the residual oxygen to form a ferric hydroxide corrosion product.

4.3.2 Experimental Challenges in Electrochemical Tests

Collecting noise-free EIS data was critical for estimating the dissolution rates accurately. Only noise-free data can be analyzed adequately to obtain dissolution rates. The experiments generate noise-free data when the experimental system is free from external interference or the overall impedance of the system is smaller than the input impedance of the potentiostat. It was found

Table 4-5. Test Matrix and Start Date of the SIMFUEL Dissolution Experiments				
SIMFUEL	Gases in the Test Solution			
	1.02 atmg [15 psig] compressed air	1.02 atmg [15 psig] compressed air and a 8.84 atmg [130 psig] of 4 percent H_2 plus 96 percent N_2	0.14 atmg [2 psig] compressed air and a 1.02 atmg [15 psig] 4 percent H_2 plus 96 percent N_2/0.7 atmg [10 psig] Compressed Air and a 1.02 atmg [15 psig] 4 percent H2 plus 96 percent N2	8.84 atmg [130 psig] 4 percent H_2 plus 96 percent N_2
UO_2	August 8, 2014	August 12, 2014 February 17, 2015 February 27, 2015	August 18, 2014* March 20, 2015† March 24, 2015†	August 5, 2014 April 14, 2015 April 17, 2015 June 26, 2015 August 7, 2015
35 GW-day/MTU burnup	July 7, 2014 August 17, 2015	June 24, 2014	July 1, 2014* March 31, 2015†	June 27, 2014 July 06, 2015
60 GW-day/MTU burnup	July 18, 2014	July 28, 2014 August 20, 2015	July 15, 2014* April 03, 2015†	July 21, 2014 April 07, 2015 April 21, 2015 June 02, 2015 June 08, 2015 June 15, 2015 July 17, 2015

*Conducted under 0.14 atmg [2 psig] compressed air and a 1.02 atmg [15 psig] 4 percent H_2 plus 96 percent N_2
†Conducted under 0.7 atmg [10 psig] compressed air and a 1.02 atmg [15 psig] 4 percent H_2 plus 96 percent N_2

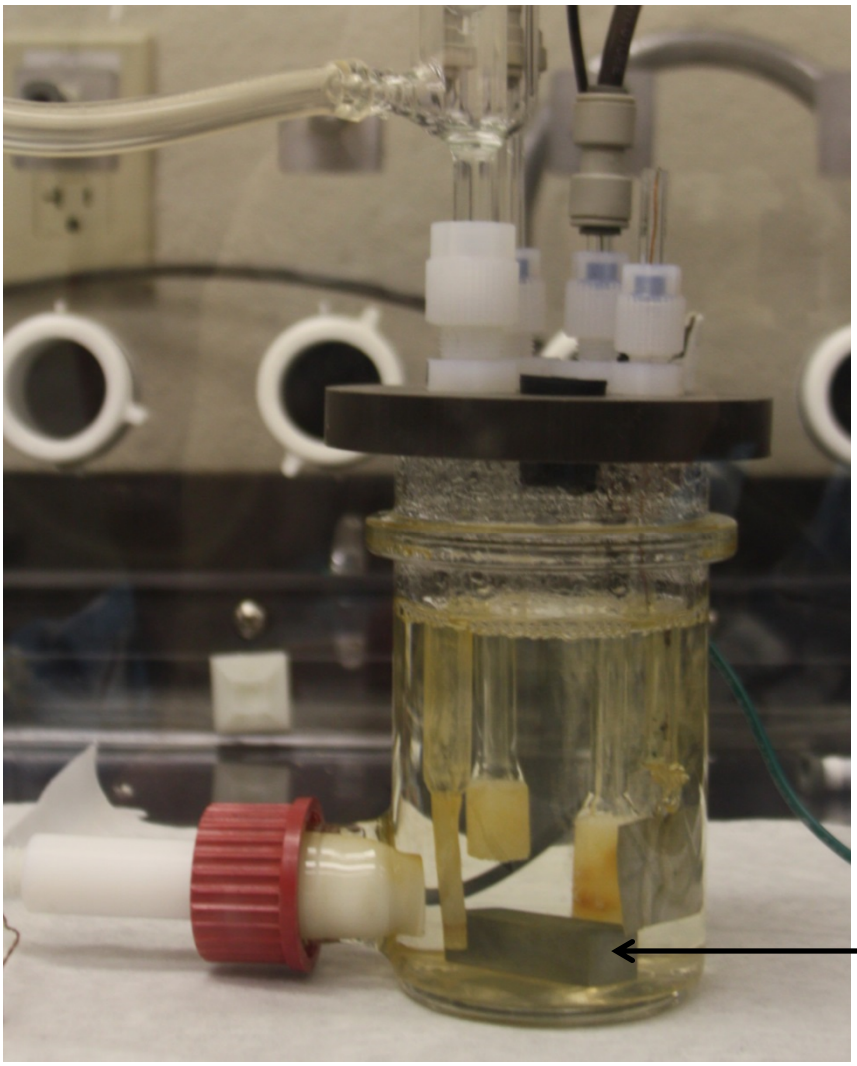

Figure 4-12. Condition 4 Test With Carbon Steel Piece Inside the Corrosion Cell

that several problems, such as the limitation of the current measuring resistor, corrupted the experimental data. The problems encountered, and their resolution follow:

- The base version of the VME3 potentiostat has current measuring resistors capable of measuring up to 10 μA. Because the applied potential was 20 mV for collecting the EIS data, the maximum impedance value that can be reliably measured is 2×10^5 Ω. This value is obtained assuming that a 10 μA current measuring resistor can accurately measure the current as low as 0.1 μA. In this study, impedance values of 10^7 Ω or higher were seen during the experiments. Resolution required procuring a low-current measuring device capable of current measurements as low as 1 nA. The low-current measuring device was attached to the VME3 potentiostat/frequency-response analyzer. This increased the capability of the instrument to reliably measure impedances of 10^9 Ω and higher.

- It was found that magnetic stirring of the solution was interfering with the impedance measurements. The magnetic stirring produced an electrical field, which interfered with

the electrical field between the working and counter electrode in the corrosion cell. The magnetic stirring of the solution was stopped, and several calibration experiments were conducted. Jung et al. (2011) had conducted experiments with the rotation of the working electrode. Jung et al. (2011) had measured the impedance of the working electrode while it was rotated at 1,000 rpm. A calibration experiment was conducted under similar conditions with 35 GW-day/MTU burnup equivalent SIMFUEL specimens. It was found that the impedance spectra obtained by the calibration experiment were similar to those Jung et al. (2011) reported. Considering this, it was found that stirring the test solution was not necessary and was thus eliminated.

- The experiments involved bubbling of the gases through the test solution. Initially, the working electrode assembly was approximately 4 cm [1.6 in] long. Gas bubbles often accumulated at the electrode surface as seen in Figure 4-13. To mitigate this problem, the SIMFUEL electrode assembly length was increased to 10.8 cm [4.25 in]. This ensured that gas discharge locations were above the electrode surface in the corrosion cell. This reduced chances of accumulation of the gas bubbles at the electrode surface. However, bubbles sometimes accumulated even with the 10.8-cm [4.25-in]-long electrode assembly. This is attributed to the internal convection of the test solution by the gas bubble. As discussed previously, another test cell was designed as depicted in Figure 4-9(b). As seen in Figure 4-9(b), the electrode assembly was inserted from side, and the electrode surface was vertical with respect to the ground. The use of the corrosion cell in Figure 4-9 (b) eliminated the possibility of the accumulation of gas bubbles at the electrode surface.

4.4 SIMFUEL Leaching Tests

In addition to the electrochemical tests, leaching experiments were conducted to determine dissolution rates using the leachate concentrations. The objective of these experiments was to measure the dissolution rate under the higher hydrogen fugacity {compared to 2.0×10^{-2} to 4.0×10^{-2} atm [0.29–0.59 psi] in the electrochemical tests} and a higher dissolved hydrogen concentration that was nearer to 1 mM. This concentration of dissolved hydrogen can be achieved when the fugacity of the hydrogen is close to 1.3 atm [19.1 psi].

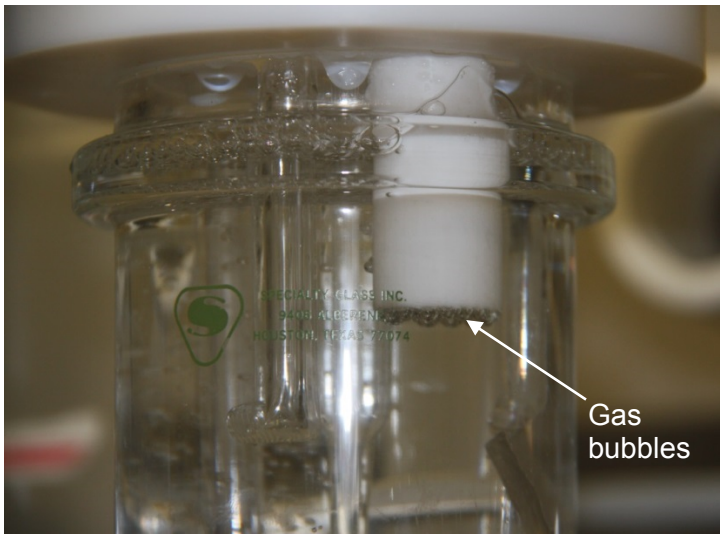

Figure 4-13. Accumulation of the Gas Bubbles at the SIMFUEL Electrode Surface

These experiments were conducted using two pipe reactors. An image of one of the pipe reactors is presented in Figure 4-14. The reactor consists of (i) a reactor body made of stainless steel tubing, and an end cap, (ii) a gas inlet valve, (iii) a pressure gauge, and (iv) a pressure release valve. These components were assembled using various fittings. The reactors were pressure checked and the pressure gauges were calibrated before use. The pressure readings in the gauges were accurate within ±1.02 atmg [±15 psig].

The reactors were fitted with Teflon® tube internal liners to hold the solution and fuel pellets inside the reactors. The following procedure was used to load the reactors with the SIMFUEL pellets and the granitic water solution to run the leaching experiments. First, approximately 200 mL [0.053 gal] of the granitic groundwater solution was purged of dissolved oxygen by injecting 4 percent hydrogen and 96 percent nitrogen mixture for 4 hours in a glovebox. The reactors were placed in the glovebox. Approximately 25 mL [6.6×10^{-3} gal] of the solution was then transferred to each reactor inside the glovebox. Following this step, a 35 GW-day/MTU pellet was placed in one of the two reactors and a 60 GW-day/MTU pellet was placed in the other reactor. The reactors were sealed inside the glovebox. The reactors were then taken out of the glovebox and immediately pressurized to approximately 30.6 atmg [450 psig] with the 4 percent hydrogen and 96 percent nitrogen mixture. The reactors were then placed in a fume hood. The pressures in the reactors were continuously monitored. Images of the reactors during the tests are presented in Figure 4-15. The two reactors are referred to as 35 GW-day/MTU (BU35) Pipe Reactor and 60 GW-day/MTU (BU60) Pipe Reactor hereafter for the sake of identification.

Two sets of leaching tests were conducted: 31-day and 84-day tests. It was observed that the reactors slowly lost pressure during the tests. Therefore, the reactors were periodically repressurized to 37.4 atmg [550 psig]. The reactor pressure data along with the pressurization events are presented in Figures 4-16(a) and 4-16(b) for the 31-day and 84-day leaching tests, respectively. As seen in Figures 4-16(a) and 4-16(b), both BU35 and BU60 pipe reactors lost pressures after initial pressurization. Both reactors were repressurised following the initial loss of pressure. Thereafter, the reactors were repressurized whenever loss of pressure was noticed. It was ensured that there is no ingress of ambient air during the repressurization events. The time average pressure values in the 31- and 84-day tests were above 30.6 atmg

[450 psig]. This value was used to estimate the dissolve hydrogen concentration in the test solution..

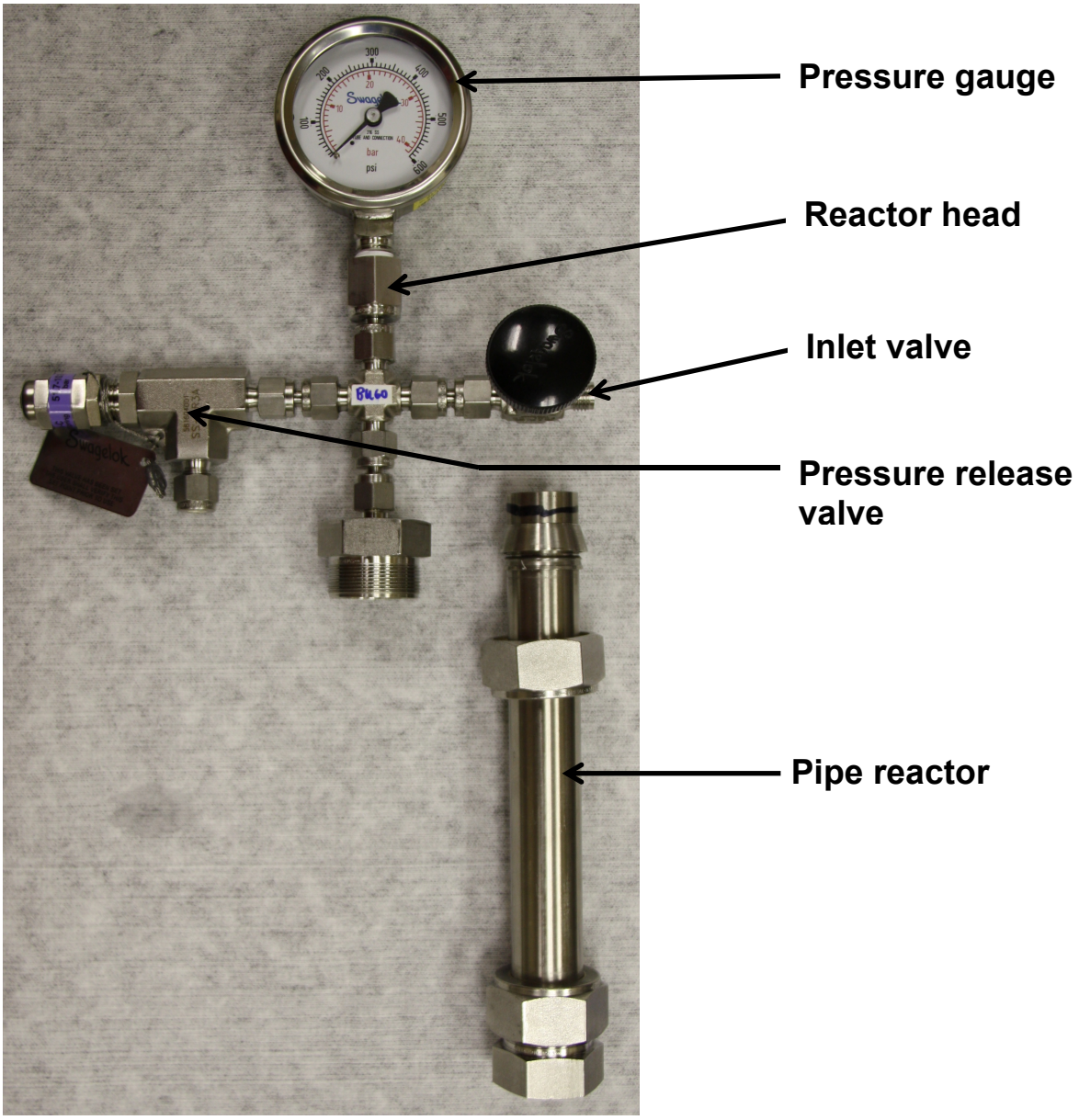

Figure 4-14. Pipe Reactor Used to Conduct the Leaching Tests

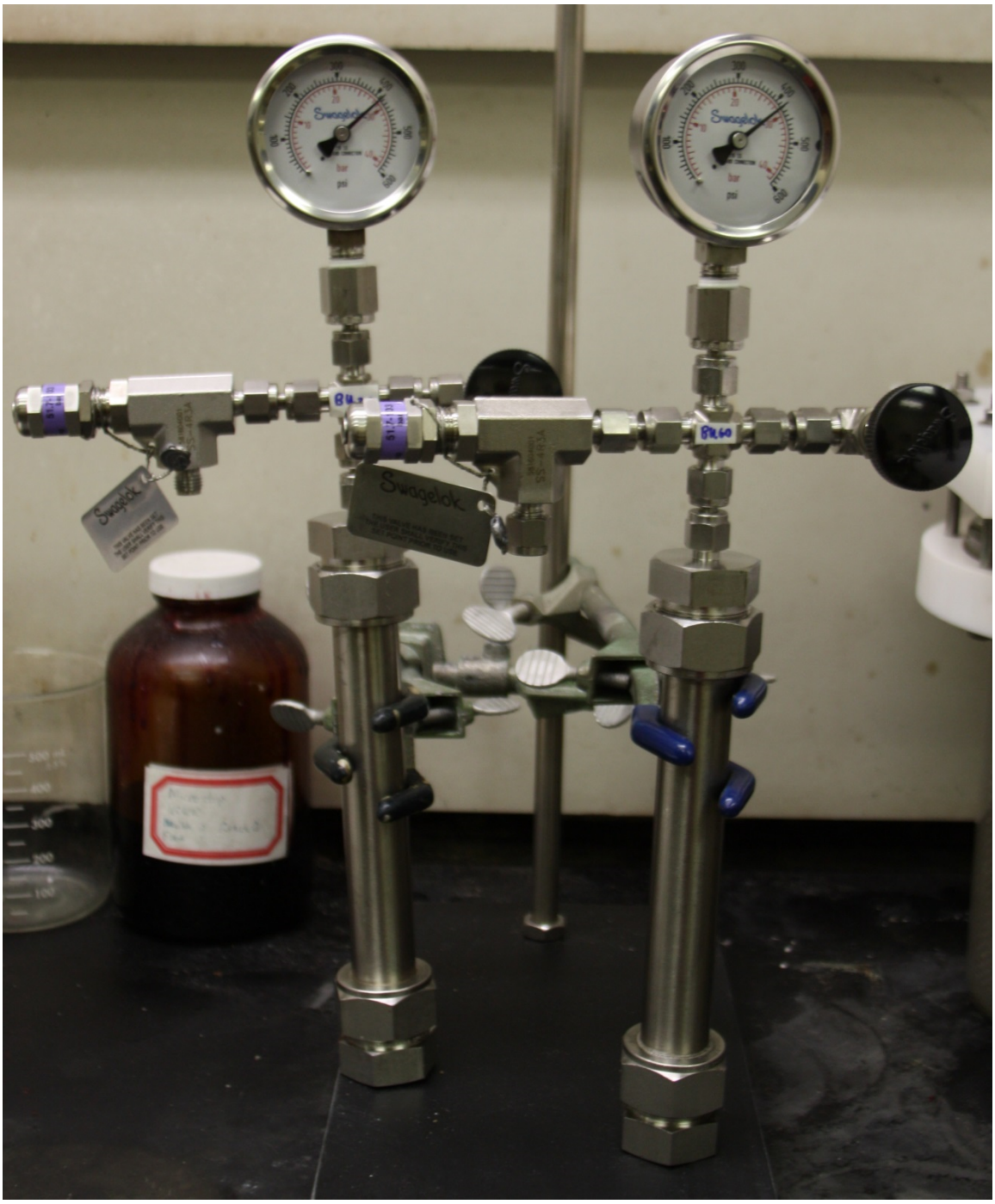

Figure 4-15. Pressurized Pipe Reactors During the Leaching Test

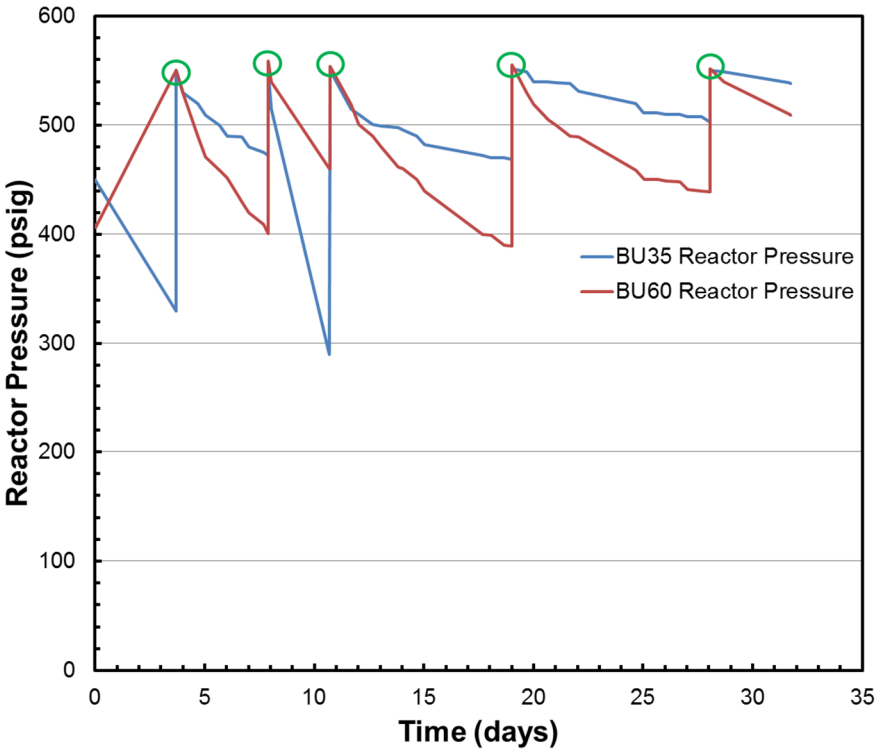

(a) **31-Day Test**

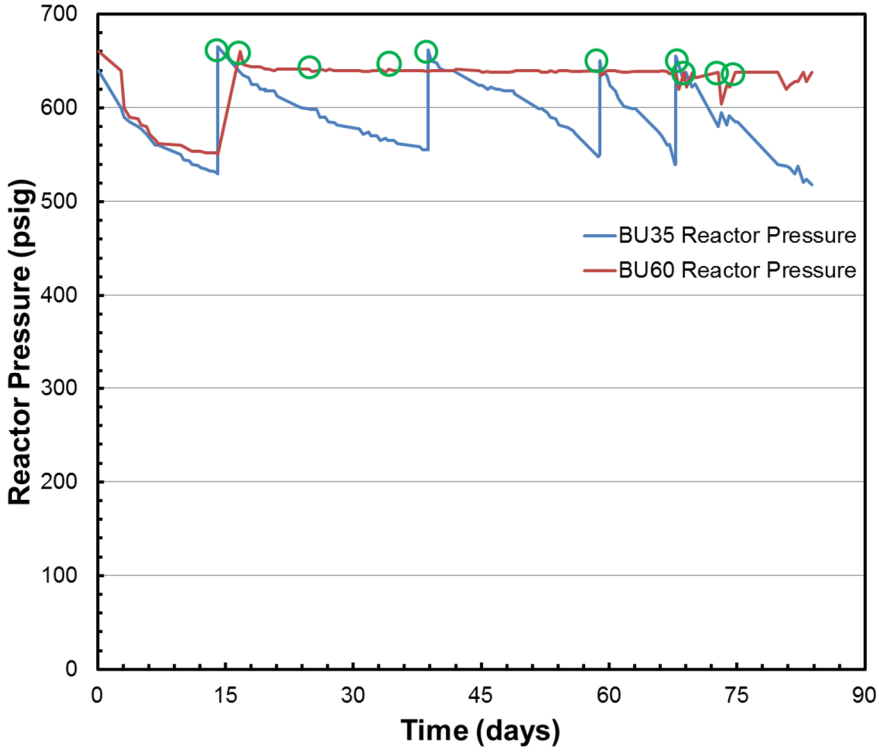

(b) 84-Day Test

Figure 4-16. 35 GW-day/MTU (BU35) and 60 GW-day/MTU (BU60) Reactor Pressure Versus Time for (a) 31- and (b) 84-Day Tests . The Green Circles Mark the Repressurization Events.

5 EXPERIMENTAL DATA AND RESULTS

The electrochemical and leaching test data and dissolution rate estimates are presented and described in this section.

5.1 Electrochemical Data

The electrochemical data included the collection of (1) electrode potential versus time, (2) electrochemical impedance spectroscopy, and (3) potentiodynamic polarization curve data.

5.1.1 Electrode Potential

Figures 5-1 and 5-2 show the electrode potential of the UO_2, 35 GW-day/MTU, and 60 GW-day/MTU burnup equivalent SIMFUEL electrodes as a function of time in the simulated granitic groundwater under four conditions at 22 °C [72 °F]. These conditions were (1) 1.02 atmg [15 psig] air; (2) 1.02 atmg [15 psig] air and 8.84 atmg [130 psig] 4 percent H_2 plus 96 percent N_2; (3) 0.14 atmg [2 psig] air and 1.02 atmg [15 psig] 4 percent H_2 plus 96 percent N_2; or 0.70 atmg [10 psig] air and 1.02 atmg [15 psig] 4 percent H_2 plus 96 percent N_2; and (4) 8.84 atmg [130 psig] 4 percent H_2 plus 96 percent N_2. The data in Figure 5-1 are for experiments conducted in fiscal year (FY) 2014. The data in Figure 5-2 are for the experiments conducted during 2015. In all cases, the electrodes were polarized to −1.0 V_{SCE} for 10 minutes before letting them rest at the open circuit potential for 16 hours. The electrode potentials were measured during and immediately following the impedance measurements. As seen in Figures 5-1 and 5-2, the electrode potentials reached steady state in about 15–20 hours after initial polarization. The steady-state values of the electrode potential are the corrosion potentials of the electrodes.

Dissolved oxygen concentrations of the test solutions were measured immediately after the electrochemical tests (Tables 5-1 and 5-2). These measurements were conducted while the corrosion cell was inside the glove box. The measured oxygen concentrations are highest for Condition 1 when air at 1.02 atmg [15 psig] was bubbled through the solution. This result was anticipated because the solution is expected to be saturated with oxygen under Condition 1. The measured oxygen concentrations were below the lower detection limit (<0.005 ppm) of the oxygen meter for Condition 4 when the H_2 and N_2 mixture was bubbled through the test solution. This was anticipated, because the nitrogen in the gas mixture is expected to deplete the oxygen in the solution. In Tables 5-1 and 5-2, the oxygen concentrations under Conditions 2 and 3 are between those for Conditions 1 and 4, which is consistent with both oxygen and hydrogen being bubbled through the solutions.

It was intended that the dissolved oxygen concentrations for Conditions 2 and 3 would be varied by changing the air flow rate into the solution. The oxygen concentrations under Condition 2 were expected to be greater than the concentrations under Condition 3, because the air flowrate in the solution for Condition 2 was higher than for Condition 3. As expected, the measured oxygen concentration for the UO_2 electrode under Condition 2 was higher than the concentration under Condition 3. For the FY 2014 experimental data in Table 5-1, the oxygen concentration for the UO_2 electrode under Condition 3 is less than 0.005 mg/L. For this condition, the air was bubbled at a rate of 5 L/min and the hydrogen plus nitrogen mixture was bubbled at a rate of 130 L/min. It is not clear why the measured oxygen concentration was undetectable under Condition 3 for the UO_2 electrode, but it may reflect the low flow rate of air, and a fluctuation in the air flow rate. For the FY 2015 experimental data in Table 5-2, the

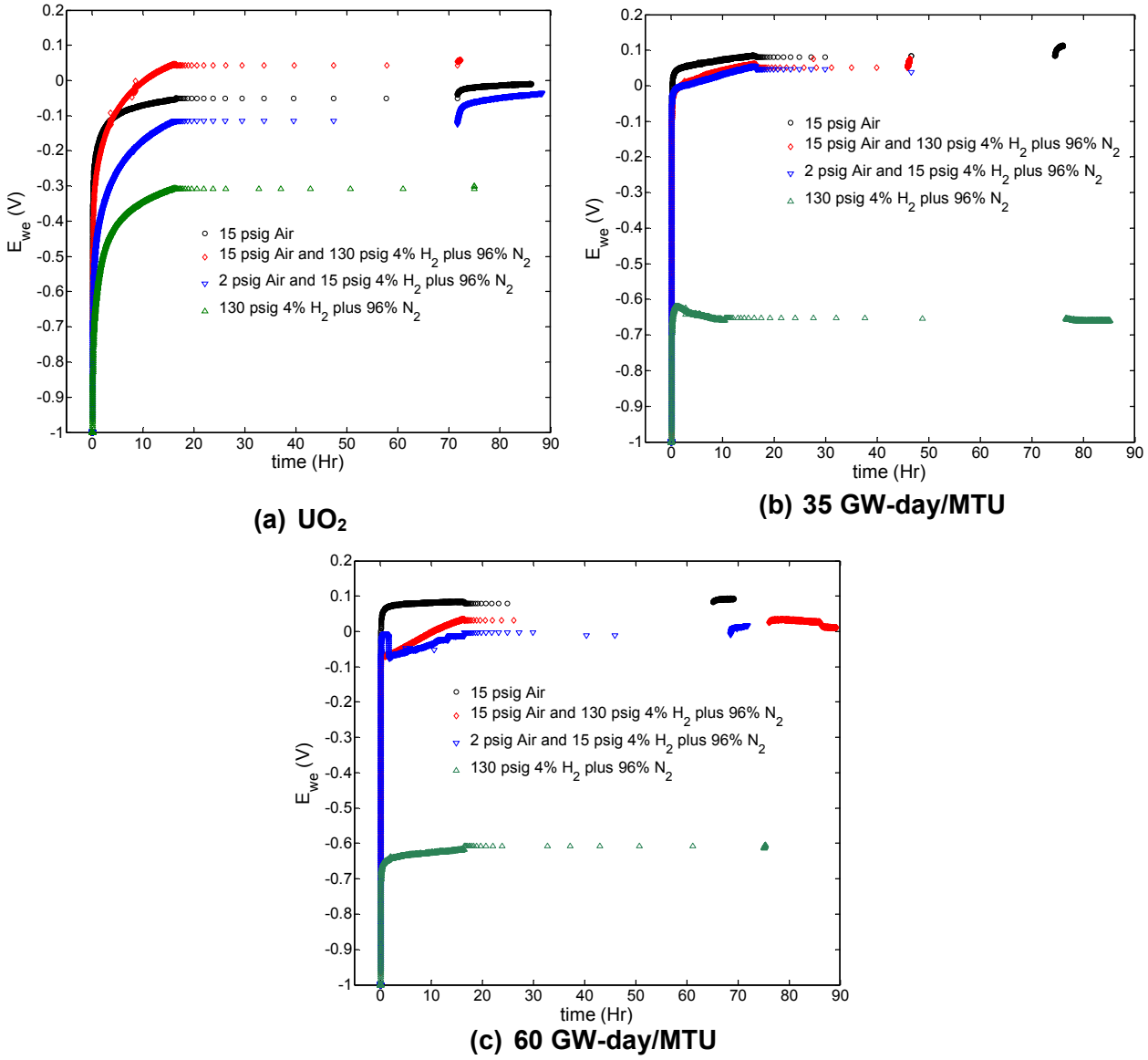

Figure 5-1. Working Electrode Potential (E_{we}) With Respect to Saturated Calomel Electrode Versus Time for (a) UO_2, (b) 35 GW-day/MTU, and (c) 60 GW-day/MTU Burnup Equivalent SIMFUEL Specimens Under the Four Conditions for the Experiments Conducted in FY 2014

oxygen concentration for the UO_2 electrode for Condition 3 was approximately 0.70 mg/L (which is in line with the expectation of low oxygen concentration). The air was bubbled at the rate of 40–50 L/min, and the hydrogen plus nitrogen mixture was bubbled at a rate of 100–130 L/min for the Condition 3 experiment in FY 2015. The oxygen concentration for the Condition 2 experiment in FY 2015 was approximately 2.08 mg/L, which is higher than for the FY 2014 experiment.

The oxygen concentrations for the 35 GW-day/MTU electrode under Conditions 2 and 3 are relatively close to each other for the FY 2014 experiments, whereas the oxygen concentration

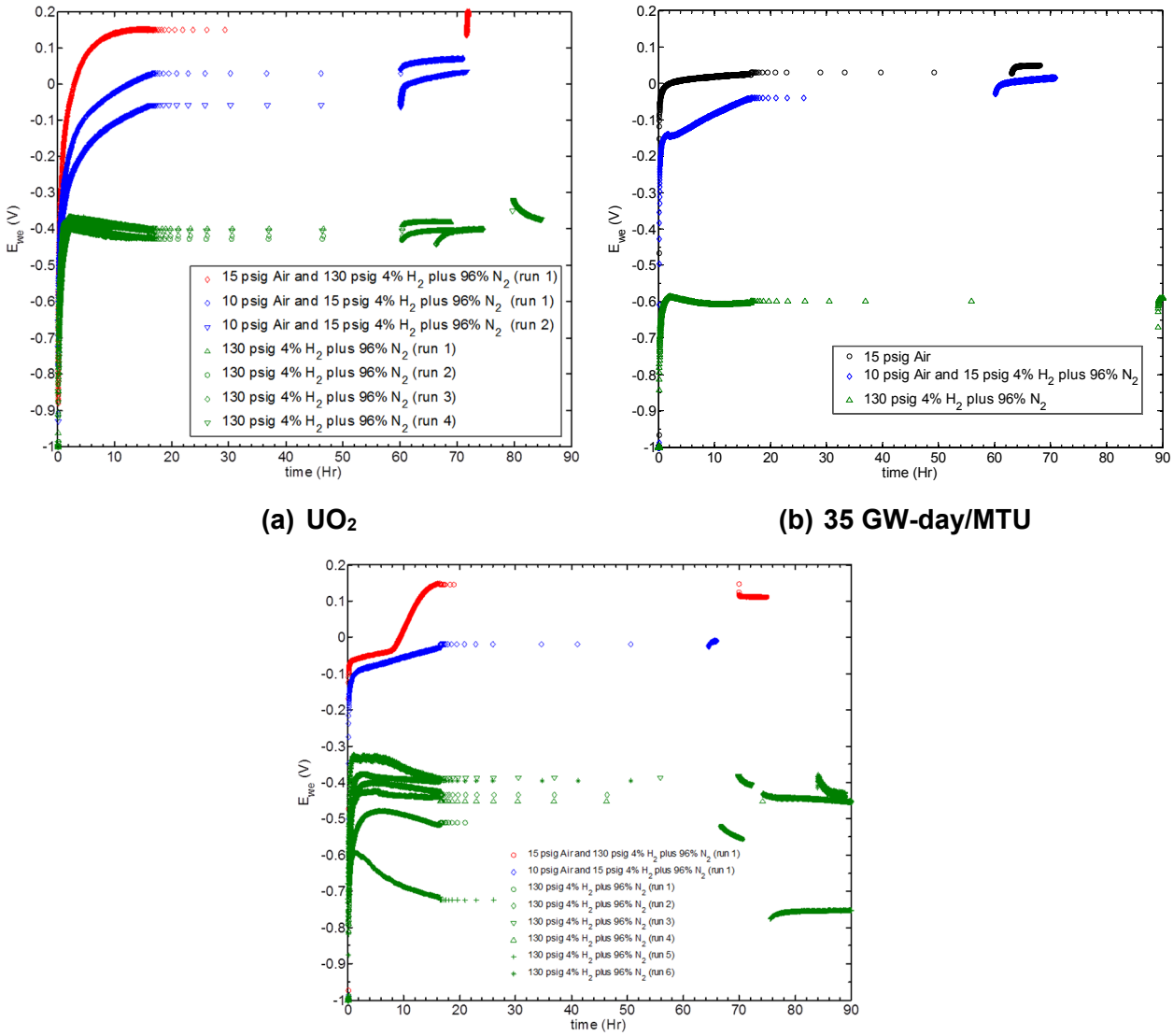

(a) UO_2 **(b) 35 GW-day/MTU**

(c) 60 GW-day/MTU

Figure 5-2. Working Electrode Potential (E_{we}) With Respect to Saturated Calomel Electrode Versus Time for (a) UO_2, (b) 35 GW-day/MTU, and (c) 60 GW-day/MTU Burnup Equivalent SIMFUEL Specimens Under the Four Conditions for the Experiments Conducted in FY 2015

under Conditions 2 was expected to be greater than under Conditions 3. For this reason, the Condition 3 experiment was repeated in FY 2015, with a measured oxygen concentration of 0.76 mg/L. In addition, the Condition 1 experiment was repeated for the 35 GW-day/MTU electrode, because the oxygen concentration in the FY 2014 experiment under Condition 1 was 5.35 mg/L, which was less than the expected value of approximately 7.5 mg/L. The oxygen concentration in the FY 2015 experiment under Condition 1 was 7.93 mg/L, falling within the expected range.

Table 5−1. Oxygen Concentration in the Test Solutions Immediately After Completion of the Electrochemical Experiments in FY 2014			
Test Condition	**Oxygen Concentration (mg/L)**		
	UO_2	**35 GW-day/MTU burnup**	**60 GW-day/MTU burnup**
1. 1.02 atmg [15 psig] air	7.67	5.35	7.58
2. 1.02 atmg [15 psig] air and 8.84 atmg [130 psig] of 4 percent H_2 plus 96 percent N_2	0.95	3.04	0.83
3. 0.14 atmg [2 psig] air and 1.02 atmg [15 psig] of 4 percent H_2 plus 96 percent N_2	<0.005*	3.19	3.71
4. 8.84 atmg [130 psig] of 4 percent H_2 plus 96 percent N_2	<0.005*	<0.005*	<0.005*
*Lower detection limit of the instrument			

Table 5−2. Oxygen Concentration in the Test Solutions Immediately After Completion of the Electrochemical Experiments in FY 2015			
Test Condition	**Oxygen Concentration (mg/L)**		
	UO_2	**35 GW-day/MTU burnup**	**60 GW-day/MTU burnup**
1. 1.02 atmg [15 psig] air	—	7.93	—
2. 1.02 atmg [15 psig] air and 8.84 atmg [130 psig] of 4 percent H_2 plus 96 percent N_2	2.08	—	1.82
3. 0.70 atmg [10 psig] air and 1.02 atmg [15 psig] of 4 percent H_2 plus 96 percent N_2	0.70 (run1) 0.71 (run2)	0.76	0.73
4. 8.84 atmg [130 psig] of 4 percent H_2 plus 96 percent N_2	<0.005* (for all runs)	<0.005* (for all runs)	<0.005* (for all runs)
*Lower detection limit of the instrument			

In the FY 2014 experiments, the oxygen concentrations for the 60 GW-day/MTU electrodes under Condition 2 were lower than the concentrations under Condition 3. This was unexpected, and additional experiments were conducted under Conditions 2 and 3 for the 60 GW-day/MTU electrode in FY 2015. The oxygen concentration for the FY 2015 experiments under Conditions 2 and 3 were consistent with expected values of 1.82 and 0.73 mg/L for

Conditions 2 and 3, respectively. The corrosion potentials of the three electrodes under reducing conditions (i.e., Condition 4) are the lowest among the four conditions. The corrosion potentials of the 35 and 60 GW-day/MTU SIMFUEL electrodes were lower than –0.4 V_{SCE} under reducing conditions (Condition 4) for both FY 2014 and 2015 experiments. Corrosion potentials for the 35 and 60 GW-day/MTU SIMFUEL electrodes sometimes fell below –0.6 V_{SCE} under reducing conditions (Condition 4). This observation is consistent with the reported literature (Shoesmith, 2007, 2008), indicating that the corrosion potential of the spent nuclear fuel (SNF) under the reducing conditions is expected to be below –0.4 V_{SCE}. Shoesmith (2007, 2008) also stated that corrosion potentials below –0.4 V_{SCE} are indicative of the hydrogen effect under reducing conditions. Shoesmith (2008) argued that corrosion potential values greater than –0.4 V_{SCE} are indicative of surface dissolution and, SNF oxidation.

The corrosion potential of the UO_2 electrode exceeded –0.4 V_{SCE} even under reducing conditions and was approximately –0.3 V_{SCE} for the FY 2014 experiments. The corrosion potential of the UO_2 electrode was close to –0.4 V_{SCE} for the FY 2015 experiments. A potential value exceeding or being close to –0.4 V_{SCE} can be attributed to the absence of ε particles in the UO_2 electrode matrix (Shoesmith, 2008). Shoesmith (2008) also showed that the corrosion potential falls below –0.4 V_{SCE} when the burnup level is 6 percent SIMFUEL (in which the simulated burnup is expressed as an atomic percent). The 6 percent burnup is equivalent to 60 GW-day/MTU (Jung et al., 2011). Shoesmith (2008) reported the corrosion potential data at 60 °C [140 °F]. Shoesmith (2008) further reported that the corrosion potential of the UO_2 SIMFUEL with no ε particles was approximately –0.17 V_{SCE}. Corrosion potentials generally increase with increasing temperature because the rate of the anodic and cathodic reactions accelerates with temperature. The Shoesmith (2008) corrosion potential data were collected at 60 °C [140 °F] whereas this study's data were collected at 22 ± 2 °C [72 ± 4 °F]. Since corrosion potentials are expected to increase with temperature, the corrosion potential values ranging between –0.3 to –0.4 V_{SCE} at 22 ± 2 °C [72 ± 4 °F] are consistent with –0.17 V_{SCE} at 60 °C [140 °F]. Considering the temperature difference and the absence of the ε particles in the UO_2 electrodes, the corrosion potential values of the UO_2 electrode under reducing conditions are consistent with the literature data.

The corrosion potential data of the three SIMFUEL electrodes under reducing conditions can also be used to assess the rate of the anodic and cathodic reactions at the SIMFUEL electrode surface. When the anodic and cathodic reactions balance each other, the corrosion potential is the electrode potential (in accordance with the principle of mixed potentials). The lower corrosion potential of SIMFUEL electrodes under the reducing conditions could be due to either the higher anodic dissolution rate or the relatively lower cathodic reduction rate on the electrode surface. Considering the relatively smaller grain size and the higher heterogeneity of the 35 and 60 GW-day/MTU SIMFUEL electrodes (compared to the UO_2 electrode), it is likely that a relatively higher grain boundary area with more precipitates on the surface can lead to a more rapid and higher anodic dissolution rate of 35 and 60 GW-day/MTU SIMFUEL electrodes. This is supported by the observation of preferential dissolution in the grain boundaries on the SIMFUEL surface by Shoesmith and Sunder (1998) and Santos et al. (2006a,b). Rare-earth dopants (such as yttrium, lanthanum, cerium, and neodymium), and noble metal inclusions (such as molybdenum,ruthenium, rhodium, and palladium), in SIMFUEL tend to catalyze the reduction reaction in SIMFUEL under reducing conditions (Shoesmith et al., 1996; Santos et al., 2006a,b; Martin et al., 2008). Because rare-earth dopants and noble metal inclusions are not present in the UO_2 SIMFUEL electrode, the cathodic reduction reactions cannot be catalyzed at the electrode. The lower value of the corrosion potential under reducing conditions for the 35 and 60 GW-day/MTU SIMFUEL electrodes compared to the UO_2 electrode suggest that the rate of the cathodic reduction reaction is more affected by the presence of the rare-

earth and the noble metal inclusions compared to the anodic dissolution reaction. Specifically, the rate of cathodic reaction is lowered under the reducing conditions at the 35 and 60 GW-day/MTU SIMFUEL electrodes compared to the UO2 electrode, leading to lower values of corrosion potentials of the two electrodes compared to the UO_2 electrode.

The corrosion potential data under oxygen saturated conditions (i.e., Condition 1), and under the intermediate oxygen concentrations (i.e., Conditions 2 and 3) for the three SIMFUEL electrodes, are shown in Figures 5-1 and 5-2. For these three conditions, Figures 5-1(a) and 5-2(a) show corrosion potentials that are in the range of –0.1 to 0.2 V_{SCE} for the UO_2 electrode. The corrosion potential of the UO_2 electrode under Condition 3 is lower than Conditions 1 and 2. This is indicative of the lower oxygen concentration under Condition 3 than under Conditions 1 and 2, further correlating the oxygen concertation with the corrosion potential data for the UO_2 electrode. The corrosion potential of the UO_2 electrode under Condition 3 is higher than Condition 4. This indicates that the oxygen concentration under Condition 3 was higher than under Condition 4 (even though the oxygen concentration could not be detected using the meter in the FY 2014 experiment). The corrosion potentials of the 35 and 60 GW-day/MTU SIMFUEL electrodes were in the range of –0.1 to 0.2 V_{SCE} under the three conditions.

The corrosion potential data of the three electrodes under Conditions 1–3 are consistent with the literature. Shoesmith et al. (1996) and Shoesmith and Sunder (1998) measured corrosion potentials ranging from 0.0 to 1.2 V_{SCE} in aerated neutral or weakly alkaline solutions containing chloride and/or carbonate ions. Shoesmith et al. (1998) and Shoesmith and Sunder (1996) also reported that measured corrosion potentials were not different from those of unirradiated UO_2 or irradiated SNF. The corrosion potential values observed in this work are used to infer surface film composition as per information in Shoesmith et al. (1998) and Shoesmith and Sunders (1996). It is inferred that the UO_2 surface can be oxidized to produce a $UO_{2.333}$ film, and further precipitate a secondary phase (in the form of $UO_3 \cdot xH_2O$) and/or dissolve to $UO_2(CO_3)_2^{2-}$ depending on the solution chemistry.

The corrosion potential data in this study also are consistent with Carbol et al., (2005, Tables 2-12 and 2-13), who reported on the corrosion potential of the 10 and 1 percent U-233 doped UO_2 in a 10 mM NaCl solution. Carbol et al. (2005) found that the corrosion potential of the 10 percent U-233 doped UO_2 was in the range of −0.1 to 0.05 V_{SCE} when the test solution was purged with N_2. For the same conditions, Carbol et al. (2005) found that the corrosion potential of the 1 percent U-233 doped UO_2 was in the range of 0.1 to 0.15 V_{SCE}. Carbol et al. (2005) also reported on the corrosion potential data for a test solution that was purged with 8 percent H_2 plus 92 percent N_2. The corrosion potential for these tests were in the range of −0.25 to −0.55 V_{SCE} for the 10 percent U-233 doped UO_2 under the H_2 plus N_2 condition. Similarly, the corrosion potentials were in the range of −0.25 to −0.35 V_{SCE} for the 1 percent U-233 doped UO_2 under the H_2 plus N_2 condition. Carbol et al. (2005) initially bubbled the gases through the test solution and then pressurized the test cell with the N_2 gas or H_2 plus N_2 gas mixture. The process of bubbling N_2 is expected to remove most of the initial dissolved oxygen from the test solution. However, the alpha radiation from the 10 and 1 percent U-233 doped UO_2 is expected to produce oxygen due to radiolysis. Carbol et al. (2005) also noticed that the corrosion potential values slightly increased with time in the case of 10 and 1 percent U-233 doped UO_2 (using the H_2 plus N_2 mixture). The slight increase in the corrosion potential indicates the presence of oxygen in the test solution. Finally, the range of the corrosion potential values obtained in this investigation roughly matched those that Carbol et al. (2005) reported.

5.1.2 Electrochemical Impedance Spectroscopy

Figure 5-3 shows the Bode and phase angle impedance spectra for the UO_2 SIMFUEL electrode under four conditions in simulated granitic groundwater for experiments in FY 2014

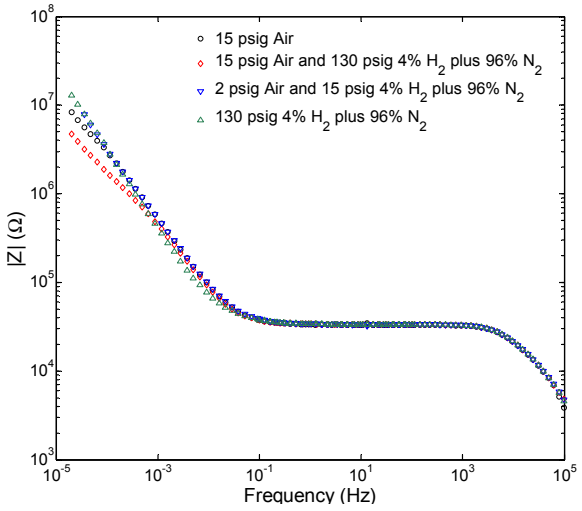

(a) Impedance Versus Frequency (FY 2014)

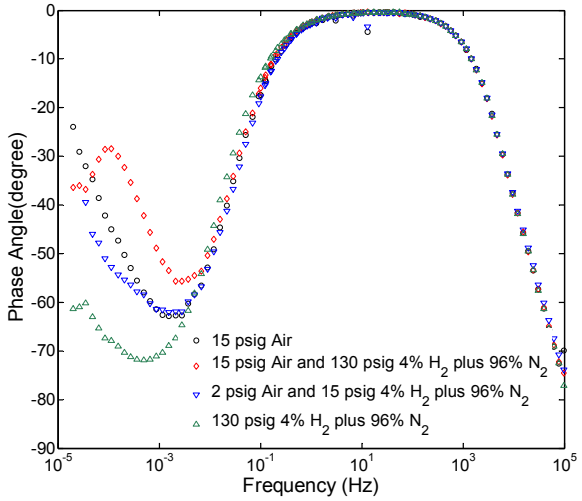

(b) Phase Versus Frequency (FY 2014)

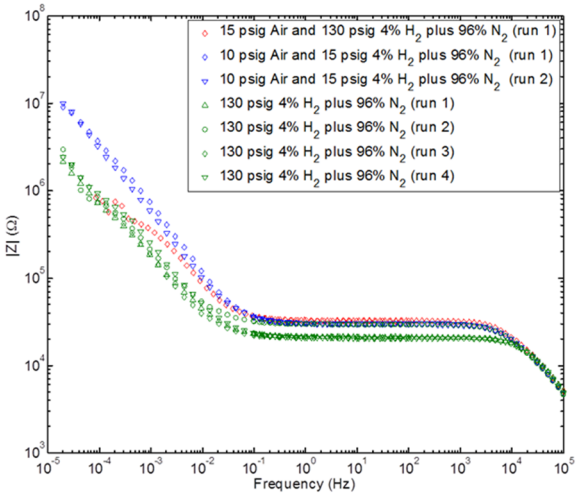

(c) Impedance Versus Frequency (FY 2015)

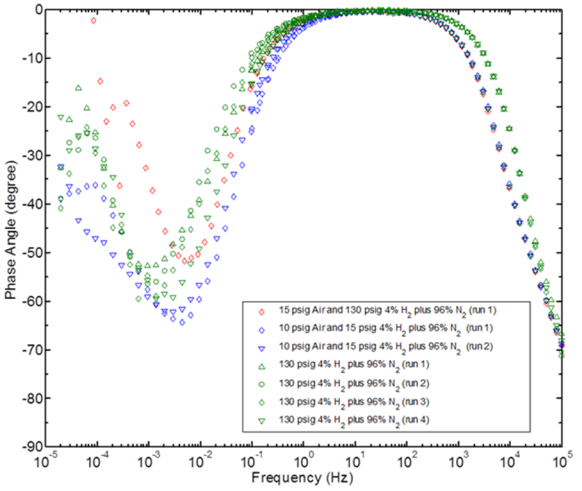

(d) Phase Versus Frequency (FY 2015)

Figure 5-3. Electrochemical Impedance Spectra of UO_2 SIMFUEL Specimen Measured After 16 Hours of Immersion at Corrosion Potential Tested in the Simulated Granitic Groundwater at 22 °C [72 °F] Under the Four Conditions in FY 2014 and 2015.

and 2015. The four conditions are (i) 1.02 atmg [15 psig] air, (ii) 1.02 atmg [15 psig] air and 8.84 atmg [130 psig] of 4 percent H_2 plus 96 percent N_2, (iii) 0.14 atmg [2 psig] air and 1.02 atmg [15 psig] of 4 percent H_2 plus 96 percent N_2 (for FY 2014) and 0.70 atmg [10 psig] air and 1.02 atmg [15 psig] of 4 percent H_2 plus 96 percent N_2 (for FY 2015), and (iv) 8.84 atmg [130 psig] of 4 percent H_2 plus 96 percent N_2. Similarly, Figures 5-4 and 5-5 show the

impedance spectra for the 35 and 60 GW-day/MTU burnup equivalent SIMFUEL electrodes, respectively, under the four conditions for experiments in FY 2014 and 2015. The impedance data for the three SIMFUEL electrodes under each condition are presented in Appendix A and Appendix B for the FY 2014 and 2015, respectively.

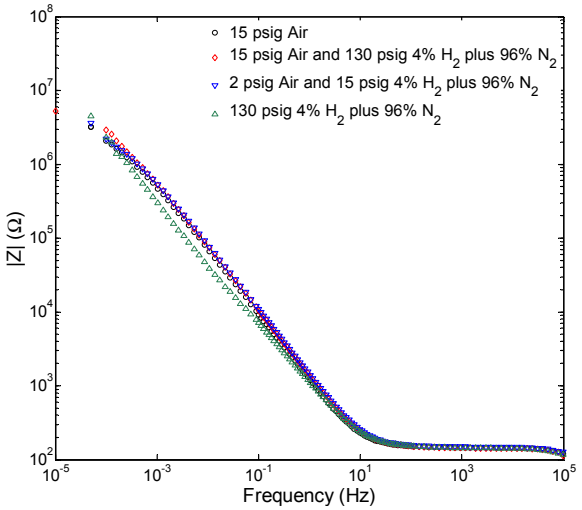

(a) Impedance Versus Frequency (FY 2014)

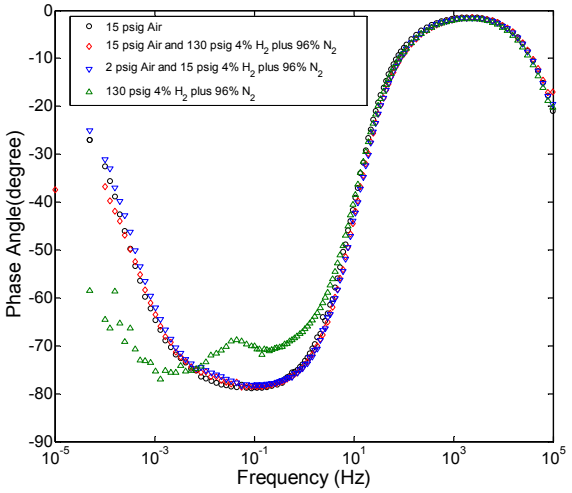

(b) Phase Versus Frequency (FY 2014)

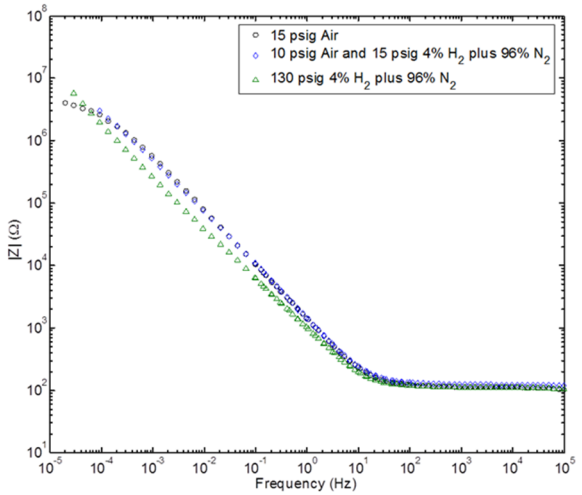

(c) Impedance Versus Frequency (FY 2015)

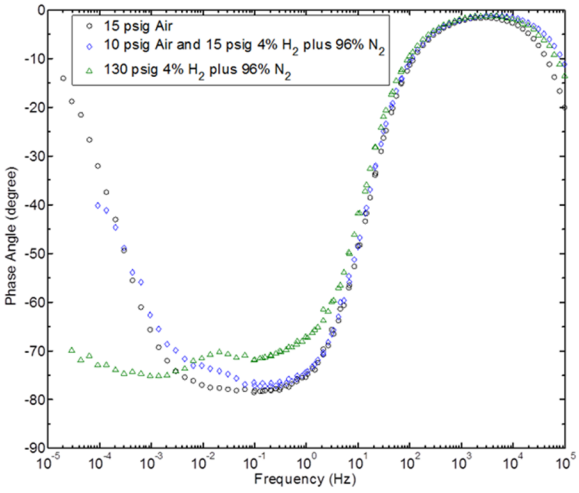

(d) Phase Versus Frequency (FY 2015)

Figure 5-4. Electrochemical Impedance Spectra of 35 GW-day/MTU Burnup Equivalent SIMFUEL Specimen Measured After 16 Hours of Immersion at Corrosion Potential Tested in the Simulated Granitic Groundwater at 22 °C [72 °F] Under the Four Conditions in FY 2014 and FY 2015.

A time constant in the electrochemical impedance data is broadly defined as inverse of the angular frequency, i.e., 2π×frequency, when the phase angle is minimal. Existence of one or multiple time constants in an impedance spectra is recognized when phase versus frequency plot exhibit one or more troughs. Exact values of time constants are not important in this discussion; instead the range of frequency where time constants appear to occur in an impedance spectrum is identified and discussed.

In Figures 5-3(b) and 5-3(d) for the UO_2 SIMFUEL electrode, the impedance data indicate two time constants. The first time constant is associated with the high frequency, and appears to occur in the frequency range of 10 Hz to higher frequencies. The second time constant is apparent in the frequency range of 10 Hz to lower frequencies, and appears near 0.01 Hz for Conditions 1-3, and at 0.001 Hz for Condition 4. The first time constant represents the ohmic resistance due mainly to the intrinsic electrical resistance of the SIMFUEL pellet and resistance of the electrolyte solution to the charge flow (Jung et al., 2011). The second time constant is associated with the polarization resistance at the SIMFUEL electrode surface (Jung et al., 2011). The polarization resistance values are needed to estimate the dissolution rates. The polarization resistance values can be determined when impedance associated with the second time constant reach a steady state, similar to when the impedance reaching steady state for the first time constant in Figures 5-3(a), 5-3(c), 5-4(a), 5-4(c), 5-5(a), and 5-5(c). But it required measuring impedances at very low frequencies (10^{-6} Hz or less). This was not possible considering the time needed to collect the data. For example, one impedance measurement at 10^{-6} Hz would have required approximately 24 days. Several such impedance measurements at the frequencies of 10^{-6} Hz and lower would have been needed to observe the steady state impedance associated with the second time constant. For this reason, the measured impedance data were extrapolated to estimate the polarization resistances associated with the second time constant.

In Figures 5-4(b) and 5-4(d) for the 35 GW-day/MTU burnup equivalent SIMFUEL electrode, the impedance data also indicate two time constants. The first time constant is estimated to occur in the frequency range of approximately 10^4 Hz to higher frequencies, and the second time constant is apparent in the frequency range of 10^4 Hz to lower frequencies. For Conditions 1–3, the frequency range associated with the second time constant is estimated to be 10^{-8} to 10^4 Hz, with the trough being observed near 0.1 Hz in Figures 5-4(b) and 5-4(d). The frequency range for the second time constant for Condition 4 is also approximately 10^{-8} to 10^4 Hz, with the trough being observed near 0.001 Hz in Figures 5-4(b) and 5-4(d). These results are indicative of very high steady state impedance associated with the second time constant. Similarly in Figures 5-5(b) and 5-5(d) for the 60 GW-day/MTU burnup equivalent SIMFUEL electrode, the impedance data indicate two time constants in the same frequency range as the 35 GW-day/MTU burnup equivalent SIMFUEL electrode. From the EIS data, it is clear that the key difference between the UO_2 and the other two SIMFUEL electrodes is the frequency range of the first time constant. The lower bound of the frequency range associated with the first time constant increases by a factor of 100 for the 35 and 60 GW-day/MTU burnup equivalent SIMFUEL electrodes compared to the UO_2 electrode. Another key difference is the frequency value associated with the second time constant under Condition 4 compared to Conditions 1-3. The Condition 4 second time constants occur near 0.001 Hz in Figures 5-3(b), 5-3(d), 5-4(b), 5-4(d), 5-5(b), and 5-5(d). In contrast, Conditions 1-3 second time constants occur near 0.1 Hz. This observation suggests that the steady state impedance for Condition 4 would occur at a lower frequency compared to Conditions 1-3.

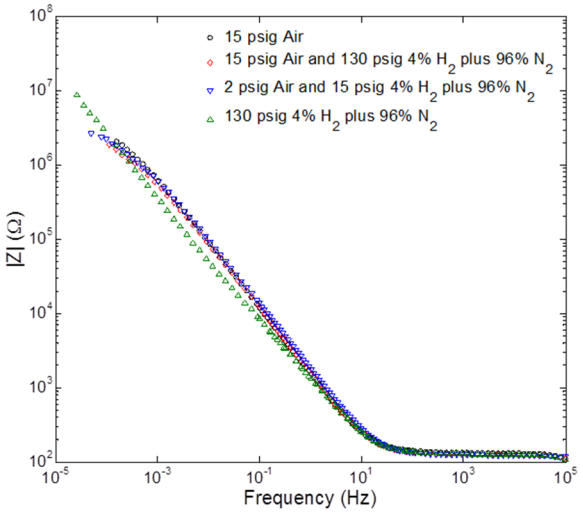

(a) Impedance Versus Frequency (FY 2014)

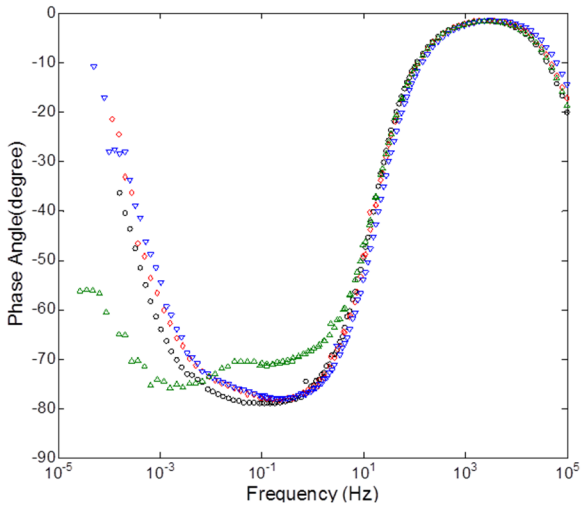

(b) Phase Versus Frequency (FY 2014)

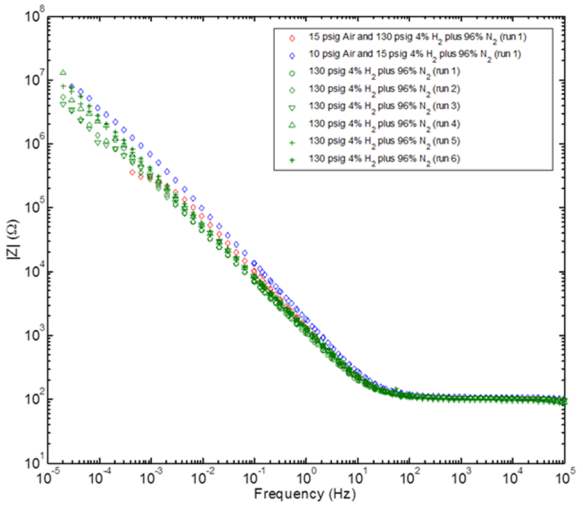

(c) Impedance Versus Frequency (FY 2015)

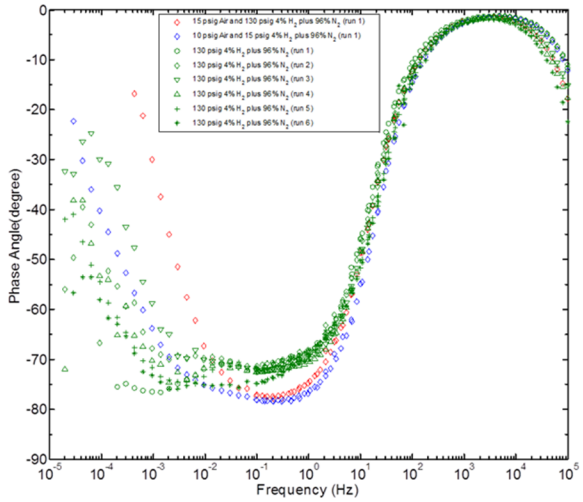

(d) Phase Versus Frequency (FY 2015)

Figure 5-5. Electrochemical Impedance Spectra of 60 GW-day/MTU Burnup Equivalent SIMFUEL Specimen Measured After 16 Hours of Immersion at Corrosion Potential Tested in the Simulated Granitic Groundwater at 22 °C [72 °F] Under the Four Conditions in FY 2014 and 2015.

In repeated measurements for each condition, there was variation in the corrosion potential and impedance for each electrode in a given condition. This variation may have resulted from the microstructural variation of the electrode surface. For each experiment, the electrode surface was polished and cleaned before being placed in the corrosion cell. This was done in order to expose a fresh electrode surface for each run. SIMFUEL pellets were prepared by mixing and ball milling the UO_2 (natural uranium) powder with additives of non-radiactive, chemically equivalent, and surrogate fission product oxides and pure elements. Because it is not a controlled commercial-grade process, the experimental specimens may be more heterogeneous than a commercial SNF matrix. As a result, the epsilon particle distribution should be expected to vary from surface to surface, with resulting variations in the experimental data.

An electrical circuit model was used to analyze the impedance data in Figures 5-3 to 5-5 using the mathematical approach detailed in Shukla (2004). The circuit model is shown in Figure 5-6. This circuit model is similar to the one Carbol et al. (2005) used, except for this work, one additional parameter was added. In this circuit model, the first time constant denoted by the parameters Rb and Cb is exactly same as the one in Carbol et al. (2005). The two parameters (Rb and Cb) represent the intrinsic ohmic resistance (Rb) and capacitance (Cb) of the SIMFUEL electrode particles, grain boundaries, oxide layer, and electrolyte solution resistance. The second time constant is denoted by parameters Rp, Cdl, and α in Figure 5-6. The second time constant associated with the polarization resistance (Rp) was modified to be a constant phase element (MacDonald, 1990). In the second time constant, Rp and Cdl represent the polarization resistance and capacitance at the electrode surface, and α was used to model the nonideal behavior of the electrode surface. Carbol et al. (2005) did not include α in the second time constant. The parameter N in Figure 5-6 denotes an additional noise-level resistor in the circuit and is not related to any physical property. This approach provided a better fit of the circuit model to the experimental data compared to the two time constants in the Randles circuit considered by Carbol et al. (2005). Figure 5-7 shows a representative circuit model fit to the impedance data for the UO_2 electrode under 8.84 atmg [130 psig] of 4 percent H_2 plus 96 percent N_2. The estimated polarization resistance values for the three electrodes are listed in Tables 5-3 and 5-4 for the FY 2014 and FY 2015 impedance data, respectively. The circuit model fit for the rest of the impedance data is provided in Appendices A and B for the FY 2014 and 2015 data, respectively.

The polarization resistance of all the electrodes correlates with dissolved oxygen concentrations except for a few cases in the FY 2014 impedance data. The polarization resistance decreased with increasing oxygen concentration. The polarization resistance of the electrodes under Condition 4 (i.e., 8.84 atmg [130 psig] in 4 percent H_2 plus 96 percent N_2) was highest compared to the other three conditions. The oxygen concentration was below the detection limit of the Oakton® oxygen meter under Condition 4 for the three electrodes. As expected, the polarization resistance of the electrodes, except for the UO_2 electrode, under Condition 1 (i.e., 1.02 atmg [15 psig] air) was lowest compared to the other three conditions. The polarization resistances for Condition 2 and 3 were in the range between Condition 1 and 4 for all of the SIMFUEL electrodes. There were two exceptions to the correlation between the dissolved oxygen concentration and polarization resistance. The first exception was for the UO_2 electrode under Condition 2. The second exception was for the 60 GW-day/MTU burnup equivalent SIMFUEL electrode under Condition 3. For the second exception, a difference of about 5 percent in the FY2014 impedance data could be associated with the noise level of the measurement.

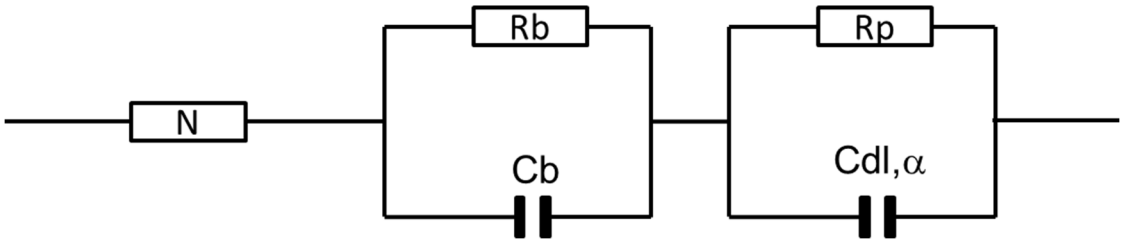

Figure 5-6. Electrical Circuit Used To Fit the Electrochemical Impedance Spectroscopy Data Presented in Figures 5-2, 5-3, and 5-4

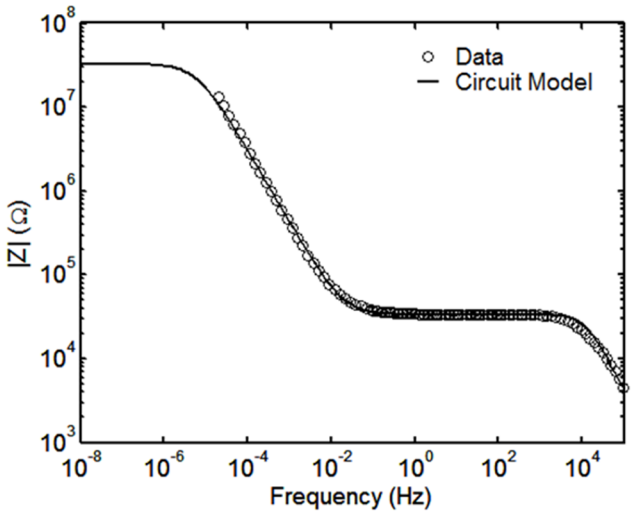

Figure 5-7. Circuit Model Fit to the Impedance Data for the UO_2 Electrode Under the Condition of 8.84 atmg [130 psig] of 4 percent H_2 Plus 96 percent N_2

The polarization resistance of all the electrodes correlates with the dissolved oxygen concentrations in the FY 2015 impedance data. The polarization resistance decreased with increasing oxygen concentration. The polarization resistance of the electrodes under Condition 4 {i.e., 8.84 atmg [130 psig] of 4 percent H_2 plus 96 percent N_2} was highest compared to the other three conditions. The oxygen concentration was below the detection limit of the oxygen meter under Condition 4.

5.1.3 Potentiodynamic Polarization Curves

The potentiodynamic polarization curves were measured for the three SIMFUEL electrodes. The polarization curves were measured for Condition 4 only after completion of the EIS measurements. The objective of these experiments was to compare the dissolution rates under the reducing conditions using multiple experimental techniques. The SIMFUEL electrodes in the corrosion cell were allowed to rest for 5 hours after the EIS measurements, and the potentiodynamic polarization curve was measured in the cathodic direction. The electrode was again allowed to rest at the open circuit potential for several hours after completion of the

cathodic potentiodynamic polarization sweep. Following this, the potentiodynamic polarization curve was measured in the anodic direction. The polarization curves were collected with a scan rate of 2 mV/sec, which is approximately 10 times greater than recommended for the linear polarization resistance method (ASTM International,

Table 5-3. Estimated Polarization Resistance of the SIMFUEL Specimen Under the Four Test Conditions (for FY 2014 Impedance Data)

Test Condition	Polarization Resistance (Ω)		
	UO_2	35 GW-day/MTU	60 GW-day/MTU
1. 1.02 atmg [15 psig] air	9.47×10^6	3.86×10^6	2.25×10^6
2. 1.02 atmg [15 psig] air and 8.84 atmg [130 psig] of 4 percent H_2 plus 96 percent N_2	8.28×10^6	5.60×10^6	2.44×10^6
3. 0.14 atmg [2 psig] air and 1.02 atmg [15 psig] of 4 percent H_2 plus 96 percent N_2 gas/ 0.70 atmg [10 psig] air and 1.02 atmg [15 psig] of 4 percent H_2 plus 96 percent N_2 gas*	1.40×10^7	5.30×10^6	2.80×10^6
4. 8.84 atmg [130 psig] of 4 percent H_2 plus 96 percent N_2	3.30×10^7	1.67×10^7	2.40×10^7

*FY 2014 experiments under Condition 3 were conducted with 0.14 atmg [2 psig] air and 1.02 atmg [15 psig] of 4 percent H_2 plus 96 percent N_2 gas

2014). It was necessary to use the higher scan rate because the signal to noise ratio for the data at the ASTM- recommended scan rate of 0.1667 mV/sec was too low to make any meaningful observations. The electrode potential data with time for the UO_2 SIMFUEL electrode is presented in Figure 5-8(a), and anodic and cathodic polarization curves are displayed in Figure 5-8(b). Similarly, the electrode potential data with time for the 35 GW-day/MTU SIMFUEL electrode is shown in Figure 5-9(a), and anodic and cathodic polarization curves are shown in Figure 5-9(b). The anodic and cathodic polarization curves in Figures 5-8(b) and 5-9(b) are used to estimate the SIMFUEL dissolution rates. Specifically, the curves are used to estimate the corrosion current densities which are used to estimate the dissolution rates.

5.2 Dissolution Rate Estimates

Posttest solution analyses included the collection of (1) electrochemical impedance spectroscopy data, (2) potentiodynamic polarization curve data, and (3) leaching test data.

5.2.1 Electrochemical Impedance Spectroscopy

The dissolution (corrosion) rates of the SIMFUEL specimens under the four conditions were estimated by fitting the impedance data to the electrical circuit in Figure 5-6, and obtaining the value of the polarization resistance (Rp). The polarization resistance was normalized with respect to the surface area of the electrode by multiplying the polarization resistance value by the electrode surface area (0.54 cm^2). Normalized polarization resistance values were used to obtain the corrosion current density (i_{corr}) using the Stern-Geary equation (1957):

$$i_{corr} = B / R_{pa} \quad (5\text{-}1)$$

where

i_{corr} — corrosion current density [A/cm^2]
R_{pa} — normalized polarization resistance [Ω-cm^2]
B — composite Tafel parameter [V]

Table 5-4. Estimated Polarization Resistance of the SIMFUEL Specimen Under the Four Test Conditions (for FY 2015 Impedance Data)

Test Condition	Polarization Resistance (Ω)		
	UO_2	35 GW-day/MTU	60 GW-day/MTU
1. 1.02 atmg [15 psig] air	—	4.53×10^6	—
2. 1.02 atmg [15 psig] air and 8.84 atmg [130 psig] of 4 percent H_2 plus 96 percent N_2	5.54×10^6	—	9.00×10^5
3. 0.14 atmg [2 psig] air and 1.02 atmg [15 psig] of 4 percent H_2 plus 96 percent N_2 gas/ 0.70 atmg [10 psig] air and 1.02 atmg [15 psig] of 4 percent H_2 plus 96 percent N_2 gas*	1.20×10^7 (run 1 and run 2)	1.90×10^7	1.07×10^7
4. 8.84 atmg [130 psig] of 4 percent H_2 plus 96 percent N_2	2.10×10^7 (run 1) 3.90×10^7 (run 2) 3.90×10^7 (run 3) 3.90×10^7 (run 4)	6.10×10^7	8.00×10^7 (run 1) 6.00×10^7 (run 2) 6.00×10^7 (run 3) 6.00×10^7 (run 4) 6.40×10^7 (run 5) 7.00×10^7 (run 6)

*FY 2015 experiments under Condition 3 were conducted with 0.70 atmg [10 psig] air and 1.02 atmg [15 psig] of 4 percent H_2 plus 96 percent N_2 gas

The value of the composite Tafel parameter B was selected to be 25 mV based on literature data (Grambow et al., 2000; Carbol et al., 2005). The dissolution rate was calculated from the polarization resistance using Faraday's law according to Eq. (5-2)

$$\text{Dissolution Rate } (D) = K_2 \times i_{corr} \times EW \qquad (5\text{-}2)$$

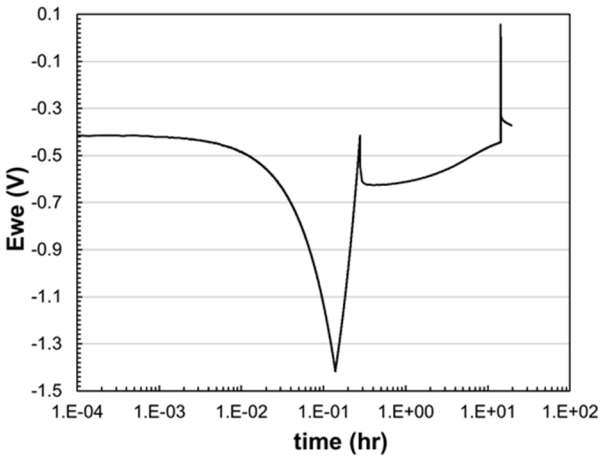

(a) Electrode Potential Versus Time

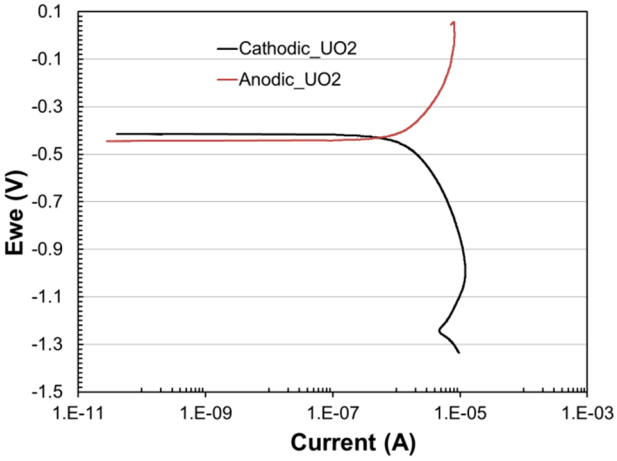

(b) Cathodic and Anodic Polarization Curves

Figure 5-8. (a) Electrode Potential With Respect to Saturated Calomel Electrode Versus Time and (b) Cathodic and Anodic Polarization Curves for the UO_2 SIMFUEL Electrode

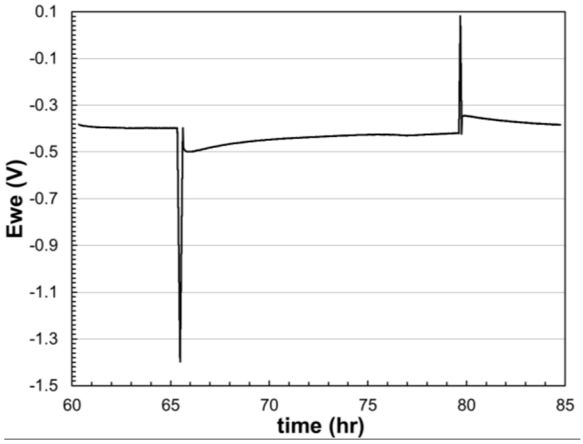

(a) Electrode Potential Versus Time

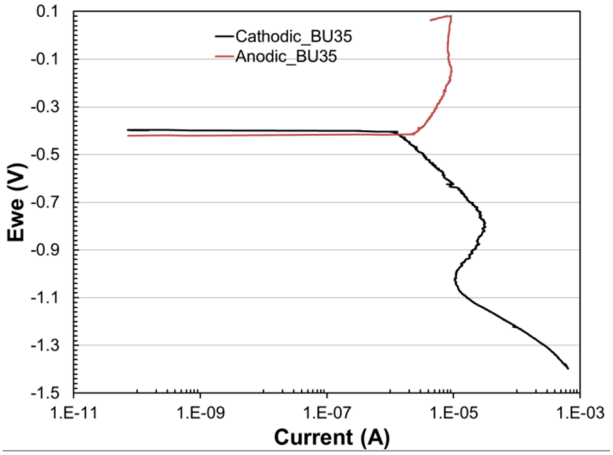

(b) Cathodic and Anodic Polarization Curves

Figure 5-9. (a) Electrode Potential With Respect to Saturated Calomel Electrode Versus Time and (b) Cathodic and Anodic Polarization Curves for the 35 GW-day/MTU SIMFUEL Electrode

where

K_2	—	constant [8.95×10^6 mg−cm^2/A/m^2/ day]
EW	—	equivalent weight for UO_2 = 33.75 assuming +6 and −2 valences for U and O, respectively

Tables 5-5 and 5-6 list the estimated dissolution rates of the three SIMFUEL electrodes under the four conditions for the FY 2014 and FY 2015 data, respectively. The SIMFUEL electrodes exhibited very high polarization resistance on the order of 10^6–10^7 Ω, indicating high corrosion resistance. Based on FY 2014 data, the estimated dissolution rates of the SIMFUEL electrodes

Table 5-5. Estimated Dissolution Rates of the SIMFUEL Specimens Under the Four Test Conditions From the Electrochemical Impedance Spectroscopy Data Collected in FY 2014

Test Condition	Dissolution Rates (mg/m^2/day)		
	UO_2	35 GW-day/MTU	60 GW-day/MTU
1. 1.02 atmg [15 psig] air	1.47	3.62	6.20
2. 1.02 atmg [15 psig] air and 8.84 atmg [130 psig] of 4 percent H_2 plus 96 percent N_2	1.69	2.49	5.72
3. 0.14 atmg [2 psig] air and 1.02 atmg [15 psig] of 4 percent H_2 plus 96 percent N_2/0.70 atmg [10 psig] air and 1.02 atmg [15 psig] of 4 percent H_2 plus 96 percent N_2*	1.00	2.63	4.98
4. 8.84 atmg [130 psig] of 4 percent H_2 plus 96 percent N_2	0.42	0.84	0.58

*FY 2014 experiments under Condition 3 were conducted with 0.14 atmg [2 psig] air and 1.02 atmg [15 psig] of 4 percent H_2 plus 96 percent N_2 gas

ranged from 0.42 to 6.2 mg/m^2/day. Based on the FY 2015 data the dissolution rates were in the range of 0.17 to 15.5 mg/m^2/day. Burnup and dissolved oxygen concentration are the two factors affecting the dissolution rates. . The dissolution rates increased with increasing burnup in the test conditions with oxygen (i.e., Conditions 1-3). Under Condition 4, the dissolution rate decreased with increasing burnup, except for the UO_2 electrode in FY 2014 data listed in Table 5-5. The result of one single run under Condition 4 for each SIMFUEL electrode in FY2014 differed from the expected trend, i.e., dissolution rate decreasing with increasing burnup. Therefore, Condition 4 experiments were extensively repeated in FY 2015. In the FY 2015 data, the average dissolution rate of the 60 GW-day/MTU electrode is the lowest under Condition 4, compared to the UO_2 and 35 GW-day/MTU electrodes. The burnup effect on the dissolution rate is consistent with the analyses by Forsyth (1997) under oxidizing conditions. Forsyth (1997) reported that the cumulative fractional release of radionuclides (i.e., Cs-137 and Sr-90) from SNF, increased with burnup almost linearly up to values of 40–45 GW-day/MTU under oxidizing conditions. Forsyth (1997) also reported that the fractional release of radionuclides (i.e., Cs-137 and Sr-90) decreased, as burnup further increased up to 49 GW-day/MTU (from 40–45 GW-day/MTU). However, the high burnup effect that Forsyth (1997)

reported may not be applicable, because there were additional microstructural changes in the SNF with high burnup. For example, Jung et al. (2013), and Thomas et al. (1992) reported the formation of a rim layer, which may also inhibit the dissolution rate of the SNF. The high burnup microstructural changes were not included when fabricating the SIMFUEL for the current analyses. Furthermore, the dissolution rate data is consistent with Trummer et al. (2008, 2009), who reported a decreasing dissolution rate with an increasing epsilon particle concentration under reducing conditions. Because the 60 GW-day/MTU electrode has the highest

Table 5-6. Estimated Dissolution Rates of the SIMFUEL Specimens Under the Four Test Conditions From the Electrochemical Impedance Spectroscopy Data Collected in FY 2015

Test Condition	Dissolution Rates ($mg/m^2/day$)		
	UO_2	35 GW-day/MTU	60 GW-day/MTU
1. 1.02 atmg [15 psig] air	—	3.08	—
2. 1.02 atmg [15 psig] air and 8.84 atmg [130 psig] of 4 percent H_2 plus 96 percent N_2	2.52	—	15.5
3. 0.14 atmg [2 psig] air and 1.02 atmg [15 psig] of 4 percent H_2 plus 96 percent N_2/0.70 atmg [10 psig] air and 1.02 atmg [15 psig] of 4 percent H_2 plus 96 percent N_2	1.16 (run 1, run 2)	0.74	1.30
4. 8.84 atmg [130 psig] of 4 percent H_2 plus 96 percent N_2	0.66 (run 1) 0.36 (run 2 to run 4)	0.23	0.17 (run 1) 0.23 (run 2 to run 4) 0.22 (run 5) 0.20 (run 6) Average = 0.21

*FY 2014 experiments under Condition 3 were conducted with 0.70 atmg [10 psig] air and 1.02 atmg [15 psig] of 4 percent H_2 plus 96 percent N_2 gas

concentration of epsilon particles, its dissolution rate was expected to be lowest among the three electrodes. Trummer et al. (2009) also reported that the noble metal particles (ε-particles) catalyze the oxidation of the UO_2 matrix by the oxidants H_2O_2 and O_2 under oxidizing conditions. Thus, the increased dissolution rates of the three SIMFUEL electrodes under Conditions 1–3 are also consistent with Trummer et al. (2009). Our SIMFUEL dissolution rates generally decreased with decreasing oxygen concentration, consistent with the inverse proportionality to normalized polarization resistance (R_{pa}) in Eqs. (5-1) and (5-2). The polarization resistance of an electrode under Condition 4 (i.e., 8.84 atmg [130 psig] of 4 percent H_2 plus 96 percent N_2) was lowest compared to the other three conditions as can be seen in both the FY 2014 and 2015 data. The oxygen concentration was below the detection limit of the Okton® oxygen meter

under Condition 4 for all three electrodes. The dissolution rate of electrodes under Condition 1 (i.e., 1.02 atmg [15 psig] air) was highest, except for the UO_2 electrode, compared to the other three conditions used in FY 2014. The oxygen concentration was highest under Condition 1. The dissolution rates obtained under Conditions 2 and 3 generally are between those obtained under Conditions 1 and 4. There are two exceptions to the correlation between the dissolved oxygen concentration and the dissolution rate:

(i) The first exception is for the UO_2 electrode, whose dissolution rate is slightly higher for Condition 2 compared to those obtained under Condition 1 (although the oxygen concentration in Condition 2 is lower than in Condition 1 in the FY 2014 data). This exception was not seen in the FY 2015 data.

(ii) The second exception was under Condition 3 for the 60 GW-day/MTU electrode (whose dissolution rate is slightly lower compared to those obtained under Condition 2 (even though the condition 3 oxygen concentration was higher than the Condition 2 oxygen concentration used to obtain the FY 2014 data). This exception also was not seen in the FY 2015 data.

Although the dissolution rate of the 35 GW-day/MTU electrode was lower under Condition 3 compared to those obtained under Condition 2, the Condition 3 oxygen concentration was higher than the Condition 2 oxygen concentration, used to obtain the FY 2014 data. It should be noted that the difference in the 35 GW-day/MTU condition 2 and 3 dissolution rates is only about 5 percent. Therefore, this observation is not considered an exception to the correlation between dissolution rate and the dissolved oxygen concentration in the solution. Furthermore, the dissolution rate under Condition 3 for the 35 GW-day/MTU electrode was 0.74 mg/m^2/day in the FY 2015 data, which is much lower than the 2.49 mg/m^2/day dissolution rate obtained under Condition 2 in FY 2014 . This resolved the discrepancy observed in the FY 2014 data under Conditions 2 and 3 for the 35 GW-day/MTU electrode.

5.2.2 Potentiodynamic Polarization Curves

The polarization curves for the UO_2 and 35 GW-day/MTU electrodes were analyzed to obtain the corrosion potential and the corrosion current for Condition 4. For the UO_2 electrode, the anodic polarization curve was shifted down by 28 mV. The resulting graph of the anodic and cathodic polarization curves is displayed in Figure 5-10(a). The Tafel regions on both anodic and cathodic curves were in the low current region and were steep with close to 90-degree slope for the change in current versus change in potential ratio, so it was not possible to estimate the anodic and cathodic Tafel slopes with a high degree of certainty. Therefore, the corrosion current was visually determined, and is marked by a green circle in Figure 5-10(a). The corrosion current was estimated to be 2×10^{-10} A. The estimated dissolution rate for this value of the corrosion current density is 0.11 mg/m^2/day.

For the 35 GW-day/MTU electrode, the anodic polarization curve was shifted down by 22 mV. The resulting graph of the anodic and cathodic polarization curves is shown in Figure 5-10(b). Here again, the Tafel regions on both anodic and cathodic curves were in the low current region and were steep with close to 90-degree slope for the change in current versus change in potential ratio, so it was not possible to estimate the anodic and cathodic Tafel slopes with a high degree of certainty. Therefore, the corrosion current was visually determined, and is marked by a green circle in Figure 5-10(b). The corrosion current was estimated to be 10^{-10} A. The estimated dissolution rate for this value of the corrosion current density is 0.06 mg/m^2/day.

The potentiodynamic polarization method was found to be not very effective technique to estimate the corrosion current density because of steep anode and cathodic Tafel slopes.

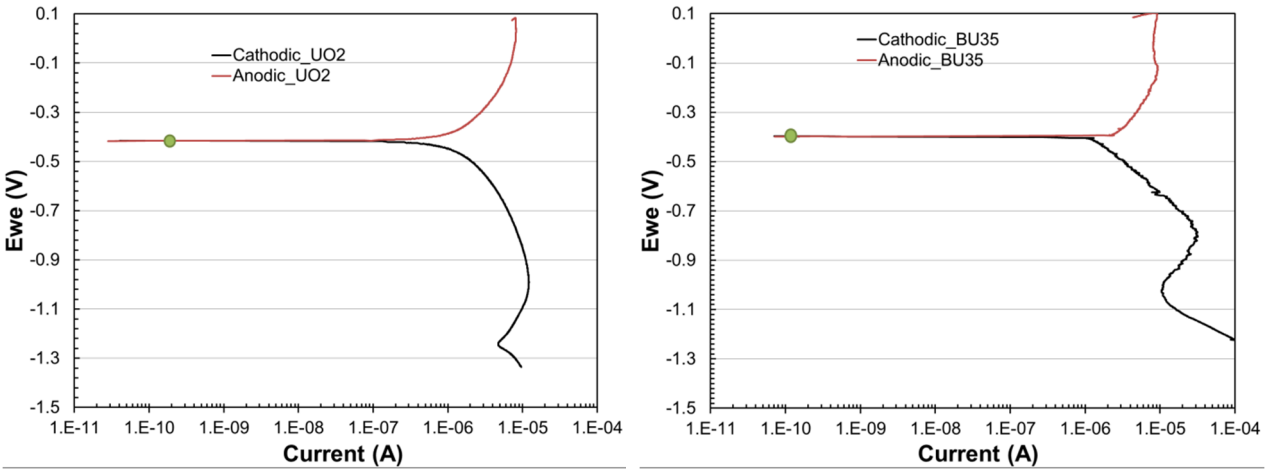

(a) UO_2 **(b) 35 GW-day/MTU**

Figure 5-10. Adjusted Anodic and Cathodic Polarization Curves for (a) UO_2 and (b) 35 GW-day/MTU SIMFUEL Electrodes

5.2.3 Leaching Tests

Two sets of leaching experiments were conducted. The first sets leaching experiments were conducted for 31 days and the second ones were conducted for 84 days. It is noted that the fresh soulion was used for each test. The test solutions were collected after completion of the experiments and analyzed using the ICP-AES. Uranium concentration data obtained from analysis of the leachate is listed in Table 5-7. The data were used to estimate the dissolution rate according to the following equation

$$\text{Dissolution Rate } (D) = 2.5 \times 10^{-2}\, C_U/(S_{pellet} \times t_{exposure\_days}) \qquad (5\text{-}3)$$

where

C_U — Uranium concentration [mg/L]
S_{pellet} — Surface area of the pellet [m^2]
$t_{exposure\_days}$ — Exposure time [days]

The numerical factor on right hand side of Eq. (5-3) accounts for the 25 mL of the granitic water used in each experiment. The estimated surface area of each pellet is approximately 3.44×10^{-4} m^2 [3.70×10^{-2} ft^2]. The dissolution rates, estimated using the surface area, uranium leachate concentration, and exposure time, are listed in Table 5-8.

The 31-day test dissolution rates are higher than they are for the 84-day test for both 35 and 60 GW-day/MTU samples. Specifically, the 31-day test dissolution rate is 13 times higher than the 84-day test for the 35 GW-day/MTU sample, but the 31-day test dissolution rate is only 2.5 times higher than the 84-day test dissolution rate for the 60 GW-day/MTU sample. This is probably due to better control of the hydrogen partial pressure in the 84-day test compared to the 31-day test. It is further observed that the dissolution rate of 35 GW-day/MTU sample is

higher than the dissolution rate of the 60 GW-day/MTU sample in the 31-day test, but the trend is opposite in the 84-day test. It is conjuctered that this discrepancy could be due to non-uniform surface distribution of the epsilon particles in the 35 GW-day/MTU and 60 GW-day/MTU samples. It is possible that surface density of the epsilon particles in the 35 GW-day/MTU sample was more compared to the 60 GW-day/MTU sample. The lower surface density of the epsilon particles in the 60 GW-day/MTU sample could have led to higher dissolution rate in the 60 GW-day/MTU sample compared to the 35 GW-day/MTU sample in the 84-day test.

Table 5-7. Uranium Concentrations Obtained from Chemical Analyses of the Leachate Collected After Leaching Tests

Species	31-day Exposure Test		84-day Exposure Test	
	35 GW-day/MTU Sample Leachate	60 GW-day/MTU Sample Leachate	35 GW-day/MTU Sample Leachate	60 GW-day/MTU Sample Leachate
Uranium (mg/L)	1.28×10^{-1}	6.04×10^{-2}	2.72×10^{-2}	6.64×10^{-2}

Table 5-8. Estimated Dissolution Rates of the SIMFUEL Specimens Used in the Leaching Test

Test Exposure Time (days)	Dissolution Rates (mg/m^2/day)	
	35 GW-day/MTU	60 GW-day/MTU
31	0.31	0.15
84	2.4×10^{-2}	6.1×10^{-2}

6 SUMMARY AND DISCUSSION

The values reported in the literature on the dissolution rate of spent nuclear fuel (SNF) under reducing conditions vary widely. One set of studies concludes that SNF dissolution is completely suppressed in the presence of hydrogen, while other studies suggest that the effect is more gradual. If gradual, there is no consensus on the extent of decrease in the dissolution rates due to hydrogen. Some studies indicate that the dissolution rates decrease by up to a factor of 10 in the presence of hydrogen under reducing conditions compared to the oxidizing conditions. Other studies conclude that hydrogen decreases the dissolution rates by a factor of 1,000 or more in reducing conditions compared to oxidizing conditions. There is consensus that SNF dissolution is dependent on the redox state (lower dissolution rates are attained in reducing conditions), but there is no agreement on the extent of the decrease in the reducing conditions compared to the oxidizing conditions.

In this work, dissolution of SIMFUEL in contact with a simulated saline groundwater (with chemical composition based on published compositions for deep groundwaters in granitic rocks) was measured using electrochemical methods. SIMFUEL is an unirradiated, simulated SNF containing chemically equivalent nonradioactive surrogate elements for fission products, activation products, and actinides. The experiments involved three SIMFUEL types: (i) pure UO_2, (ii) 35 GW-day/MTU burnup equivalent, and (iii) 60 GW-day/MTU burnup equivalent. The electrochemical experiments were conducted by immersing one of the three SIMFUEL specimens as a working electrode in a granitic groundwater solution. The solution had a near-neutral pH and elevated concentrations of Na^+ and Cl^- ions. Further, the solution was purged with various combinations of compressed air and a mixture of 4 percent H_2 plus 96 percent N_2. For each SIMFUEL specimen, experiments were conducted under the following four conditions: (1) groundwater saturated with oxygen {by bubbling the solution with 1.02 atmg [15 psig] compressed air}, (2) groundwater saturated with oxygen and hydrogen {by bubbling the solution with 1.02 atmg [15 psig] compressed air and an 8.84 atmg [130 psig] of 4 percent H_2 plus 96 percent N_2 gas mixture}, (3) groundwater unsaturated with oxygen and hydrogen {by bubbling the solution either with 0.14 atmg [2 psig] compressed air and a 1.02 atmg [15 psig] 4 percent H_2 plus 96 percent N_2 gas mixture; or with 0.70 atmg [10 psig] compressed air and a 1.02 atmg [15 psig] 4 percent H_2 plus 96 percent N_2 gas mixture}, and (4) groundwater with dissolved hydrogen {by bubbling the solution with an 8.84 atmg [130 psig] 4 percent H_2 plus 96 percent N_2 gas mixture}. With regard to Condition 3, the experiments in fiscal year (FY) 2014 were conducted with 0.14 atmg [2 psig] compressed air and a 1.02 atmg [15 psig] 4 percent H_2 plus 96 percent N_2 gas mixture. In FY 2015, condition 3 experiments were conducted with 0.70 atmg [10 psig] compressed air and a 1.02 atmg [15 psig] 4 percent H_2 plus 96 percent N_2 gas mixture. The test conditions were based on the exit pressure of the gases from the gas tanks and not on the gas pressure in the test cell. Electrochemical impedance spectroscopy was used to record the impedance of the working electrode at various combinations of the purging rate of gas at a solution temperature of 22 ± 2 °C [72 ± 4 °F]. The impedance data were analyzed using an equivalent electrical circuit to estimate dissolution rates. Potentiodynamic polarization curves of the UO_2 and 35 GW-day/MTU electrode also were collected and visually analyzed to estimate dissolution rates.

In addition to electrochemical tests, leaching experiments (using leachate concentrations) were conducted to determine dissolution rates. The objective of these experiments was to measure the dissolution rate under higher hydrogen fugacity {compared to 2.0×10^{-2} to 4.0×10^{-2} atm [0.29–0.59 psi] of the electrochemical tests}, causing the dissolved hydrogen concentration to be near 1 mM. The target dissolved hydrogen concentration can be achieved when the fugacity of hydrogen is close to 1.3 atm [19.1 psi]. These experiments were conducted using two pipe

reactors that were pressurized with 4 percent H_2, plus a 96 percent N_2 gas mixture at approximately 450 psig [30.6 atm]. These experiments were run for 31 and 84 days, and the test solutions were collected after completion of the experiments. The test solutions were subsequently analyzed for uranium concentrations. The 31-day test dissolution rates of the 35 and 60 GW-day/MTU sample were 0.31 and 0.15 mg/m^2/day, respectively. The 84-day test dissolution rates of the 35 and 60 GW-day/MTU sample were 2.4×10^{-2} and 6.1×10^{-2} mg/m^2/day, respectively. It is observed that the dissolution rates of the 35 and 60 GW-day/MTU samples are approximately 13 and 2.5 times higher, respectively, in the 31-day test than in the 84-day test. This is probably due to better control of the hydrogen partial pressure in the 84-day test compared to the 31-day test. The SIMFUEL dissolution rates obtained from different methods are summarized in Table 6-1.

Table 6-1. Summary of the Dissolution Rates Obtained from Electrochemical and Leaching Tests

Test Method	Test Condition	Dissolution Rates (mg/m^2/day)*		
		UO_2	35 GW-day/MTU	60 GW-day/MTU
Electrochemical Impedance Spectroscopy	1. 1.02 atmg [15 psig] air	1.47	3.62, 3.08	6.20
	2. 1.02 atmg [15 psig] air and 8.84 atmg [130 psig] of 4 percent H_2 plus 96 percent N_2	1.69, 2.52	2.49	5.72, 15.5
	3. 0.14 atmg [2 psig] air and 1.02 atmg [15 psig] of 4 percent H_2 plus 96 percent N_2/0.70 atmg [10 psig] air and 1.02 atmg [15 psig] of 4 percent H_2 plus 96 percent N_2	1.00, 1.16	2.63, 0.74	4.98, 1.30
	4. 8.84 atmg [130 psig] of 4 percent H_2 plus 96 percent N_2	0.42, 0.66, 0.36	0.84, 0.23	0.58, 0.17, 0.23, 0.22, 0.20
Potentiodynamic Polarization	1. 8.84 atmg [130 psig] of 4 percent H_2 plus 96 percent N_2	0.11	0.06	–
Leaching (test solution pressurized to approximately 30.6 atmg [450 psig])	1. 31-day test	–	0.31	0.15
	2. 84-day test	–	2.4×10^{-2}	6.1×10^{-2}

*Multiple values in a cell are from repeat runs

The dissolution rate of the 35 GW-day/MTU sample is higher than the dissolution rate of the 60 GW-day/MTU sample in the 31-day test, but the trend is opposite in the 84-day test. This

discrepancy could be due to relatively non-uniform surface distribution of the epsilon particles in the 35 GW-day/MTU and 60 GW-day/MTU samples. It is possible that the surface density of the epsilon particles in the 35 GW-day/MTU sample was more compared to the 60 GW-day/MTU sample in the 84-day test. The lower surface density of the epsilon particles in the 60 GW-day/MTU sample could have led to higher dissolution rate in the 60 GW-day/MTU sample compared to the 35 GW-day/MTU sample in the 84-day test.

The estimated dissolution rates of the SIMFUEL electrodes in the electrochemical experiments ranged from 0.06–15.5 mg/m^2/day under the four groundwater conditions. Based on the experimental data, two primary factors clearly affected the dissolution rates: (i) burnup and (ii) the dissolved oxygen concentration. Because the dissolved hydrogen concentration was not measured directly, its effect on the dissolution rate was estimated using Henry's law. The dissolved hydrogen concentration was estimated to be 15.5 µmole/L under Conditions 2 and 3, and 31 µmole/L under Condition 4.

Under Condition 4, the dissolution rate of the 60 GW-day/MTU burnup equivalent SIMFUEL electrode was lower than the dissolution rate of the 35 GW-day/MTU burnup SIMFUEL electrode. The dissolution rate of the 60 GW-day/MTU electrode was lower compared to the 35 GW-day/MTU, but higher than the UO_2 electrode in the FY2014 data. Similarly, the average dissolution rate of the 60 GW-day/MTU electrode was lower compared to the 35 GW-day/MTU electrode in the FY2015 data. The noble element concentration was higher in the 60 GW-day/MTU sample than in the 35 GW-day/MTU sample. The higher noble element concentration in the 60 GW-day/MTU sample compared to 35 GW-day/MTU should decrease the matrix dissolution as a result of enhanced reduction of the oxidizing species and reduction of any oxidized UO_2 particles present in the solution.

SIMFUEL dissolution rates decreased with decreasing dissolved oxygen concentration. The dissolution rate of an electrode under groundwater Condition 1 {i.e., 1.02 atmg [15 psig] air} was highest compared to the other three groundwater conditions, except for the UO_2 electrode in FY2014. The oxygen concentration was highest in groundwater under Condition 1 for both FY2014 and 2015 data. The dissolution rates in the groundwater for Conditions 2 and 3 are generally between those for Conditions 1 and 4 for a given electrode. There are two exceptions to the correlation between the dissolved oxygen concentration and the dissolution rate in FY2014. The first exception is under Condition 2 for the UO_2 electrode, whose dissolution rate is slightly higher in the condition 2 groundwater than for the Condition 1 groundwater (although the oxygen concentration in the Condition 2 groundwater is lower than the oxygen concentration in the Condition 1 groundwater). The second exception is under groundwater Condition 3 for the 60 GW-day/MTU electrode, which had a slightly lower dissolution rate than it had under groundwater Condition 2, even though the groundwater Condition 3 oxygen concentration is higher than the groundwater Condition 2 oxygen concentration. These two exceptions were not observed in the FY2015 data.

The current experimental work in this report suggests that the SNF dissolution rates depend on the dissolved oxidizing species concentration along with the hydrogen concentration under reducing conditions in a geological repository. More specifically, the experimental results for the three SIMFUEL specimens indicate that the dissolution rate (i) increases with increasing burnup and (ii) decreases with decreasing oxygen concentration under the oxidizing condition. Under reducing conditions, the dissolution rate decreases with increasing burnup.

The dissolution rate data acquired under the reducing condition (groundwater Condition 4 experiments) were analyzed to estimate the fractional release rate. The fractional release rate is related to dissolution rate according to the following equation:

$$F \times V \times \rho = D \times S \times 365 \text{ day/yr} \quad (6\text{-}1)$$

where

F	—	fractional release rate [1/yr]
V	—	volume of fuel fragment [m^3]
ρ	—	fuel density [mg/m^3]
D	—	dissolution rate [$mg/m^2/day$]
S	—	surface area of fuel fragment [m^2]

The dissolution rate values, D, were experimentally measured. The density of the spent fuel is approximately 10^{10} mg/m^3 (Jung et al., 2013). For surface area and volume, a cubic fuel fragment, with each side equal to 3 mm, was assumed. This assumption is based on fragmentation of fuel pellets into 10–30 pieces during reactor operation (Jung et al., 2013). The cubic fuel fragment with 3 mm each side is equivalent to a fuel pellet with typical dimensions fragmenting into approximately 10 pieces.

The parameter values were input into Eq. (6-1), and the following relationship was obtained between the fractional release rate and the dissolution rate:

$$F = D \times 7.3 \times 10^{-5} \quad (6\text{-}2)$$

Using Equation (6-2), the dissolution rate should be less than 0.0137 $mg/m^2/day$ for the fractional release rate to be less than 10^{-6}/yr. The lowest dissolution rate observed in this study was 0.024 $mg/m^2/day$. This release rate is approximately two times higher than the rate associated with a fractional release rate of 10^{-6}/yr. Note that the fractional release rate is dependent on the size of fuel fragment which is assumed to be 3 mm cube. The fractional release rate would be lower for a fuel fragment larger than 3 mm cube, and higher for a fuel fragment smaller than a 3 mm [0.12 inch] cube.

The experimental results under the low fugacity of hydrogen with a dissolved hydrogen concentration of about 31 µmole/L indicate that dissolved hydrogen is unlikely to completely suppress SNF dissolution in reducing conditions (as claimed in the literature). However, it is likely to significantly decrease SNF dissolution rates. The leaching experiments conducted with dissolved hydrogen concentration of approximately 1 mmole/L at a hydrogen fugacity of approximately 1.3 atm [19.1 psi] also showed nonzero dissolution rates. The leaching experiments suggest that dissolved hydrogen of 1 mmole/L is unlikely to completely suppress SNF dissolution under reducing conditions. The dissolution rates decreased by one to three orders of magnitude, i.e., by a factor of 10 to 1000, under reducing conditions compared to the oxidizing condition. The decrease in dissolution rate under the reducing conditions is found to be consistent with some literature that reported a decrease by a factor of 10-1000 compared to oxidizing conditions. However, the absolute values of the dissolution rates under the reducing conditions are not sufficient to achieve the fraction release rate of 10^{-6}/year for a fragmented fuel pellet with fuel fragments sizes equivalent to 3 mm [0.12 inch] cube or less.

The experimental data do not show a clear dependence of the dissolution rate under reducing conditions on the extent of burnup (burnup is emulated in the SIMFUEL by changing the chemical composition of the alloy and the density of epsilon particles). Information in the

literature indicates that increasing the burnup should cause the SNF dissolution under the reducing condition to decrease (because the epsilon particle concentration increases with burnup, and epsilon particles facilitate the reduction of oxidants in solution which would otherwise enhance SNF dissolution). Thus, it was expected in the tests that the dissolution rate would decrease with increasing epsilon particle concentration. In the electrochemical and 31-day leaching tests, the 60 GW-day/MTU SIMFUEL sample dissolution rates were indeed less than the 35 GW-day/MTU SIMFUEL rates, but the opposite trend was observed in the 84-day leaching test. The lack of a clear trend could be due to the non-uniform distribution of the epsilon particles in the SIMFUEL. The burnup is expected to increase the epsilon particle concentration, but the SIMFUEL fabrication process does not guarantee uniform distribution of the epsilon particle. It is possible that the surface density of the epsilon particles in the 35 GW-day/MTU sample was greater than the density of the 60 GW-day/MTU sample. In the 35 GW-day/MTU sample, the epsilon particles tended to be aggregated and clustered (see Figure 4-1); thus, even though the total mass of epsilon particles was higher in the 60 GW-day/MTU sample, the corresponding effective surface density may have been lower. Differences in the effective surface density of epsilon particles may explain why a decrease in the SNF dissolution rates with increasing simulated burnup could not be confirmed.

7 REFERENCES

ASTM International. ASTM G59–97 (Reapproved 2014), "Standard Test Method for Conducting Potentiodynamic Polarization Resistance Measurements." West Conshohocken, Pennsylvania: ASTM. 2014.

Bonin, B., M. Colin, and A. Dutfoy. "Pressure Building During the Early Stages of Gas Production in a Radioactive Waste Repository." *Journal of Nuclear Materials*. Vol. 281. pp. 1–14. 2000.

Broczkowski, M.E., J.J. Noël, and D.W. Shoesmith. "The Inhibiting Effects of Hydrogen on the Corrosion of Uranium Dioxide Under Nuclear Waste Disposal Conditions." *Journal of Nuclear Materials*. Vol. 346. pp. 16–23. 2005.

Carbol, P., J. Cobos-Sabathe, J.-P. Glatz, C. Ronchi, V. Rondinella, D.H. Wegen, T. Wiss, A. Loida, V. Metz, B. Kienzler, K. Spahiu, B. Grambow, and J. Quiones. "The Effect of Dissolved Hydrogen on the Dissolution of ^{233}U Doped UO_2(s), High Burn-up Spent Fuel and MOX Fuel." A.M.E. Valiente, Tech. Rep. TR-05-09. Svensk Kärnbränslehantering AB. Stockholm, Sweden: Swedish Nuclear Fuel and Waste Management Company. 2005.

Cuss, R.J., J.F. Harrington, and D.J. Noy. "Large Scale Gas Injection Test (LASGIT) Performed at the Äspö Hard Rock Laboratory: Summary Report 2008." Technical Report TR–10–38. Stockholm, Sweden: Swedish Nuclear Fuel and Waste Management Co. February 2010.

de Pablo, J., I. Casas, J. Gim'enez, M. Molera, M. Rovira, L. Duro, and J. Bruno. "The Oxidative Dissolution Mechanism of Uranium Dioxide. I. The Effect of Temperature in Hydrogen Carbonate Medium." *Geochimica et Cosmochimica Acta.* Vol. 63. pp. 3,097–3,103. 1999.

Duro, L., S. El Aamrani, M. Rovira, J. de Pablo, and J. Bruno. "Study of the Interaction Between U(VI) and the Anoxic Corrosion Products of Carbon Steel." *Applied Geochemistry.* Vol. 23. pp. 1,094–1,100. 2008.

El Aamrani, S., J. Gimenez, M. Rovira, F. Seco, M. Grive, J. Bruno, L. Duro, and J. de Pablo. "A Spectroscopic Study of Uranium(VI) Interaction with Magnetite." *Applied Surface Science.* Vol. 253. pp. 8,794–8,797. 2007.

Eriksen, T., U-B Eklund, L. Werme, and J. Bruno. "Dissolution of Irradiated Fuel: A Radiolytic Mass Balance Study." *Journal of Nuclear Materials*. Vol. 227. pp. 76–82. 1995.

Ferry, C., C. Poinssot, V. Broudic, L. Desgranges, P. Gargia, C. Jegou, P. Lovera, P. MARIMBEAU, J.P. Piron, A. Poulesquen, and D, Roudil. "Synthesis on the Spent Fuel Long Term Evolution." CEA-R-6084. CEA Saclay, Direction De L'enrgie Nucleaire. Department De Physico-Chimie. Commissariat a l'Energie Atomique. France. 2005.

Ferry, C., C. Poinssot, C. Cappelaere, L. Desgranges, C. Jegou, F. Miserque, J.P. Piron, D. Roudil, and J.M. Gras. "Specific Outcomes of the Research on the Spent Fuel Long-Term Evolution in Interim Dry Storage and Deep Geological Disposal." *Journal of Nuclear Materials.* Vol. 352. pp. 246–253. 2006.

Forsyth, R. "An Evaluation of Results From the Experimental Programme Performed in the Studsvik Hot Cell Laboratory." SKB TR 97-25. Stockholm, Sweden: Swedish Nuclear Fuel and Waste Management Company. 1997.

Gascoyne, M. "Reference Groundwater Composition for a Depth of 500 m in the Whiteshell Research Area–Comparison with Synthetic Groundwater WN-1." Report AECL TR-463. Pinawa, Canada: Atomic Energy of Canada Limited. 1988.

Graham, C.C. and J.F. Harrington. "Final Report of FORGE 3.2.1: Key Gas Migration Process in Compact Bentonite." British Geological Survey Internal Report. CR/14/064. 51pp. 2014.

Grambow, B., C. Ferry, I. Casas, J. Bruno, J. Quinones, and L. Johnson. "Spent Fuel Waste Disposal: Analyses of Model Uncertainty in the MICADO Project." *Energy Procedia.* Vol. 7. pp. 487–494. 2011.

Grambow, B., A. Loida, A. Martinez-Esparza, P. Diaz-Arocas, J. de Pablo, J.-L. Paul, G. Marx, J.-P Paul, G. Marx, J.-P. Glatz, K. Lemmens, K. Ollila, and H. Christensen. "Source Term for Performance Assessment of Spent Fuel as a Waste Form." EUR 19140. Luxembourg, Germany: European Atomic Energy Community. 2000.

Grandstaff, D.E. "A Kinetic Study of the Dissolution of Uraninite." *Economic Geology*. Vol. 71. pp. 1,493–1,506. 1976.

Grenthe, I., F. Diego, F. Salvatore, and G. Riccio. "Studies on Metal Carbonate Equilibria. Part 10. A Solubility Study of the Complex Formation in the Uranium(VI)–Water–Carbon Dioxide (g) System at 25 °C." *Journal of Chemical Society.* Vol. 11. pp. 2,439–2,443. 1984.

Jegou, C., B. Muzeau, V. Broudic, S. Peuget, A. Poulesquen, D. Roudil, and C. Corbel. "Effect of External Gamma Irradiation on Dissolution of the Spent UO_2 Fuel Matrix." *Journal of Nuclear Materials.* Vol. 345. pp. 62–82. 2005.

Johnson, L.H. and P.A. Smith. "The Interaction of Radiolysis Products and Canister Corrosion Products and the Implications for Spent Fuel Dissolution and Radionuclide Transport in a Repository for Spent Fuel." NAGRA NTB Technical Report 00-04. 2000.

Jung, H., T. Ahn, K. Axler, R. Pabalan, and D. Pickett. "Corrosion of SIMFUEL in Aerated Carbonate Solution Containing Calcium and Silicate." San Antonio, Texas: Center for Nuclear Waste Regulatory Analyses. 2011.

Jung, H., P. Shukla, T. Ahn, L. Tipton, K. Das, X. He, and D. Basu. "Extended Storage and Transportation: Evaluation of Drying Adequacy." ML1316A039. San Antonio, Texas: Center for Nuclear Waste Regulatory Analyses. 2013.

King, F. "Overview of a Carbon Steel Container Corrosion Model for a Deep Geological Repository in Sedimentary Rock." TR–2007–01. Toronto, Canada: Nuclear Waste Management Organization (NWMO). 2007.

Kursten, B., E. Smailos, I. Azkarate, L. Wermer, N.R. Smart, and G. Santarini. "COBECOMA, State-of-the-Art Document on the Corrosion Behavior of Container Materials." Contract N° FIKW–CT–20014–20138 Final Report. Luxembourg, Germany: European Commission. 2004.

Loida, A., V. Metz, B. Kienzler, and H. Geckeis. "Radionuclide Release From High Burnup Spent Fuel During Corrosion in Salt Brine in the Presence of Hydrogen Overpressure." *Journal of Nuclear Materials*. Vol. 346. pp. 24–31. 2005.

Lucuta, P.G., R.A. Verrall, H.J. Matzke, and B.J. Palmer. "Microstructural Features of SIMFUEL–Simulated High-Burnup UO_2-Based Nuclear Fuel." *Journal of Nuclear Materials*. Vol. 178. pp. 48–60. 1991.

McMurry, J. "Synthesis of Groundwater Test Solutions." Scientific Notebook 1228E. San Antonio, Texas: Center for Nuclear Waste Regulatory Analyses. pp. 1–39. 2014.

McMurry, J. "Reference Water Compositions for a Deep Geologic Repository in the Canadian Shield." Report OPG 06819-REP-01200-10135-R01. Toronto, Canada: Ontario Power Generation. 2004.

Marx, G. "Source Term for Performance Assessment of Spent Fuel as a Waste Form." in Grambow, B. et al. EUR 19140. 2000.

Martin, T., S. Nilson, and M. Johnson. "On the Effects of Fission Product Noble Metal Inclusions on the Kinetics of Radiation Induced Dissolution of Spent Nuclear Fuel." *Journal of Nuclear Materials*. Vol. 378. pp. 55–59. 2008.

MacDonald, D.D. "Kramers-Kronig Transformation of Constant Phase Impedances." *Journal of the Electrochemical Society.* Vol. 137. pp. 3,303–3,307. 1990.

NWMO. "Used Fuel Repository Conceptual Design and Postclosure Safety Assessment in Crystalline Rock." Pre-Project Report NWMO TR-2012-16. Toronto, Canada: Nuclear Waste Management Organization. 2012.

Ollila, K., E. Myllykylä, M. Tanhua-Tyrkkö, and T. Lavonen. "Dissolution Rate of Alpha-Doped UO_2 in Natural Groundwater." *Journal of Nuclear Materials.* Vol. 442. pp. 320–325. 2013.

Oversby, V.M. and V.M.O. Konsult. "Uranium Dioxide, SIMFUEL, and Spent Fuel Dissolution Rates—A Review of Published Data." A.M.E. Valiente. Tech. Rep. TR-99-22. Svensk Kärnbränslehantering AB. Stockholm, Sweden: Swedish Nuclear Fuel and Waste Management Company. 1999.

Park, G.I., J.W. Lee, Y.W. Lee, and K.C. Song. "Effect of Impurities on the Microstructure of Dupic Fuel Pellets Using the SIMFUEL Techniques." *Nuclear Engineering and Technology.* Vol.40, Issue No.3. pp. 191–198. 2008.

Pierce, E.M., J.P. Icenhower, R.J. Serne, and J.G. Catalano. "Experimental Determination of UO_2 (cr) Dissolution Kinetics: Effects of Solution Saturation State and pH." *Journal of Nuclear Materials*. Vol. 345. pp. 206–218. 2005.

Poinssot, C., C. Ferry, M. Kelm, B. Grambow, A. Martinez, L. Johnson, Z. Andriambololona, J. Bruno, C. Cachoir, J.M. Cavedon, H. Christensen, C. Corbel, C. Jegou, K. Lemmens, A. Loida, P. Lovera, F. Miserque, J. de Pablo, A. Poulesquen, J. Quinones, V. Rondinella, K. Spahiu, and D.H. Wegen. "Spent Fuel Stability Under Repository Conditions—Final Report of the European Project." European Commission, 5th Euratom Framework Programme 1998-2002. 2005.

Poinssot, Ch., P. Toulhoat, J.P. Grouiller, J. Pavageau, J.P. Piron, M. Pelletier, Ph. Dehaudt, Ch. Cappelaere, R. Limon, L. Desgranges, Ch. Jegou, C. Corbel, S. Maillard, M.H. Faure, J.C. Cicariello, and M. Masson. "Synthesis on the Long Term Behavior of the Spent Nuclear Fuel." CEA–R–5958. Saclay, France: Commissariat à L'Énergie Atomique. 2001.

Rollin, S., K. Spahiu, and U.-B. Eklund. "Determination of Dissolution Rates of Spent Fuel in Carbonate Solutions Under Different Redox Conditions with a Flow-Through Experiment." *Journal of Nuclear Materials.* Vol. 297. pp. 231–243. 2001.

Rondinella, V. and Hj. Matzke. "Leaching of SIMFUEL in Simulated Granite Water Comparison to Results in Demineralized Water." *Journal of Nuclear Materials*. Vol. 238. pp. 44–57. 1996.

Roth, O. and M. Jonsson. "Oxidation of UO_2(s) in Aqueous Solution." *Central European Journal of Chemistry.* Vol. 6, Issue 1. pp. 1–14. 2008.

Santos, B.G., J.J. Noel, and D.W. Shoesmith. "The Influence of Calcium Ions on the Development of Acidity in Corrosion Product Deposits on SIMFUEL, UO_2." *Journal of Nuclear Materials*. Vol. 350. pp. 320–331. 2006a.

Santos, B.G., J.J. Noel, and D.W. Shoesmith. "The Influence of Silicate on the Development of Acidity in Corrosion Product Deposits on SIMFUEL (UO_2)." *Corrosion Science*. Vol. 48. pp. 3,852–3,868. 2006b.

Shoesmith, D.W. "The Role of Dissolved Hydrogen on the Corrosion/Dissolution of Spent Nuclear Fuel." NWMO TR-2008-19. Toronto, Ontario, Canada: Nuclear Waste Management Organization. 2008.

Shoesmith, D.W. "Used Fuel and Uranium Dioxide Dissolution Studies—A Review." NWMO TR-2007-03. Toronto, Ontario, Canada: Nuclear Waste Management Organization. 2007.

Shoesmith, D.W. "Fuel Corrosion Processes Under Waste Disposal Conditions." *Journal of Nuclear Materials*. Vol. 282, Issue 1. pp. 1–31. 2000.

Shoesmith, D.W. and S. Sunder. "Validation of an Electrochemical Model for the Oxidative Dissolution of Used CANDU Fuel." *Journal of Nuclear Materials*. Vol. 257. pp. 89–98. 1998.

Shoesmith, D.W., S. Sunder, M.G. Bailey, and N.H. Miller. "Corrosion of Used Nuclear Fuel in Aqueous Perchlorate and Carbonate Solutions." *Journal of Nuclear Materials*. Vol. 227. pp. 287–299. 1996.

Shukla, P.K. *Stationary Hemispherical Electrode Under Submerged Jet Impingement and Validation of the Measurement Model Concept for Impedance Spectroscopy*. Ph.D. Dissertation. Gainesville, Florida: University of Florida. 2004.

Spahiu, K., J. Devoy, D. Cui, and D. Lundstorm. "The Reduction of U(VI) by Near Field Hydrogen in the Presence of UO_2(s)." *Radiochimica Acta*. Vol. 92. pp. 625−629. 2004.

Stern, M. and A.L. Geary. "Electrochemical Polarization: 1. A Theoretical Analysis of the Shape of Polarization Curves." *Journal of the Electrochemical Society*. Vol. 104, No 1. pp. 56–63. 1957.

Sunder, S., D.W. Shoesmith, and N.H. Miller. "Oxidation and Dissolution of Nuclear Fuel (UO_2) by the Products of the Alpha Radiolysis of Water." *Journal of Nuclear Materials*. Vol. 244. pp. 66–74. 1997a.

Sunder, S., D.W. Shoesmith, M. Kolar, and D.M. Leneveu. "Calculation of Used Nuclear Fuel Dissolution Rates Under Anticipated Canadian Waste Vault Conditions." *Journal of Nuclear Materials*. Vol. 250. pp. 118–130. 1997b.

Swedish National Council for Nuclear Waste. "Nuclear Waste State-of-the-Art Report 2010—Challenges for the Final Repository Programme." Stockholm, Sweden: Swedish National Council for Nuclear Waste. 2010.

Tanaka, Y., S. Uchinashi, Y. Saihara, K. Kikuchi, T. Okaya, and Z. Ogumi. "Dissolution of Hydrogen and the Ratio of the Dissolved Hydrogen Content to the Produced Hydrogen in Electrolyzed Water Using SPE Water Electrolyzer." *Electrochimica Acta.* Vol. 48. pp. 40,13–4,019. 2003.

Thomas, L.E., C.E. Beyer, and L.A. Charlot. "Microstructural Analysis of LWR Spent Fuels at High Burnup." *Journal of Nuclear Materials.* Vol. 188. pp. 80–89. 1992.

Trummer, M. and M. Jonsson. "Resolving the H_2 Effect on Radiation Induced Dissolution of UO_2-Based Spent Nuclear Fuel." *Journal of Nuclear Materials*. Vol. 396. pp. 163–169. 2010.

Trummer, M., O. Roth, and M. Jonsson. "H_2 Inhibition of Radiation Induced Dissolution of Spent Nuclear Fuel." *Journal of Nuclear Materials.* Vol. 383. pp. 226–230. 2009.

Trummer, M., S. Nilsson, and M. Jonsson. "On the Effects of Fission Product Noble Metal Inclusions on the Kinetics of Radiation Induced Dissolution of Spent Nuclear Fuel." *Journal of Nuclear Materials.* Vol. 378. pp. 55–59. 2008.

Young, C. L., ed. *IUPAC Solubility Data Series*. Vol. 5/6, Hydrogen and Deuterium. Pergamon Press. Oxford, England. 1981.

Wilson, C.N. and W.J. Gray. "Measurement of Soluble Nuclide Dissolution Rates from Spent Fuel." Symposium Proceedings Volume 176. Warrendale, Pennsylvania: Materials Research Society. pp. 489–498. 1990.

Wu, L., Z. Qin, and D.W. Shoesmith. "An Improved Model for the Corrosion of Used Nuclear Fuel Inside a Failed Waste Container Under Permanent Disposal Conditions." *Corrosion Science*. Vol. 84. pp. 85–95. 2014.

Wu, L., Y. Beauregard, Z. Qin, S. Rohani, and D.W. Shoesmith. "A Model for the Influence of Steel Corrosion Products on Nuclear Fuel Corrosion Under Permanent Disposal Conditions." *Corrosion Science*. Vol. 61. pp. 83–91. 2012.

APPENDIX A

ELECTROCHEMICAL IMPEDANCE SPECTROSCOPY AND WORKING ELECTRODE POTENTIAL DATA FOR FY 2014 EXPERIMENTS

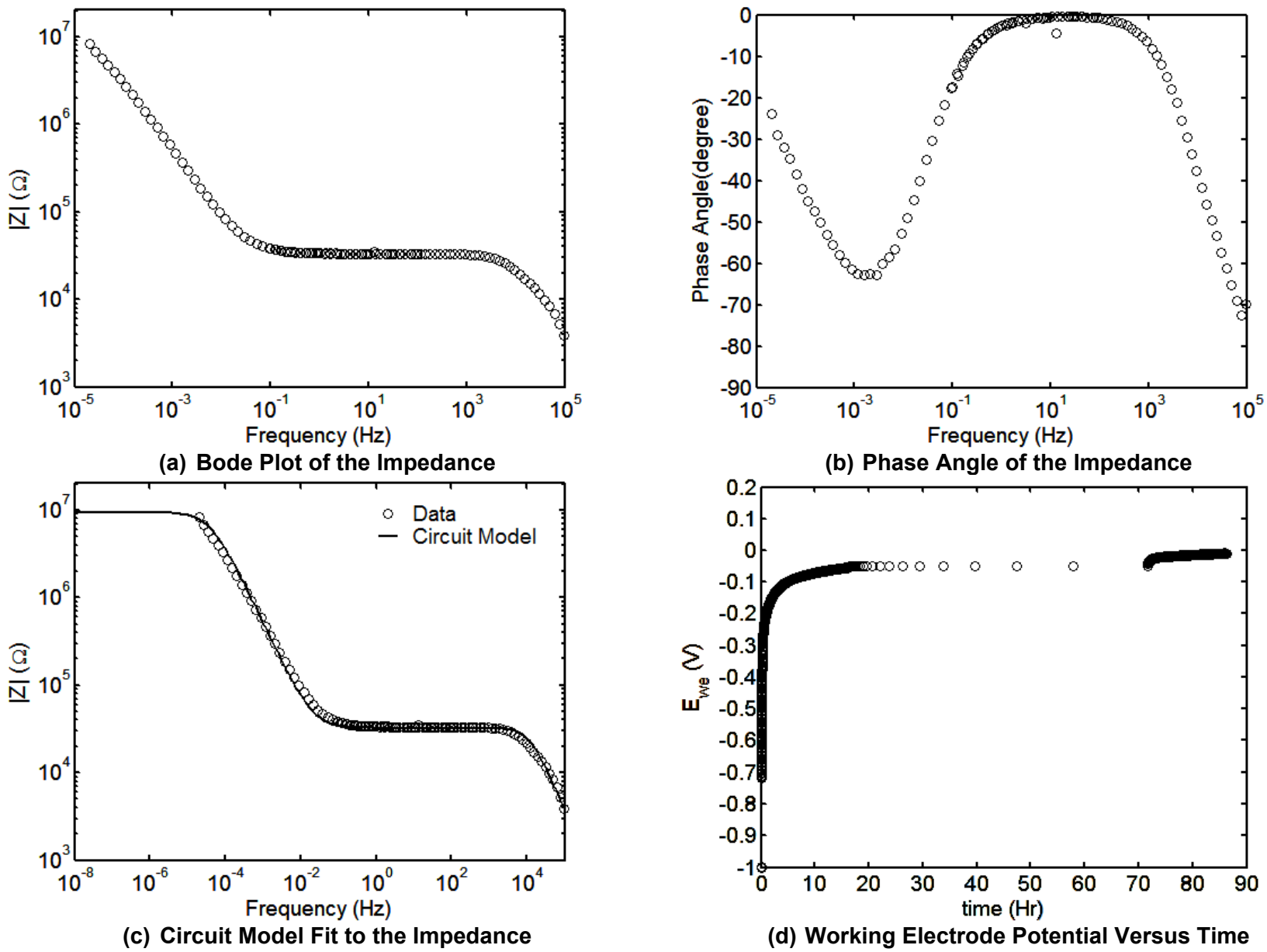

(a) Bode Plot of the Impedance

(b) Phase Angle of the Impedance

(c) Circuit Model Fit to the Impedance

(d) Working Electrode Potential Versus Time

Figure A–1. Electrochemical Impedance Spectroscopy, Circuit Model Fit to the Electrochemical Impedance Spectroscopy, and Working Electrode Potential Versus Time Data for UO_2 SIMFUEL Electrode Under 15 psig Air (Condition 1)

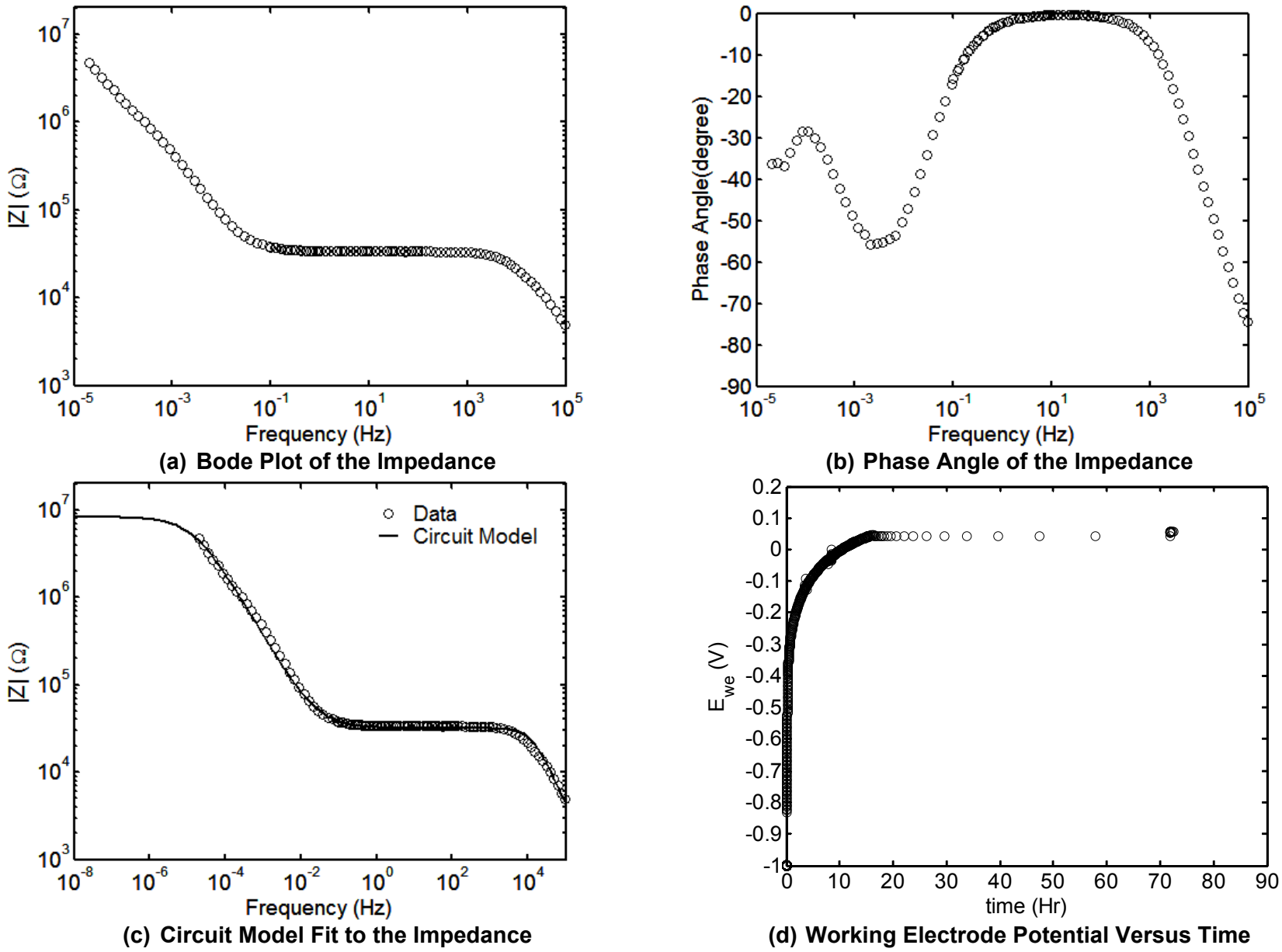

(a) Bode Plot of the Impedance

(b) Phase Angle of the Impedance

(c) Circuit Model Fit to the Impedance

(d) Working Electrode Potential Versus Time

Figure A–2. Electrochemical Impedance Spectroscopy, Circuit Model Fit to the Electrochemical Impedance Spectroscopy, and Working Electrode Potential Versus Time Data for UO_2 SIMFUEL Electrode Under 15 psig Air and 130 psig of 4 Percent H_2 Plus 96 Percent N_2 (Condition 2)

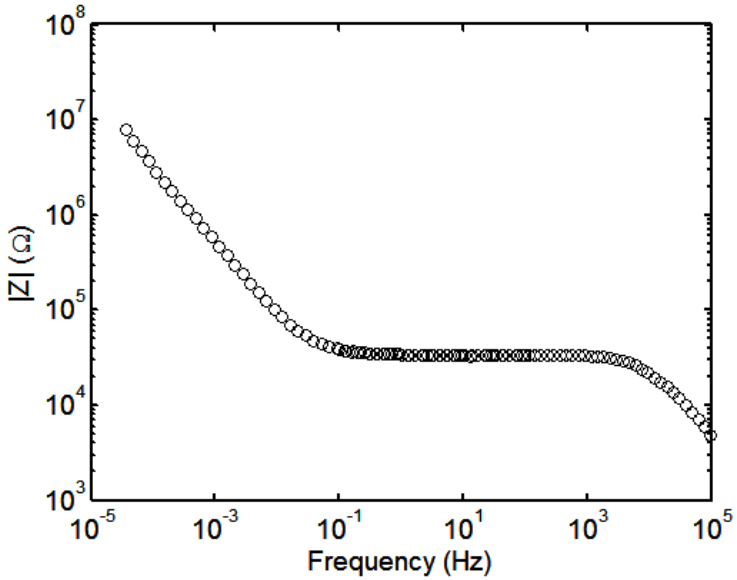

(a) Bode Plot of the Impedance

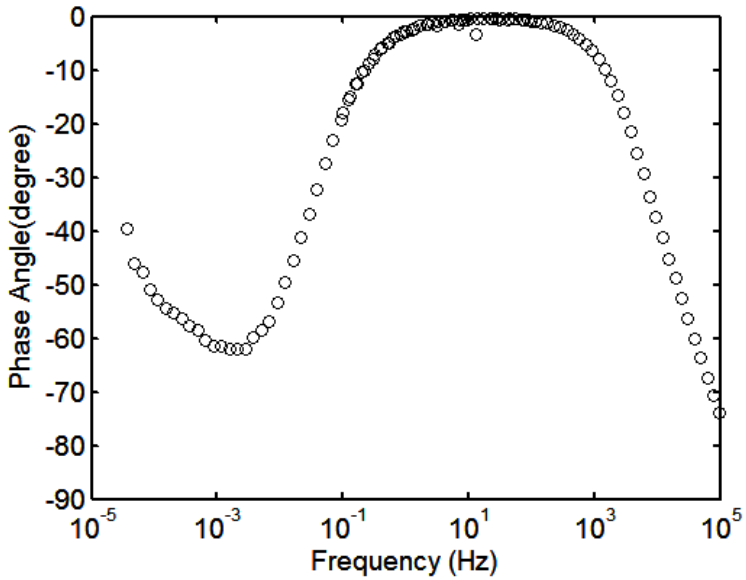

(b) Phase Angle of the Impedance

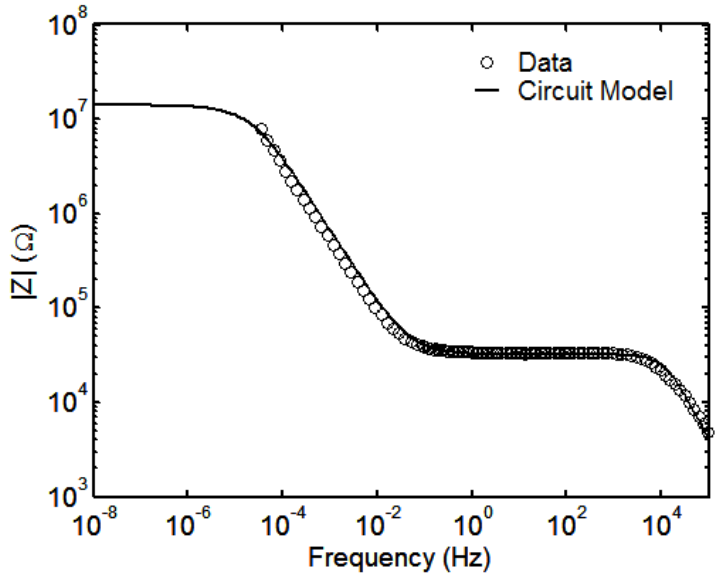

(c) Circuit Model Fit to the Impedance

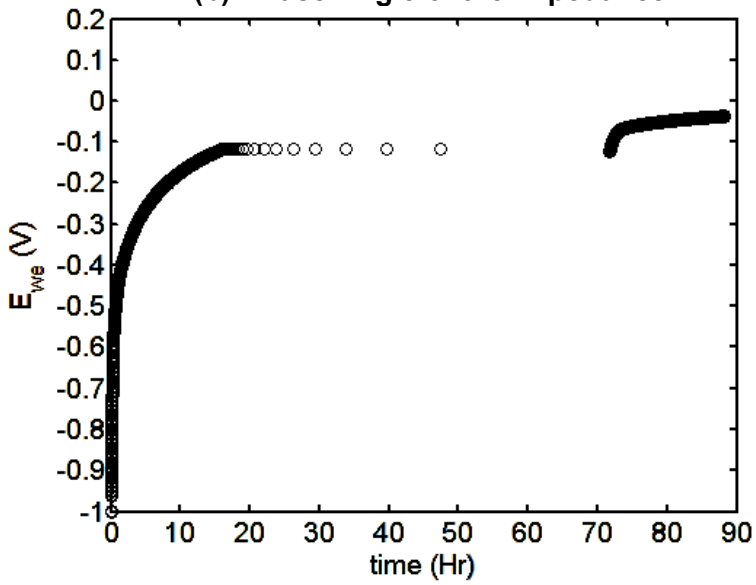

(d) Working Electrode Potential Versus Time

Figure A–3. Electrochemical Impedance Spectroscopy, Circuit Model Fit to the Electrochemical Impedance Spectroscopy, and Working Electrode Potential Versus Time Data for UO_2 SIMFUEL Electrode Under 2 psig Air and 15 psig of 4 Percent H_2 Plus 96 Percent N_2 (Condition 3)

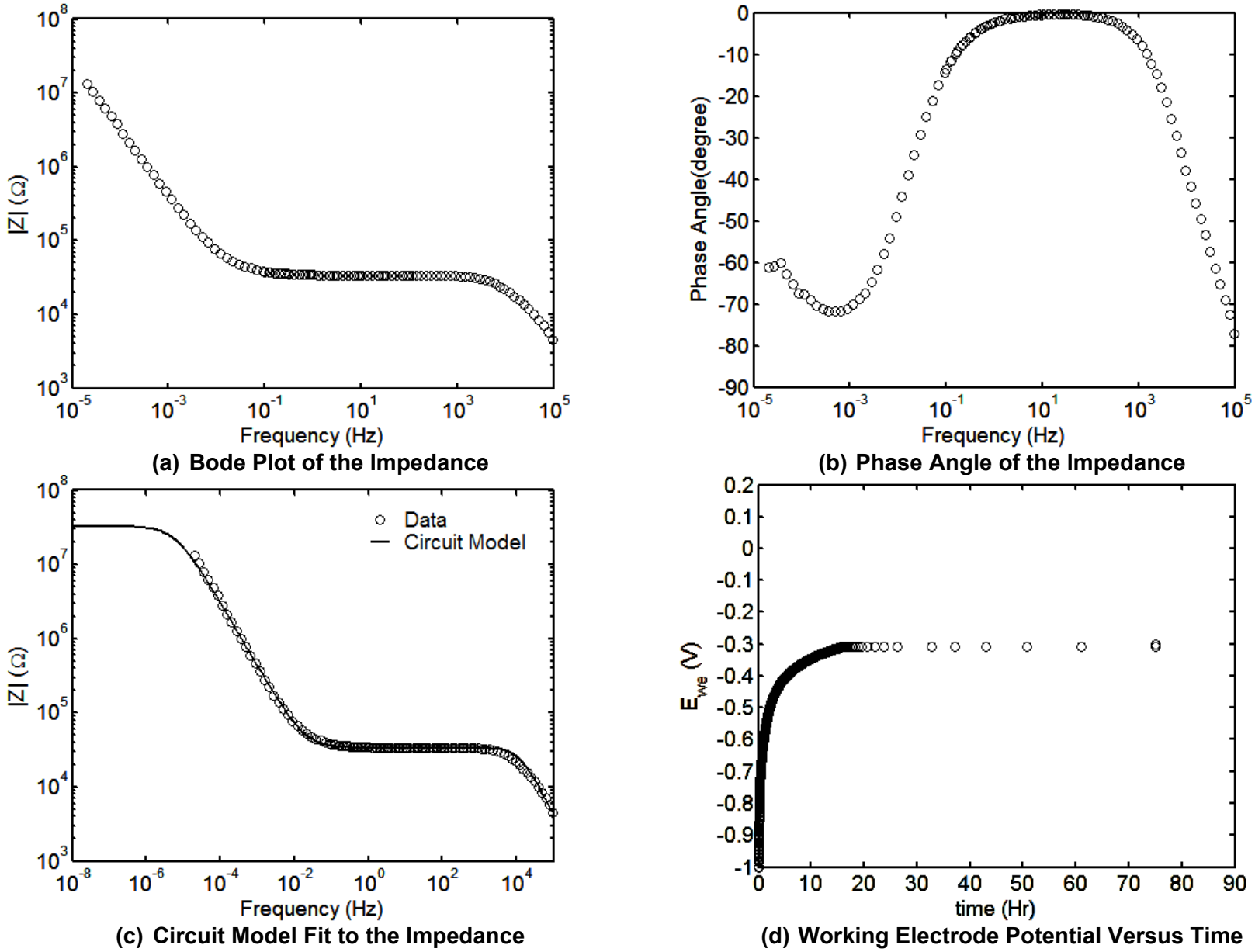

(a) Bode Plot of the Impedance

(b) Phase Angle of the Impedance

(c) Circuit Model Fit to the Impedance

(d) Working Electrode Potential Versus Time

Figure A–4. Electrochemical Impedance Spectroscopy, Circuit Model Fit to the Electrochemical Impedance Spectroscopy, and Working Electrode Potential Versus Time Data for UO_2 SIMFUEL Electrode Under 130 psig of 4 Percent H_2 Plus 96 Percent N_2 (Condition 4)

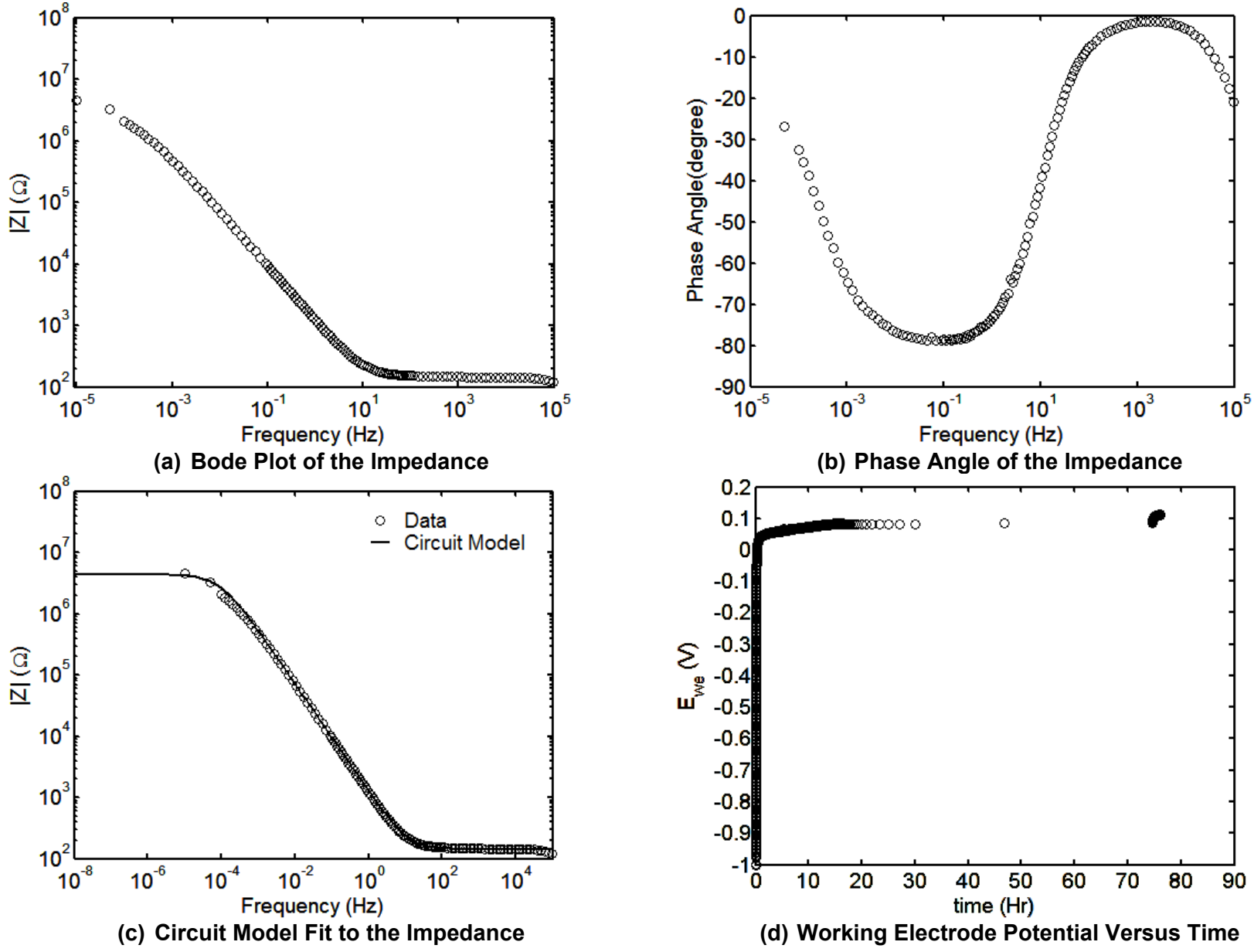

(a) Bode Plot of the Impedance

(b) Phase Angle of the Impedance

(c) Circuit Model Fit to the Impedance

(d) Working Electrode Potential Versus Time

Figure A–5. Electrochemical Impedance Spectroscopy, Circuit Model Fit to the Electrochemical Impedance Spectroscopy, and Working Electrode Potential Versus Time Data for 35 GW-day/MTU Burnup Equivalent SIMFUEL Electrode Under 15 psig Air (Condition 1)

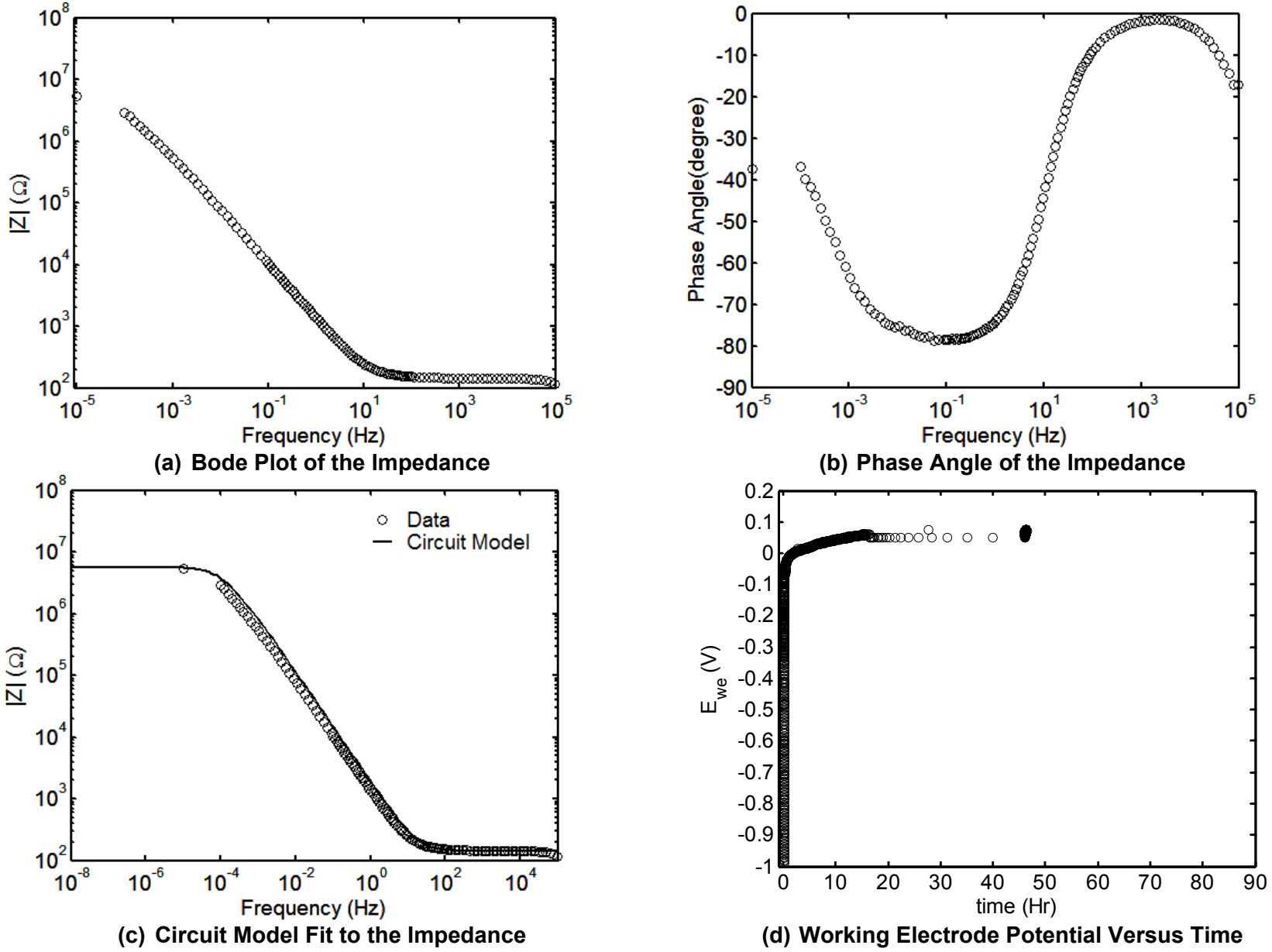

(a) Bode Plot of the Impedance

(b) Phase Angle of the Impedance

(c) Circuit Model Fit to the Impedance

(d) Working Electrode Potential Versus Time

Figure A–6. Electrochemical Impedance Spectroscopy, Circuit Model Fit to the Electrochemical Impedance Spectroscopy, and Working Electrode Potential Versus Time Data for 35 GW-day/MTU Burnup Equivalent SIMFUEL Electrode Under 15 psig Air and 130 psig of 4 Percent H_2 Plus 96 Percent N_2 (Condition 2)

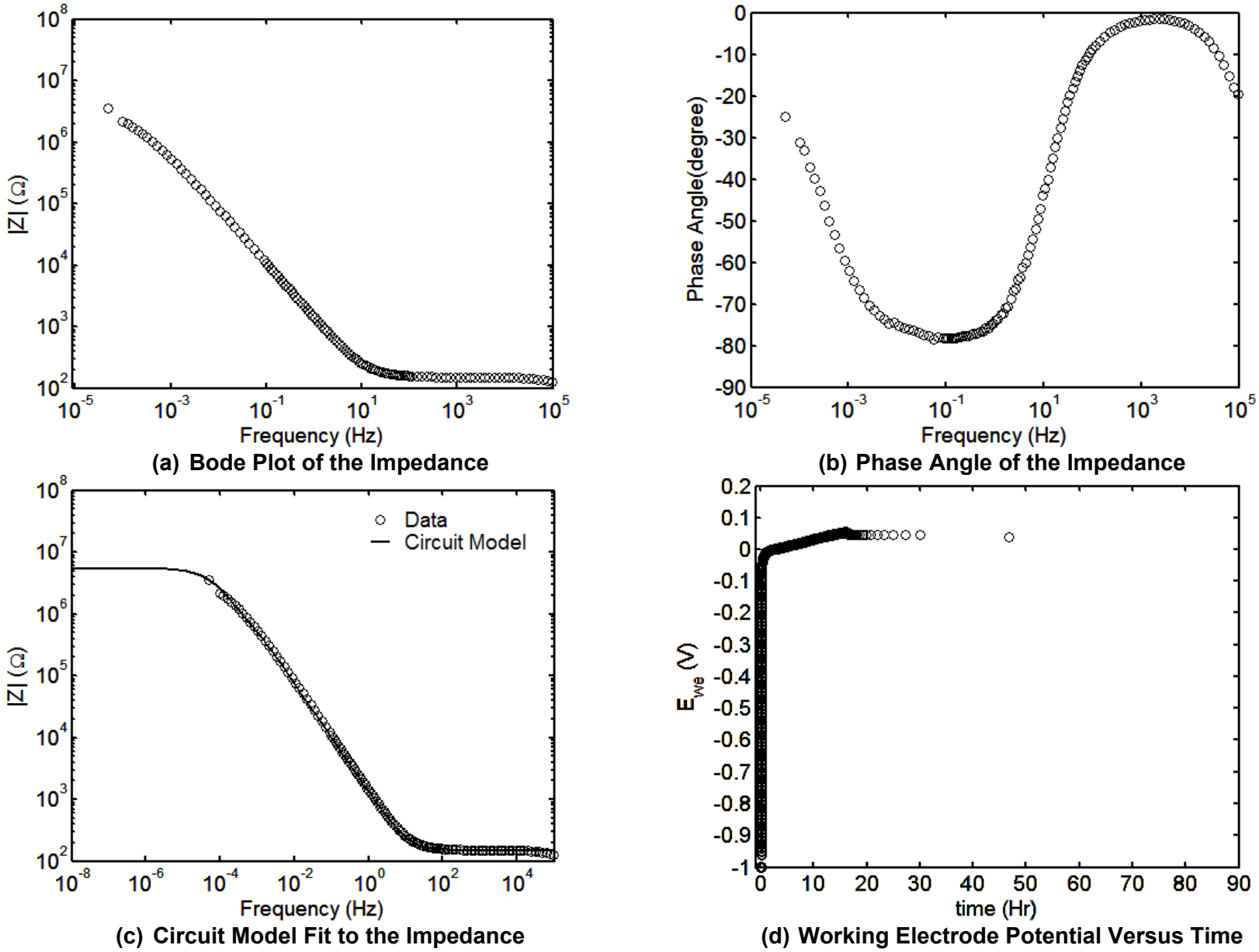

(a) Bode Plot of the Impedance

(b) Phase Angle of the Impedance

(c) Circuit Model Fit to the Impedance

(d) Working Electrode Potential Versus Time

Figure A–7. Electrochemical Impedance Spectroscopy, Circuit Model Fit to the Electrochemical Impedance Spectroscopy, and Working Electrode Potential Versus Time Data for 35 GW-day/MTU Burnup Equivalent SIMFUEL Electrode Under 2 psig Air and 15 psig of 4 Percent H_2 Plus 96 Percent N_2 (Condition 3)

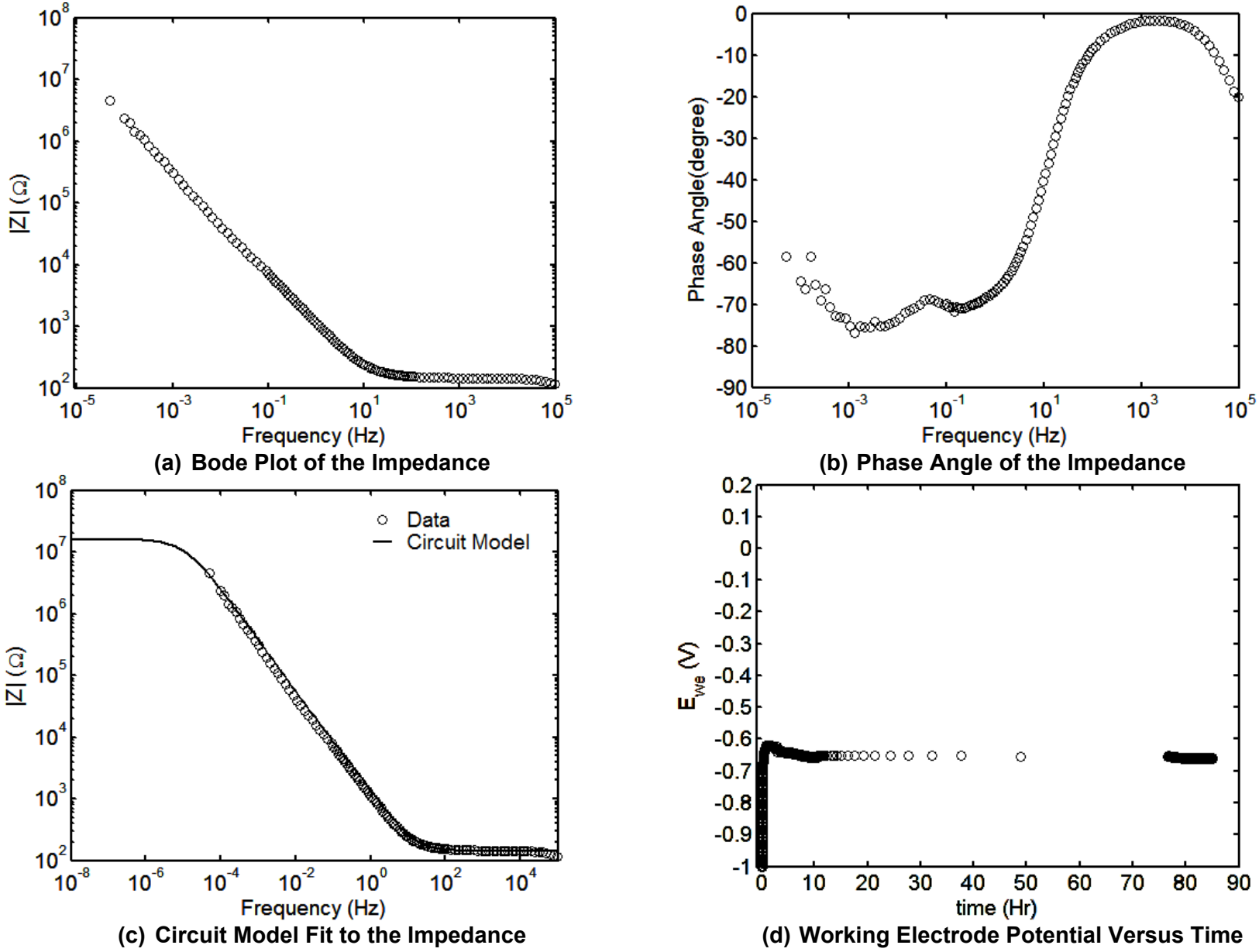

Figure A–8. Electrochemical Impedance Spectroscopy, Circuit Model Fit to the Electrochemical Impedance Spectroscopy, and Working Electrode Potential Versus Time Data for 35 GW-day/MTU Burnup Equivalent SIMFUEL Electrode 130 psig of 4 Percent H_2 Plus 96 Percent N_2 (Condition 4)

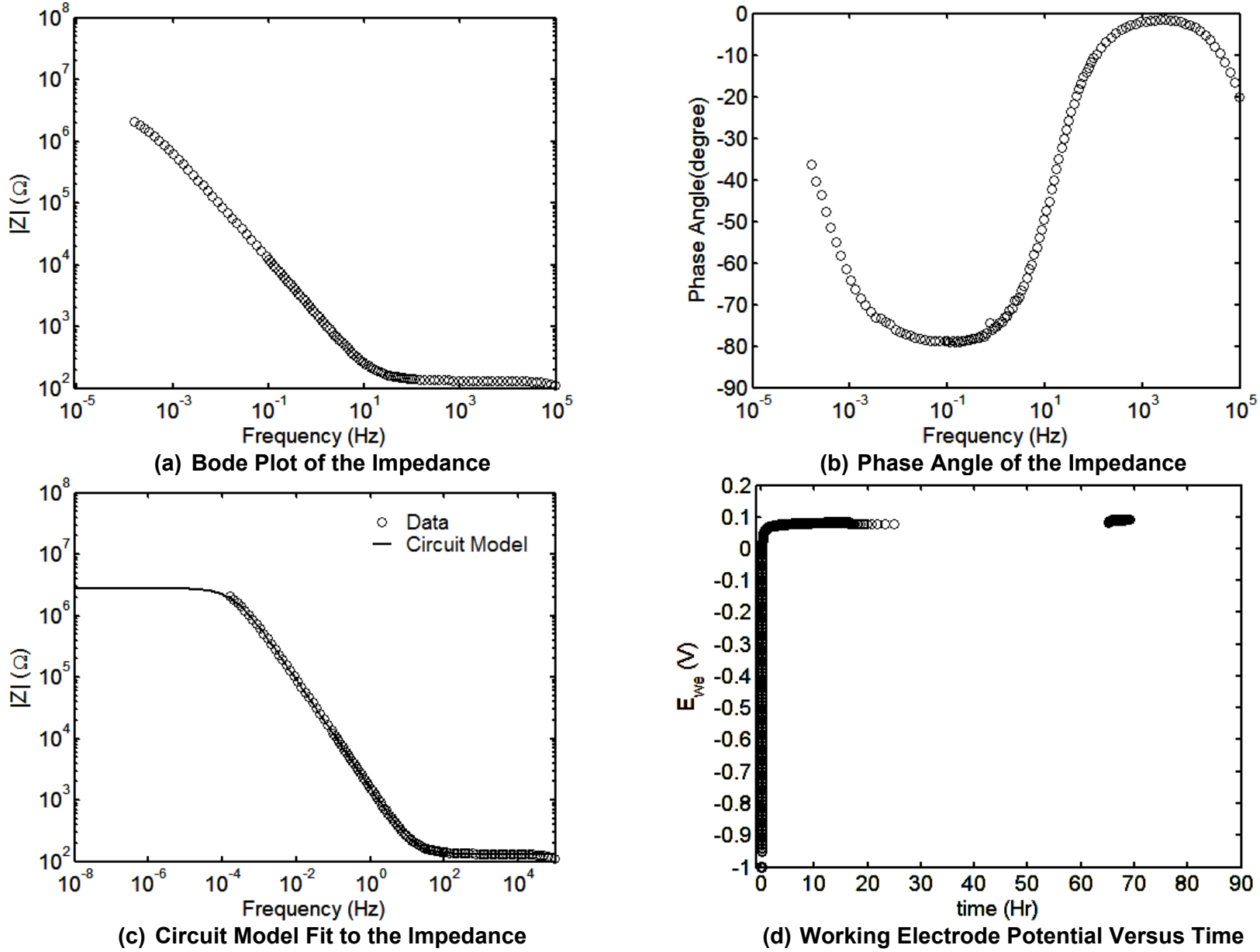

(a) Bode Plot of the Impedance

(b) Phase Angle of the Impedance

(c) Circuit Model Fit to the Impedance

(d) Working Electrode Potential Versus Time

Figure A–9. Electrochemical Impedance Spectroscopy, Circuit Model Fit to the Electrochemical Impedance Spectroscopy, and Working Electrode Potential Versus Time Data for 60 GW-day/MTU Burnup Equivalent SIMFUEL Electrode Under 15 psig Air (Condition 1)

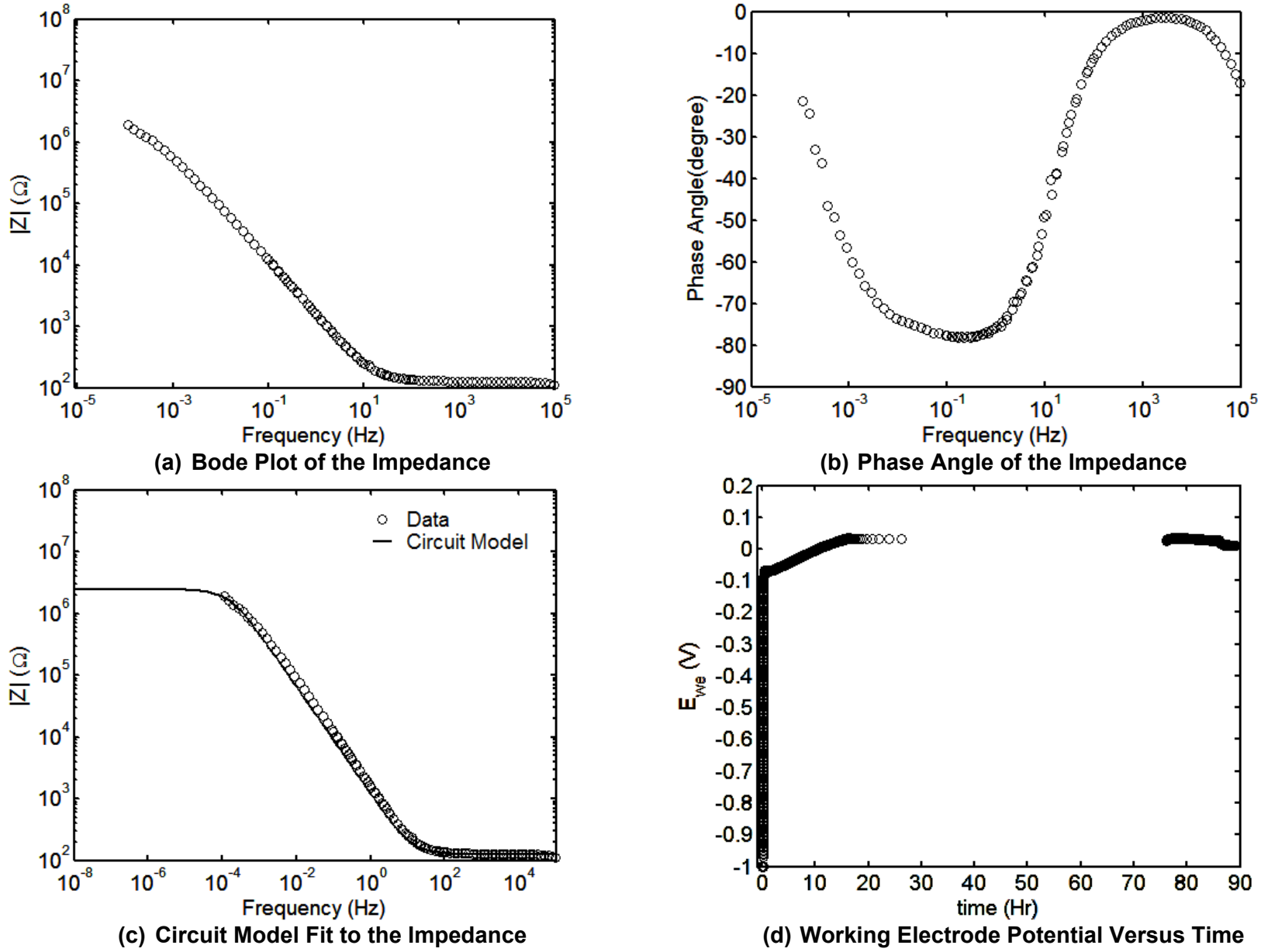

(a) Bode Plot of the Impedance

(b) Phase Angle of the Impedance

(c) Circuit Model Fit to the Impedance

(d) Working Electrode Potential Versus Time

Figure A–10. Electrochemical Impedance Spectroscopy, Circuit Model Fit to the Electrochemical Impedance Spectroscopy, and Working Electrode Potential Versus Time Data for 60 GW-day/MTU Burnup Equivalent SIMFUEL Electrode Under 15 psig Air and 130 psig of 4 Percent H_2 Plus 96 Percent N_2 (Condition 2)

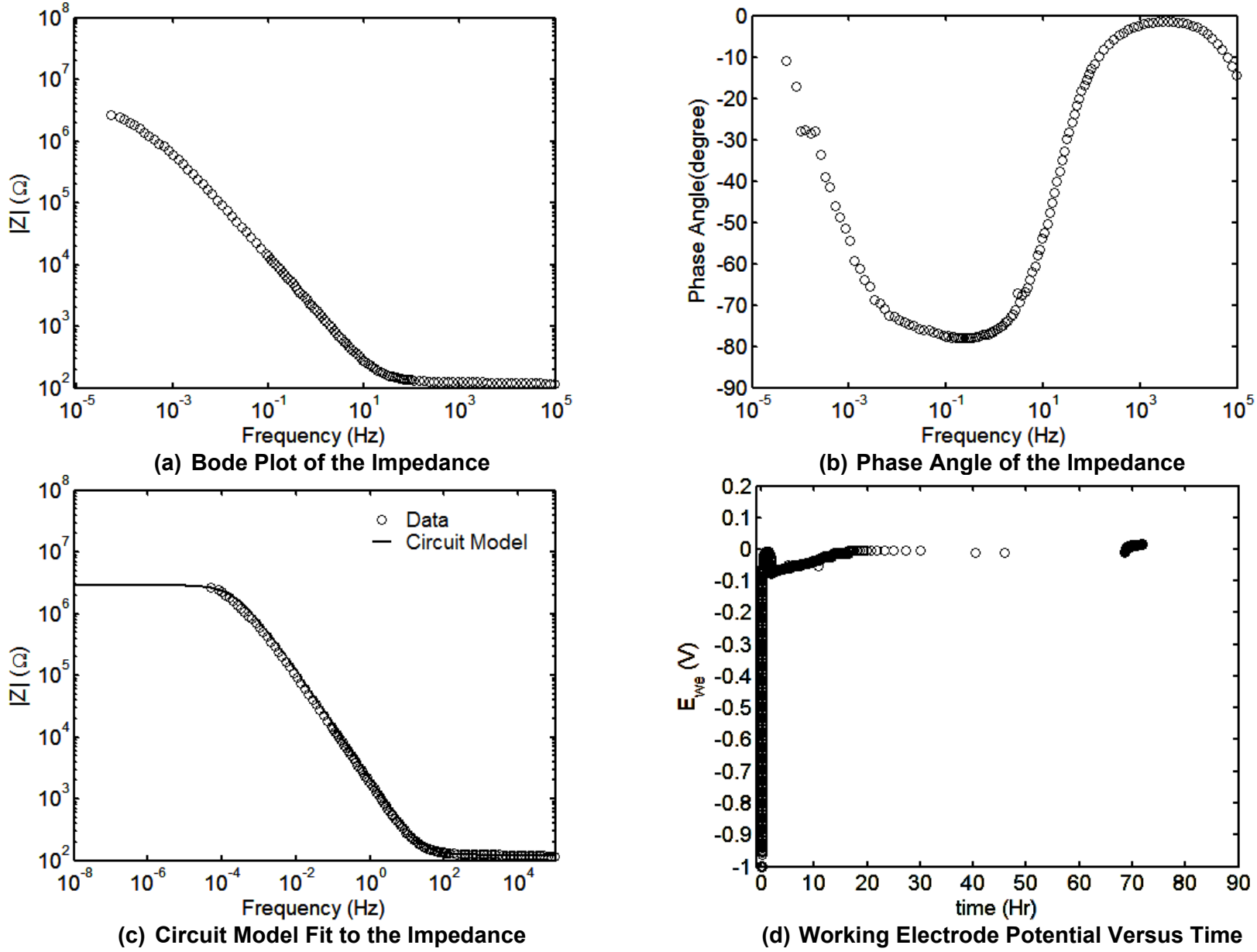

(a) Bode Plot of the Impedance

(b) Phase Angle of the Impedance

(c) Circuit Model Fit to the Impedance

(d) Working Electrode Potential Versus Time

Figure A–11. Electrochemical Impedance Spectroscopy, Circuit Model Fit to the Electrochemical Impedance Spectroscopy, and Working Electrode Potential Versus Time Data for 60 GW-day/MTU Burnup Equivalent SIMFUEL Electrode Under 2 psig Air and 15 psig of 4 Percent H_2 Plus 96 Percent N_2 (Condition 3)

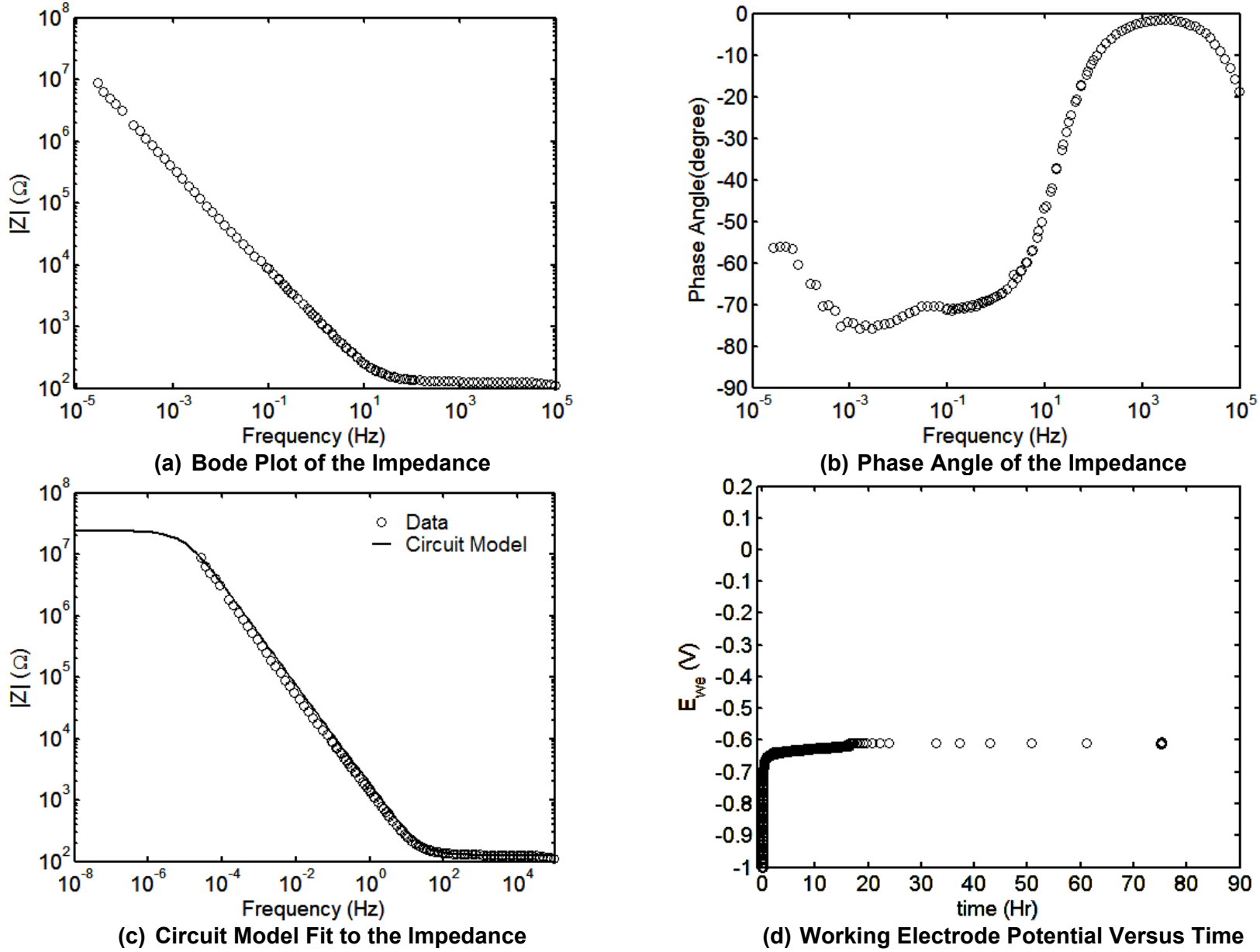

(a) Bode Plot of the Impedance

(b) Phase Angle of the Impedance

(c) Circuit Model Fit to the Impedance

(d) Working Electrode Potential Versus Time

Figure A–12. Electrochemical Impedance Spectroscopy, Circuit Model Fit to the Electrochemical Impedance Spectroscopy, and Working Electrode Potential Versus Time Data for 60 GW-day/MTU Burnup Equivalent SIMFUEL Electrode Under 130 psig of 4 Percent H_2 Plus 96 Percent N_2 (Condition 4)

APPENDIX B

ELECTROCHEMICAL IMPEDANCE SPECTROSCOPY AND WORKING ELECTRODE POTENTIAL DATA FOR FY 2015 EXPERIMENTS

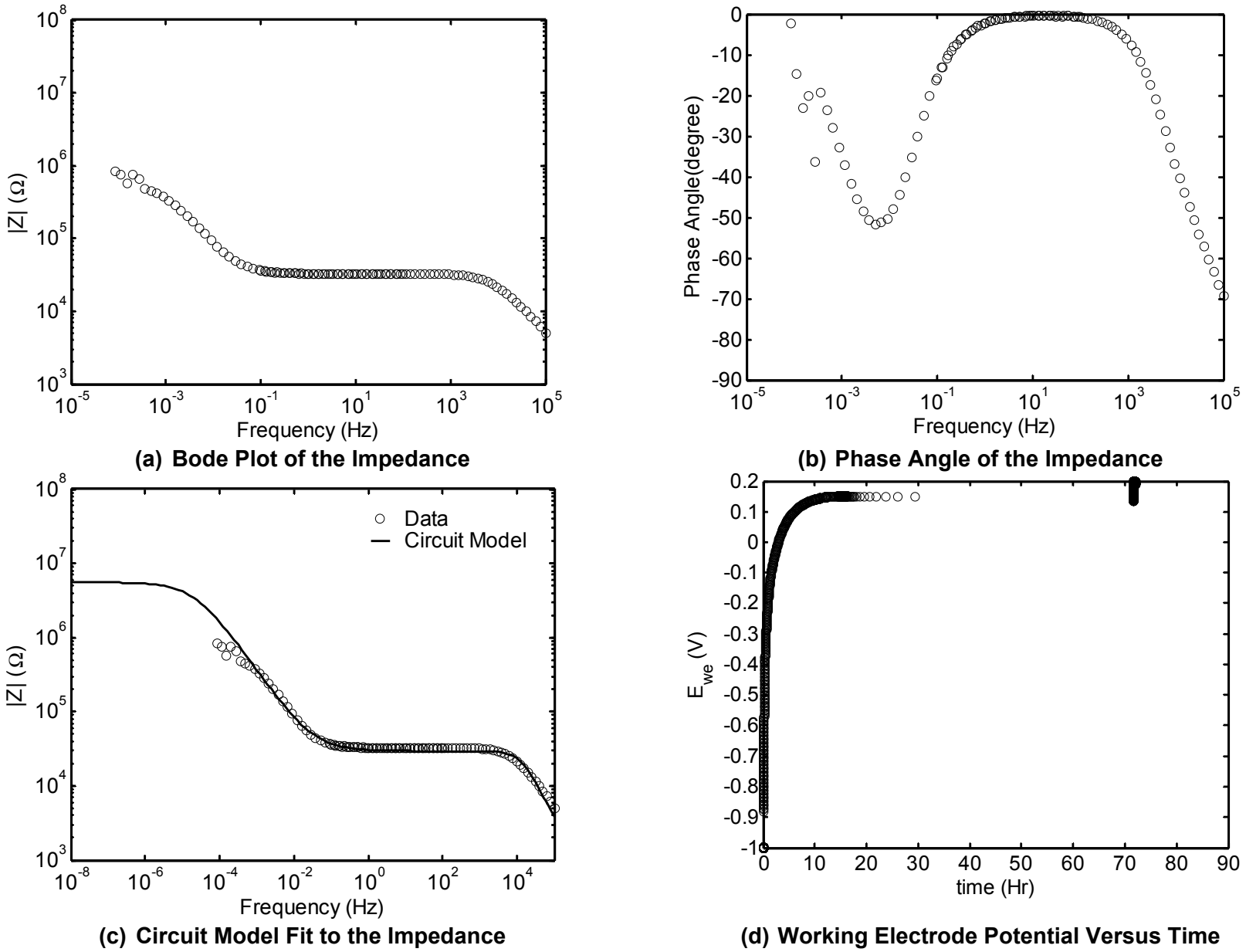

Figure B–1. Electrochemical Impedance Spectroscopy, Circuit Model Fit to the Electrochemical Impedance Spectroscopy, and Working Electrode Potential Versus Time Data for UO_2 SIMFUEL Electrode Under 5 psig Air and 130 psig of 4 Percent H_2 Plus 96 Percent N_2 (Condition 2)

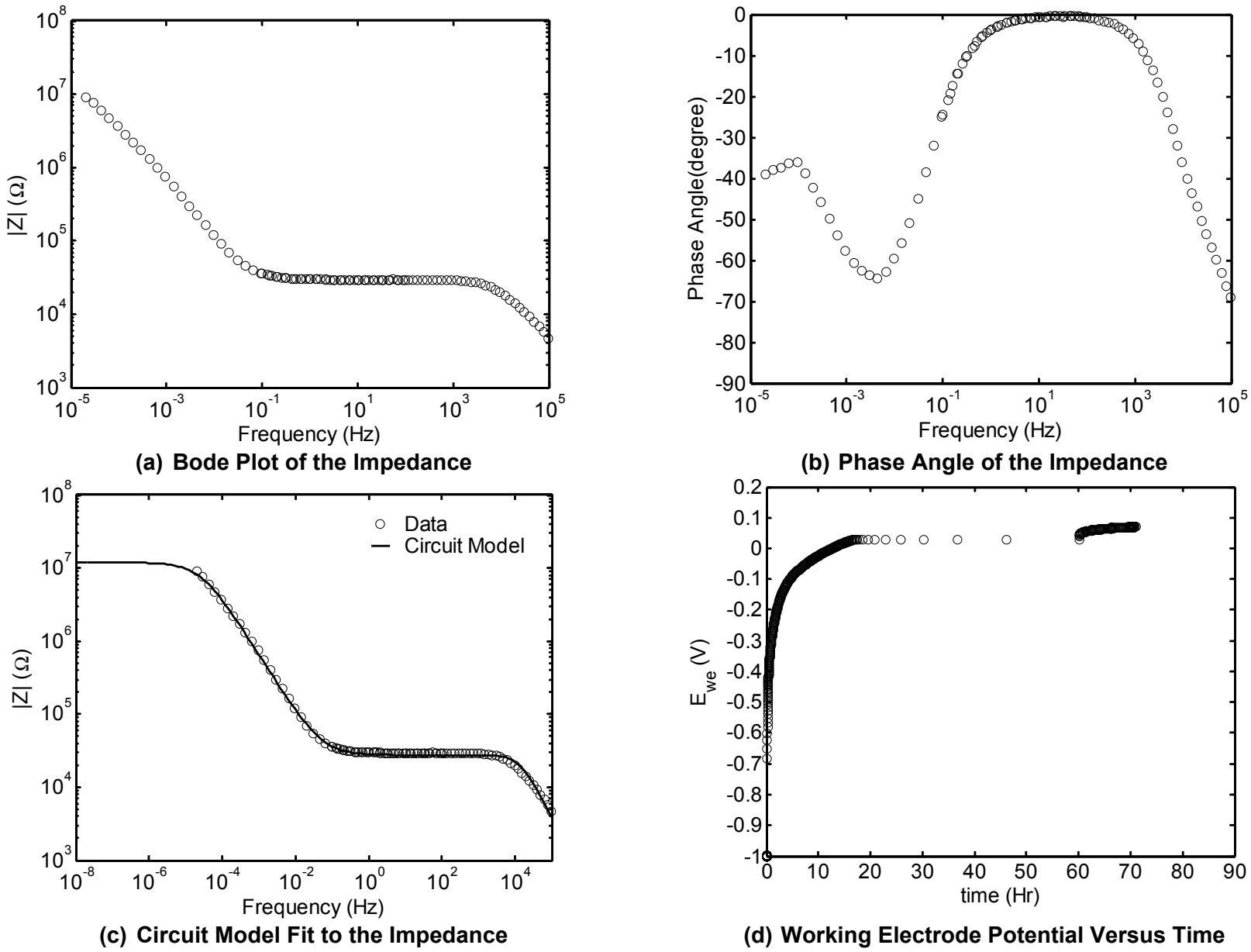

(a) Bode Plot of the Impedance

(b) Phase Angle of the Impedance

(c) Circuit Model Fit to the Impedance

(d) Working Electrode Potential Versus Time

Figure B–2. Electrochemical Impedance Spectroscopy, Circuit Model Fit to the Electrochemical Impedance Spectroscopy, and Working Electrode Potential Versus Time Data for UO_2 SIMFUEL Electrode Under 10 psig Air and 15 psig of 4 Percent H_2 Plus 96 Percent N_2 (Condition 3, Run 1)

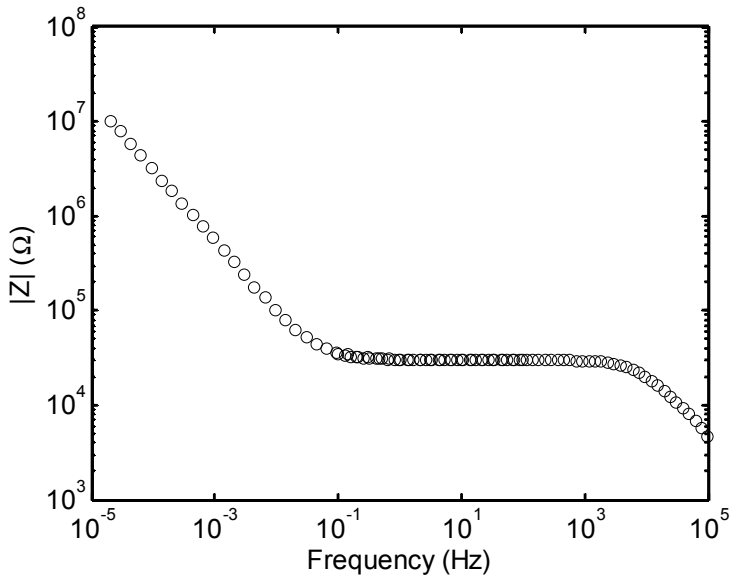

(a) Bode Plot of the Impedance

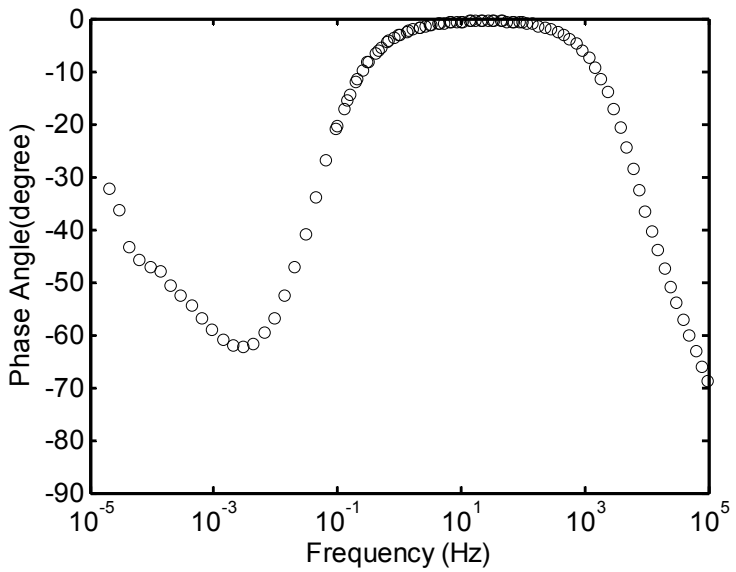

(b) Phase Angle of the Impedance

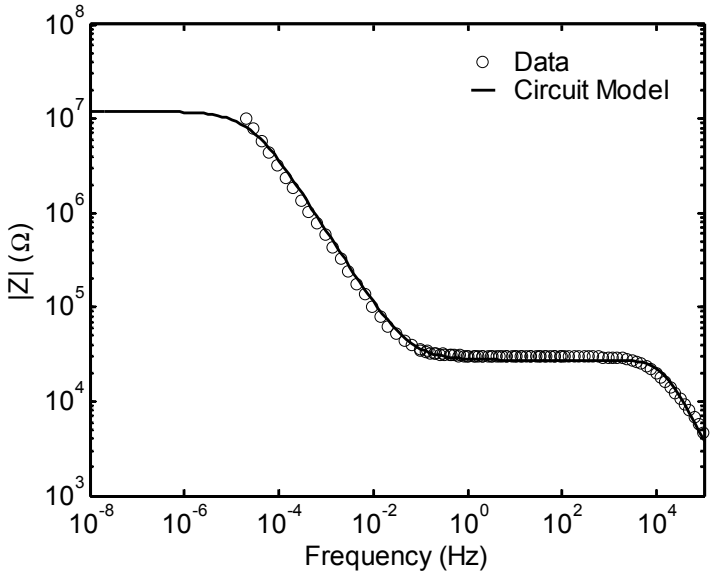

(c) Circuit Model Fit to the Impedance

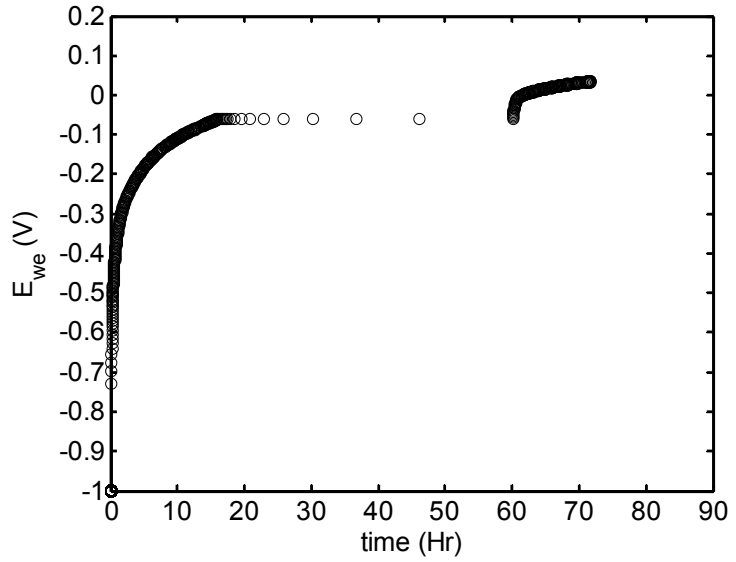

(d) Working Electrode Potential Versus Time

Figure B–3. Electrochemical Impedance Spectroscopy, Circuit Model Fit to the Electrochemical Impedance Spectroscopy, and Working Electrode Potential Versus Time Data for UO_2 SIMFUEL Electrode Under 10 psig Air and 15 psig of 4 Percent H_2 Plus 96 Percent N_2 (Condition 3, Run 2)

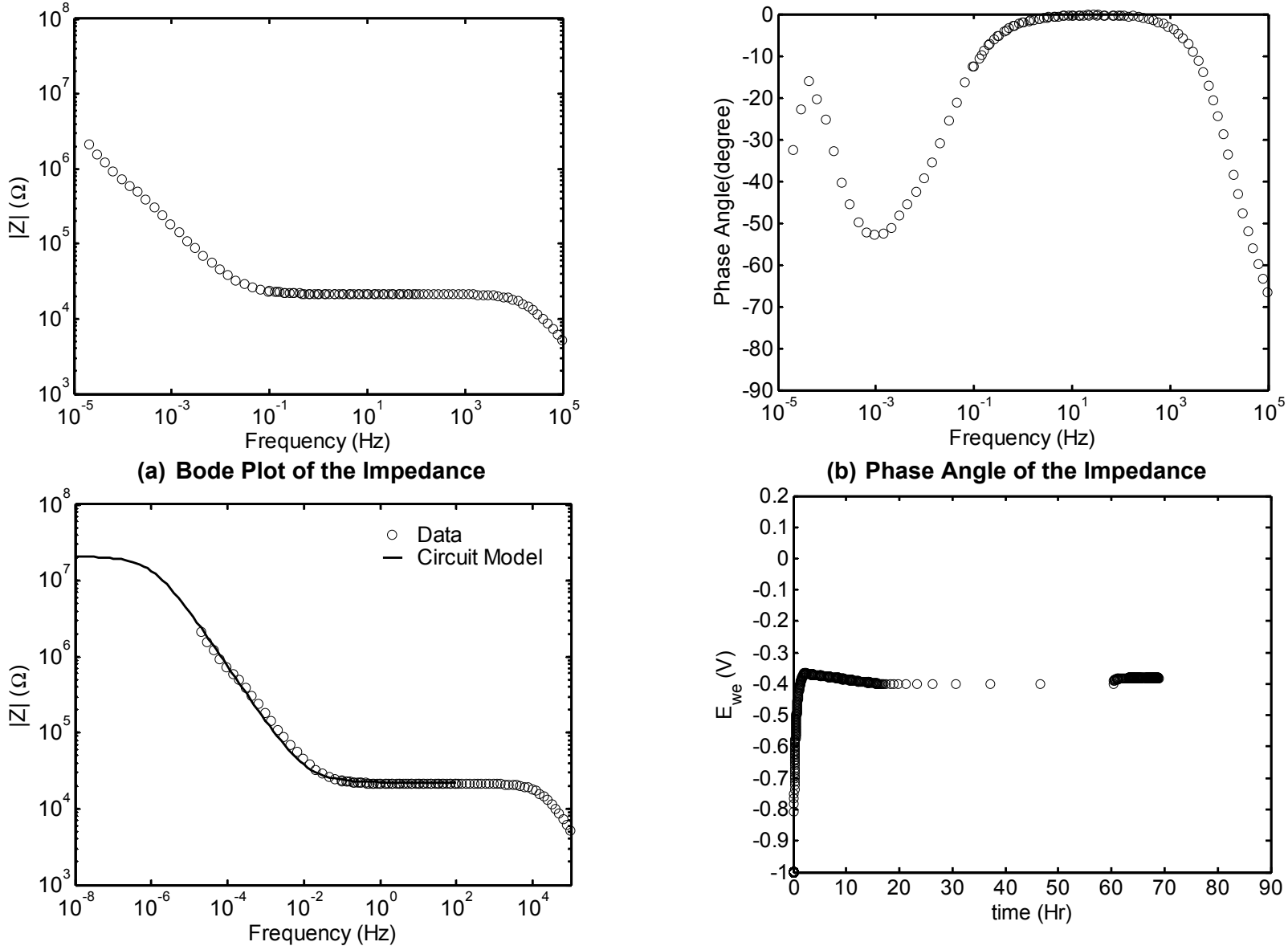

(a) Bode Plot of the Impedance

(b) Phase Angle of the Impedance

(c) Circuit Model Fit to the Impedance

(d) Working Electrode Potential Versus Time

Figure B–4. Electrochemical Impedance Spectroscopy, Circuit Model Fit to the Electrochemical Impedance Spectroscopy, and Working Electrode Potential Versus Time Data for UO_2 SIMFUEL Electrode Under 130 psig of 4 Percent H_2 Plus 96 Percent N_2 (Condition 4, Run 1)

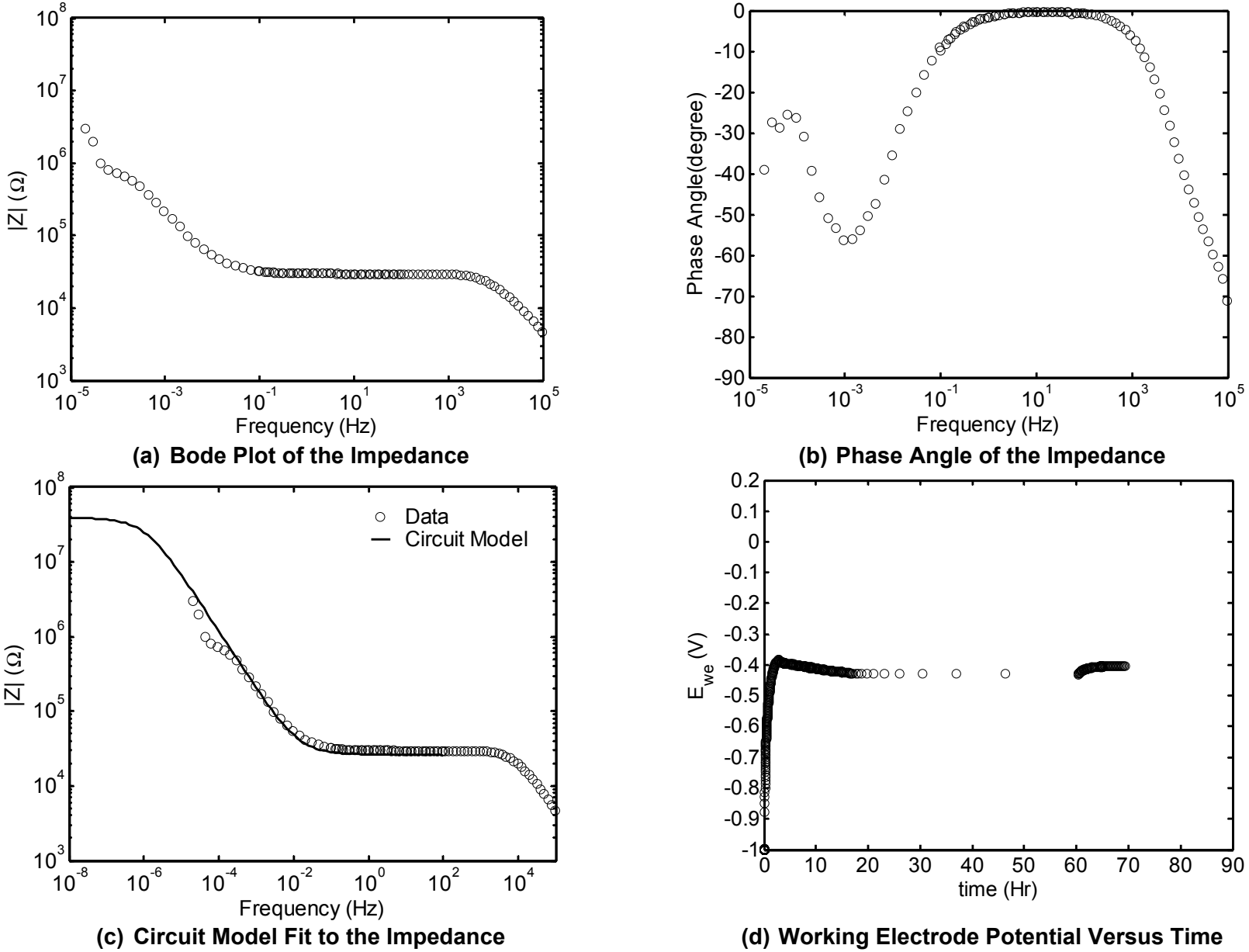

(a) Bode Plot of the Impedance

(b) Phase Angle of the Impedance

(c) Circuit Model Fit to the Impedance

(d) Working Electrode Potential Versus Time

Figure B–5. Electrochemical Impedance Spectroscopy, Circuit Model Fit to the Electrochemical Impedance Spectroscopy, and Working Electrode Potential Versus Time Data for UO_2 SIMFUEL Electrode Under 130 psig of 4 Percent H_2 Plus 96 Percent N_2 (Condition 4, Run 2)

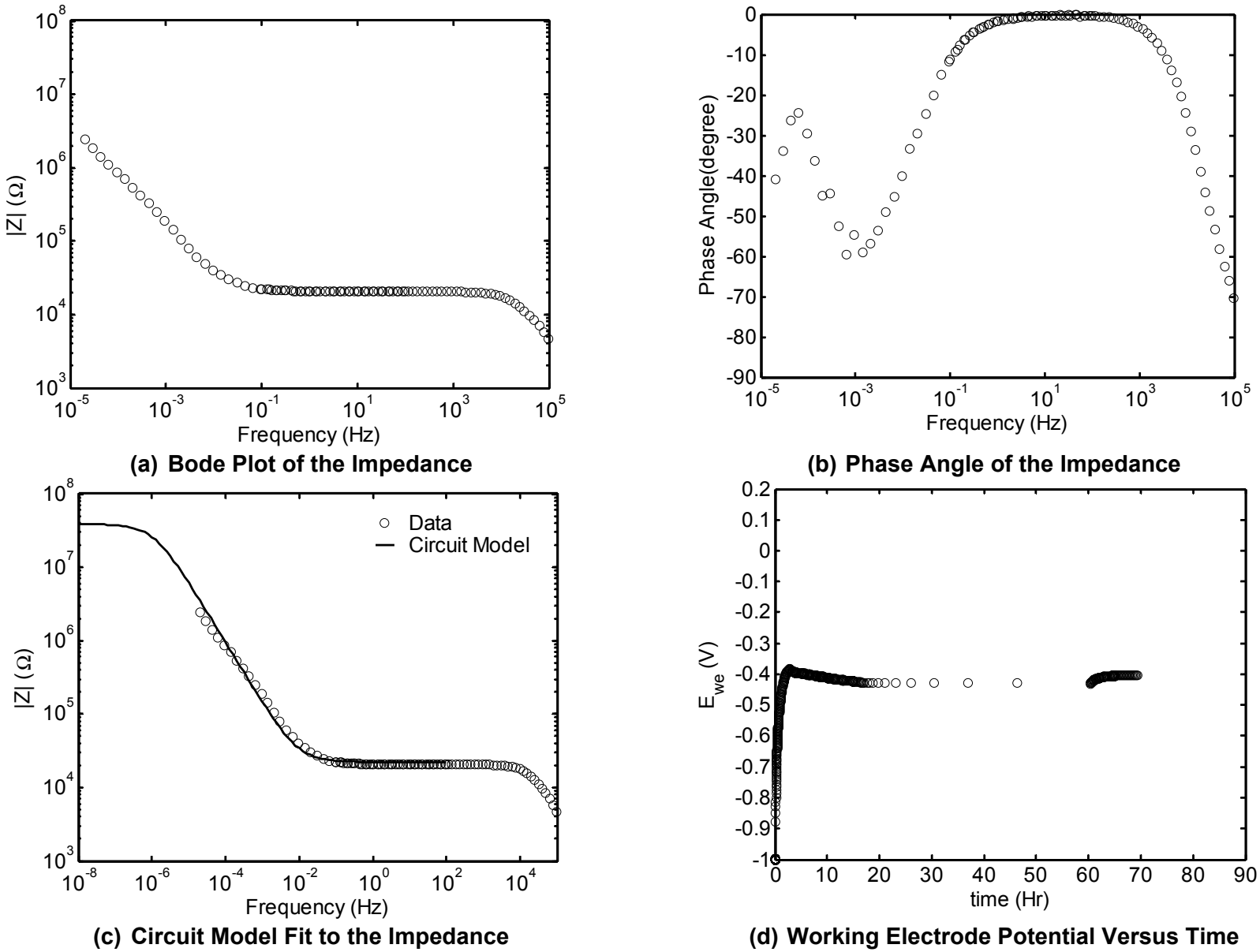

(a) Bode Plot of the Impedance

(b) Phase Angle of the Impedance

(c) Circuit Model Fit to the Impedance

(d) Working Electrode Potential Versus Time

Figure B–6. Electrochemical Impedance Spectroscopy, Circuit Model Fit to the Electrochemical Impedance Spectroscopy, and Working Electrode Potential Versus Time Data for UO_2 SIMFUEL Electrode Under 130 psig of 4 Percent H_2 Plus 96 Percent N_2 (Condition 4, Run 3)

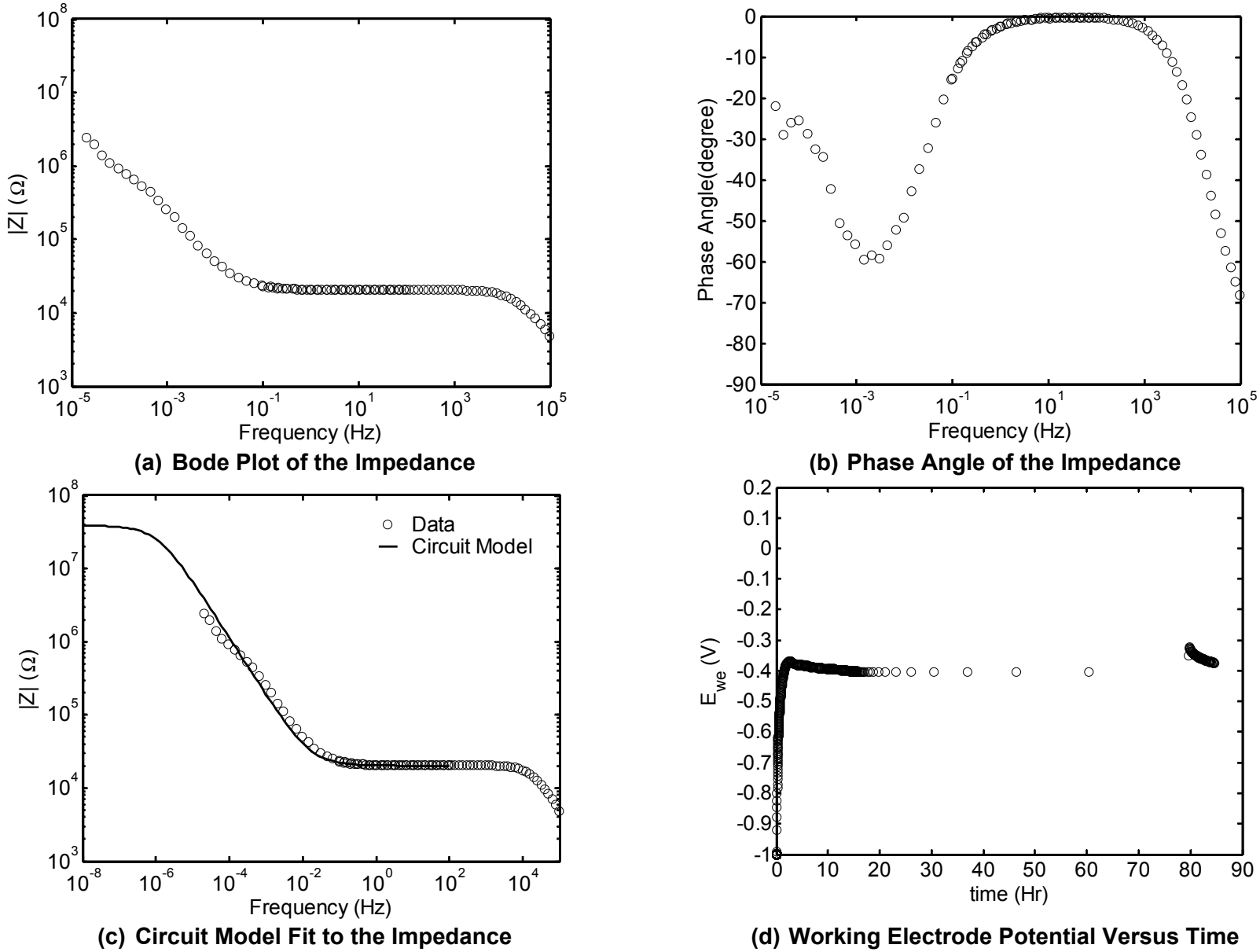

(a) Bode Plot of the Impedance

(b) Phase Angle of the Impedance

(c) Circuit Model Fit to the Impedance

(d) Working Electrode Potential Versus Time

Figure B–7. Electrochemical Impedance Spectroscopy, Circuit Model Fit to the Electrochemical Impedance Spectroscopy, and Working Electrode Potential Versus Time Data for UO_2 SIMFUEL Electrode Under 130 psig of 4 Percent H_2 Plus 96 Percent N_2 (Condition 4, Run 4)

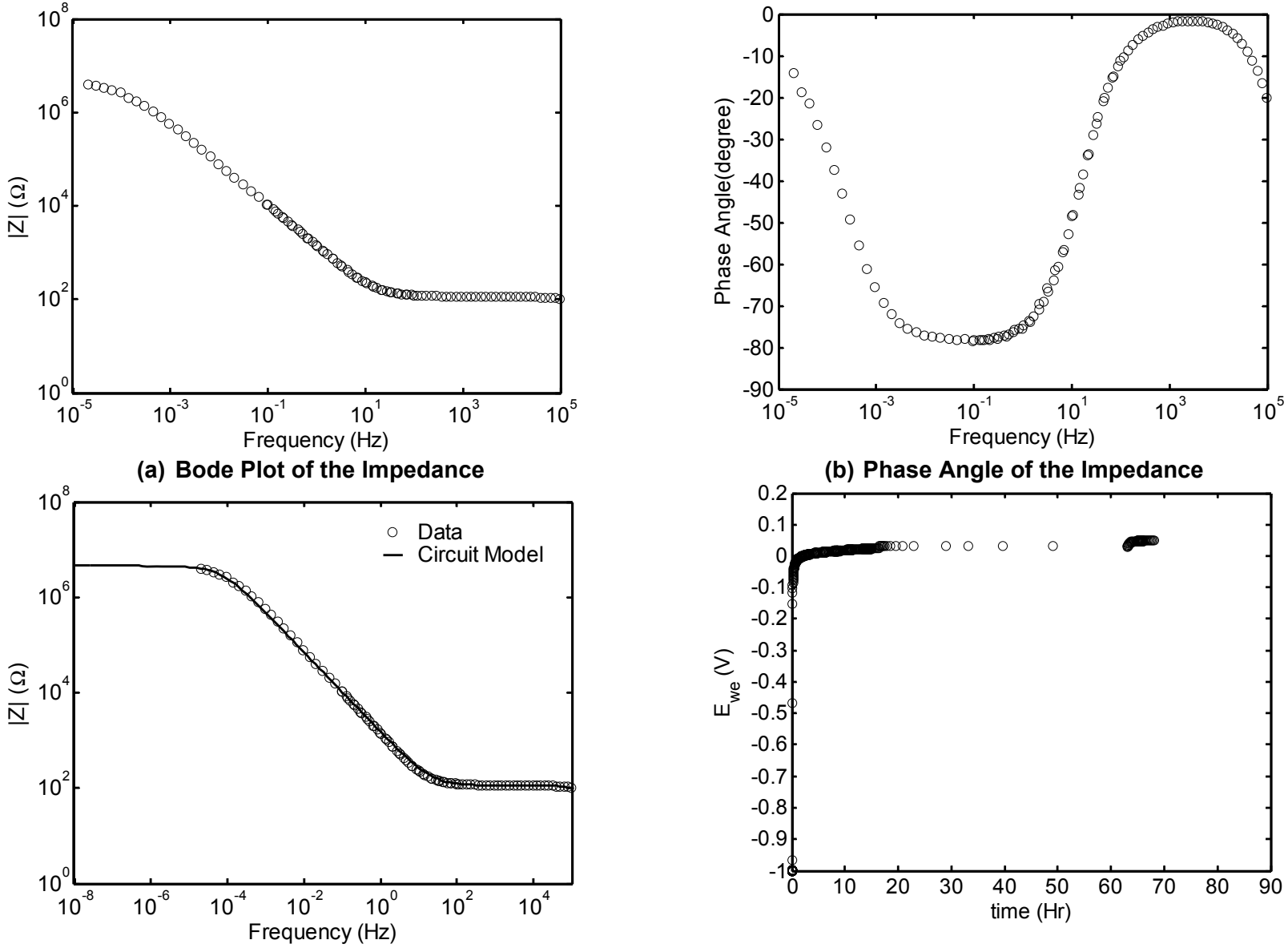

(a) Bode Plot of the Impedance

(b) Phase Angle of the Impedance

(c) Circuit Model Fit to the Impedance

(d) Working Electrode Potential Versus Time

Figure B–8. Electrochemical Impedance Spectroscopy, Circuit Model Fit to the Electrochemical Impedance Spectroscopy, and Working Electrode Potential Versus Time Data for 35 GW-day/MTU Burnup Equivalent SIMFUEL Electrode Under 15 psig of Air (Condition 1)

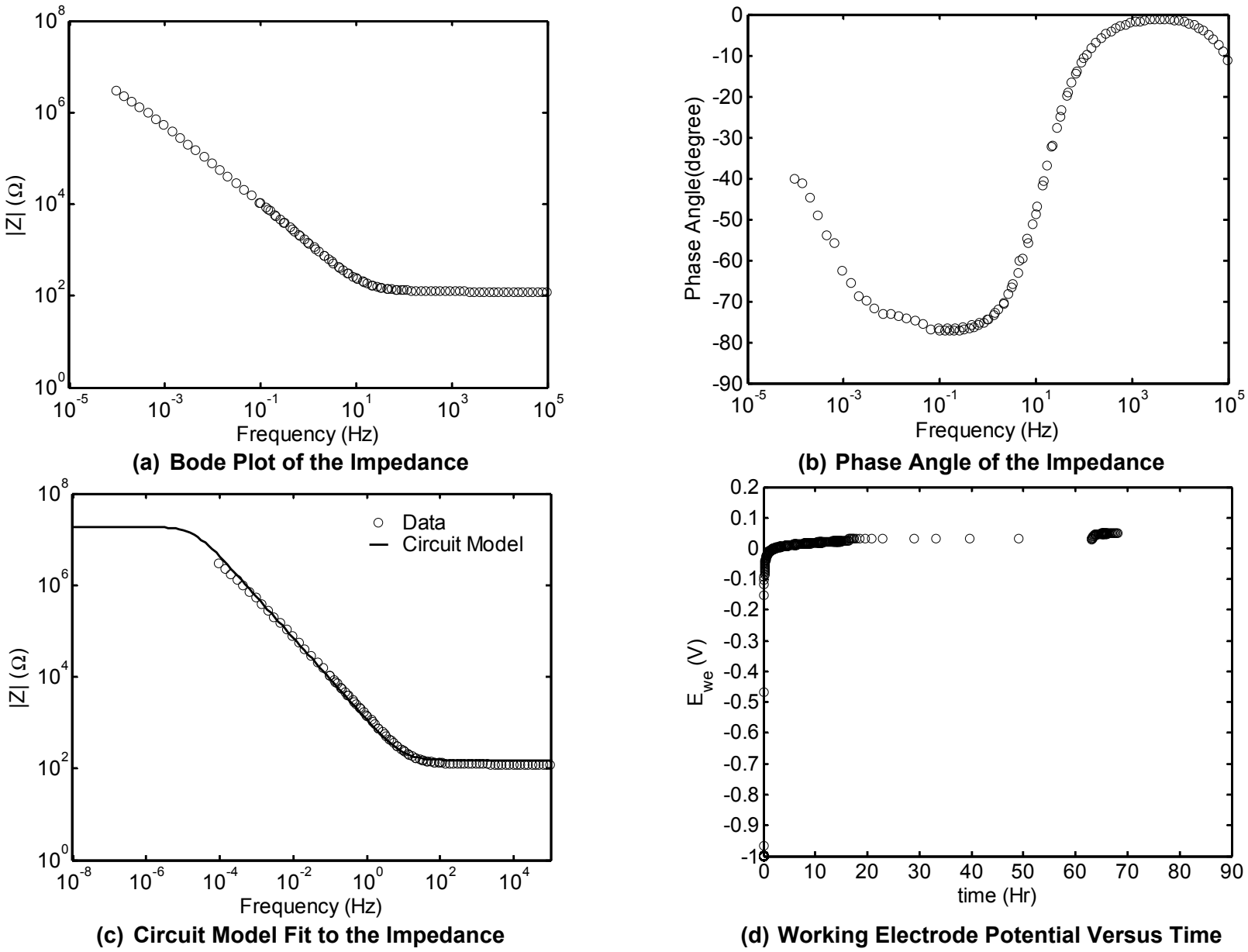

(a) Bode Plot of the Impedance

(b) Phase Angle of the Impedance

(c) Circuit Model Fit to the Impedance

(d) Working Electrode Potential Versus Time

Figure B–9. Electrochemical Impedance Spectroscopy, Circuit Model Fit to the Electrochemical Impedance Spectroscopy, and Working Electrode Potential Versus Time Data for 35 GW-day/MTU Burnup Equivalent SIMFUEL Electrode Under 10 psig Air and 15 psig of 4 Percent H_2 Plus 96 Percent N_2 (Condition 3)

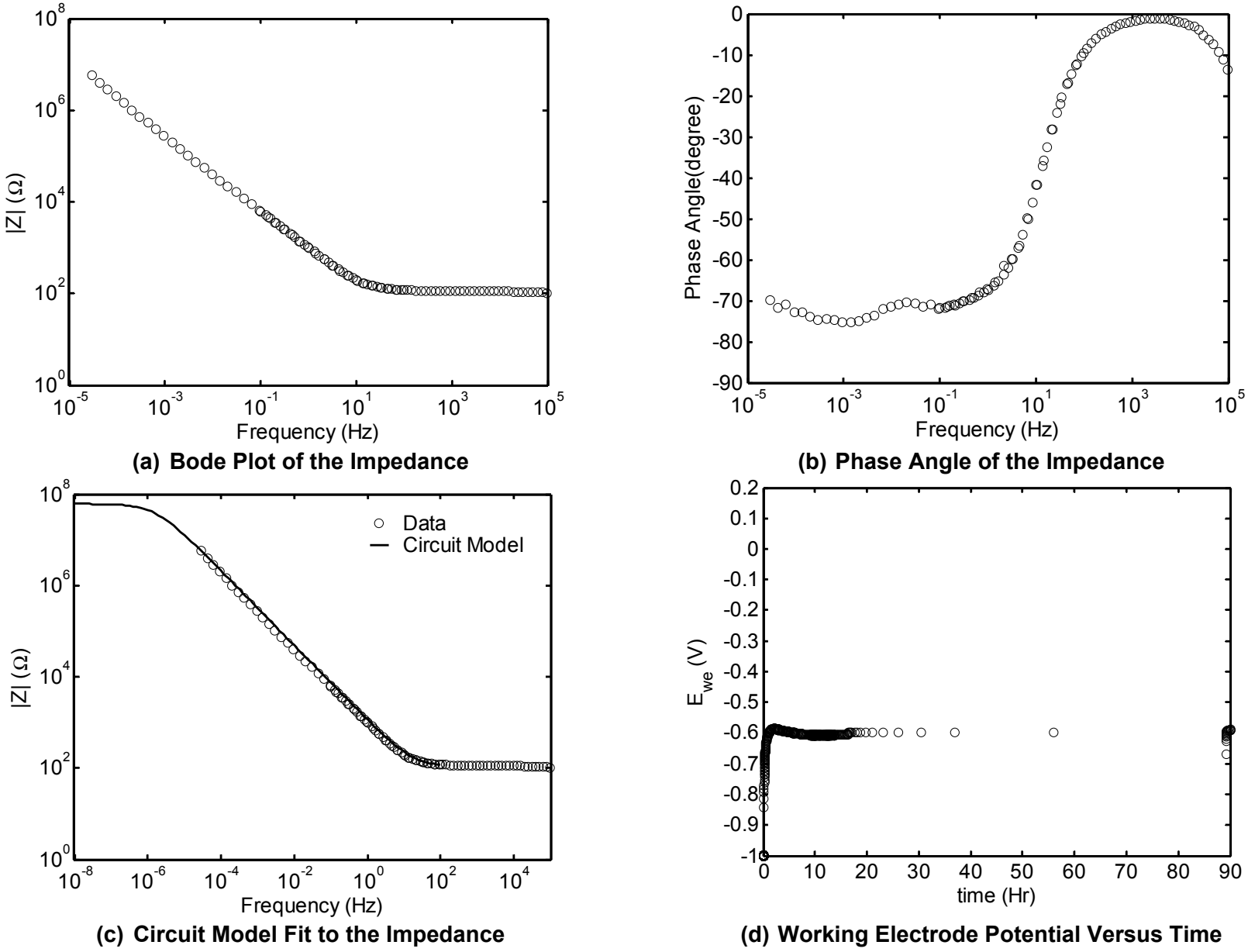

(a) Bode Plot of the Impedance

(b) Phase Angle of the Impedance

(c) Circuit Model Fit to the Impedance

(d) Working Electrode Potential Versus Time

Figure B–10. Electrochemical Impedance Spectroscopy, Circuit Model Fit to the Electrochemical Impedance Spectroscopy, and Working Electrode Potential Versus Time Data for 36 GW-day/MTU Burnup Equivalent SIMFUEL Electrode Under 130 psig of 4 Percent H_2 Plus 96 Percent N_2 (Condition 4)

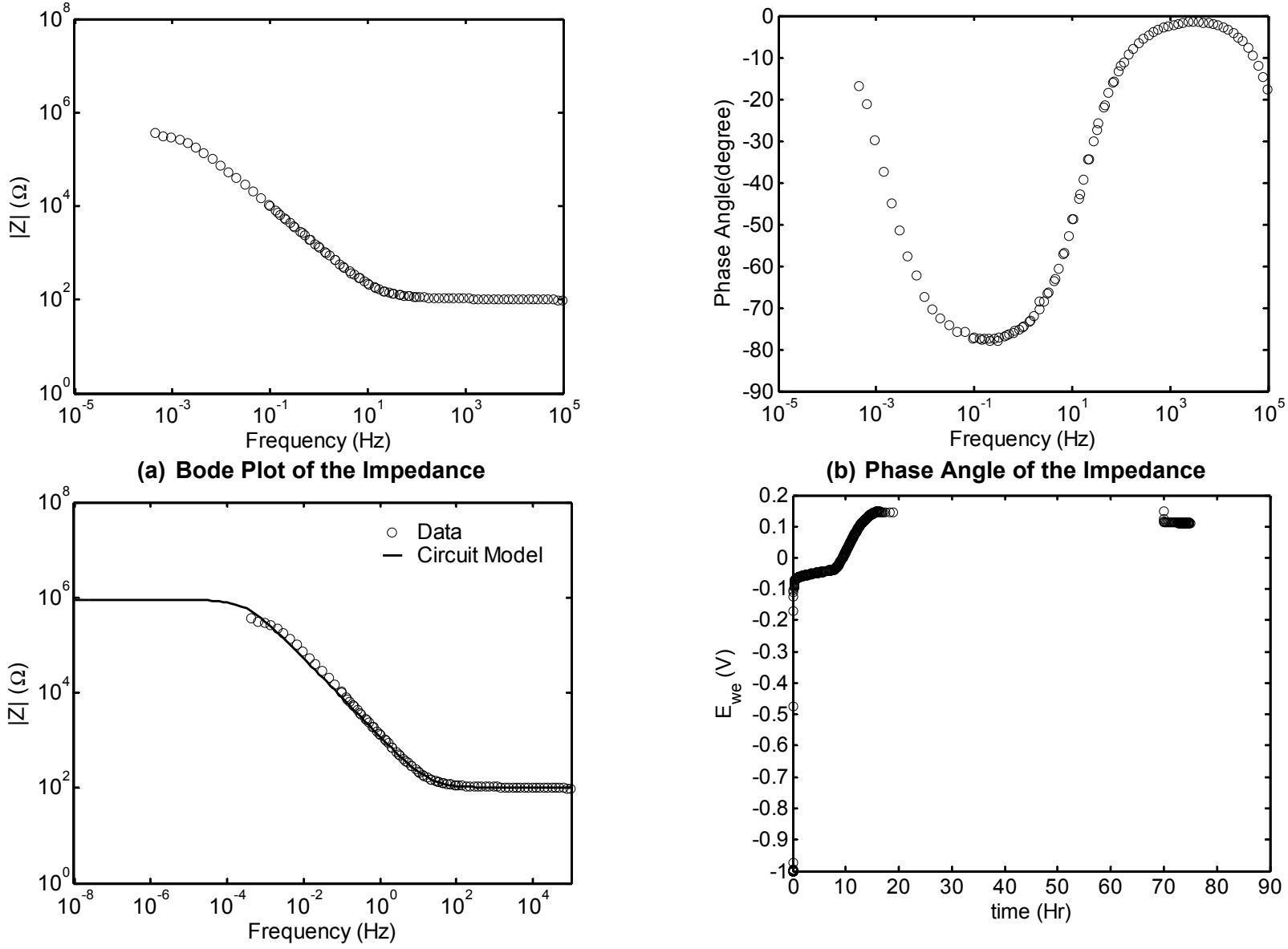

(a) Bode Plot of the Impedance

(b) Phase Angle of the Impedance

(c) Circuit Model Fit to the Impedance

(d) Working Electrode Potential Versus Time

Figure B–11. Electrochemical Impedance Spectroscopy, Circuit Model Fit to the Electrochemical Impedance Spectroscopy, and Working Electrode Potential Versus Time Data for 60 GW-day/MTU Burnup Equivalent SIMFUEL Electrode Under 15 psig Air and 130 psig of 4 Percent H_2 Plus 96 Percent N_2 (Condition 2)

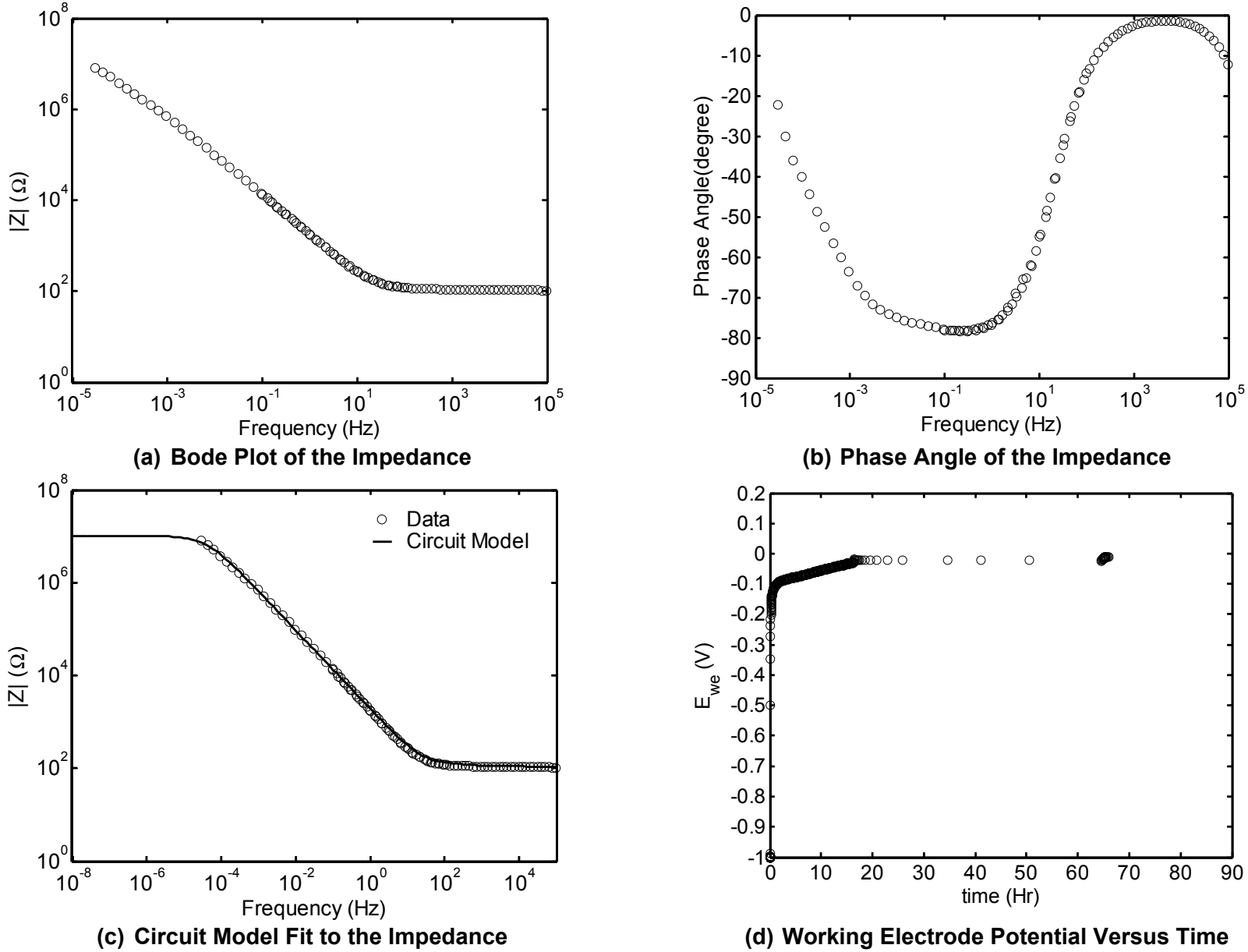

(a) Bode Plot of the Impedance

(b) Phase Angle of the Impedance

(c) Circuit Model Fit to the Impedance

(d) Working Electrode Potential Versus Time

Figure B–12. Electrochemical Impedance Spectroscopy, Circuit Model Fit to the Electrochemical Impedance Spectroscopy, and Working Electrode Potential Versus Time Data for 60 GW-day/MTU Burnup Equivalent SIMFUEL Electrode Under 10 psig Air and 15 psig of 4 Percent H_2 Plus 96 Percent N_2 (Condition 3)

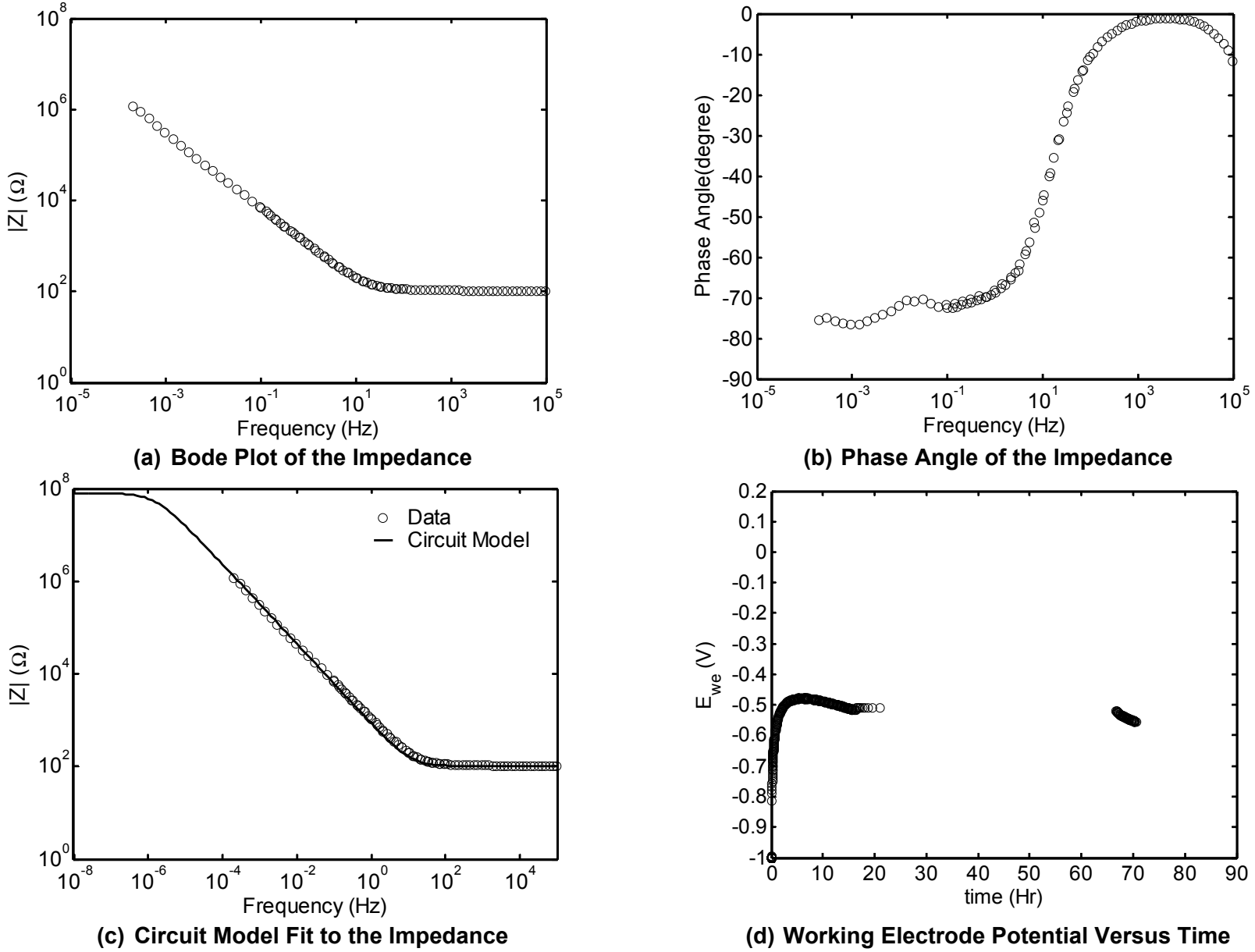

(a) Bode Plot of the Impedance

(b) Phase Angle of the Impedance

(c) Circuit Model Fit to the Impedance

(d) Working Electrode Potential Versus Time

Figure B–13. Electrochemical Impedance Spectroscopy, Circuit Model Fit to the Electrochemical Impedance Spectroscopy, and Working Electrode Potential Versus Time Data for 60 GW-day/MTU Burnup Equivalent SIMFUEL Electrode Under 130 psig of 4 Percent H_2 Plus 96 Percent N_2 (Condition 4, Run 1)

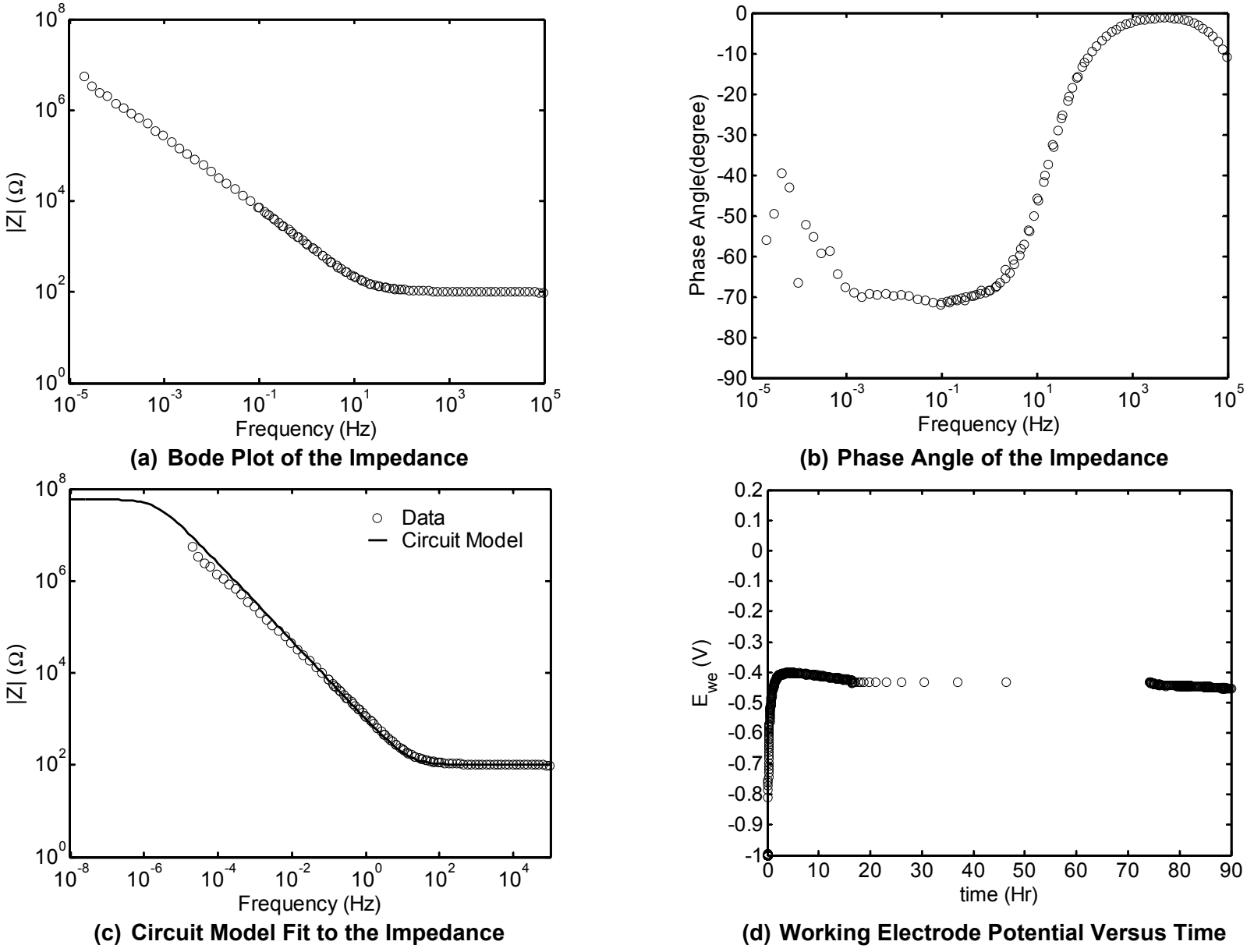

(a) Bode Plot of the Impedance

(b) Phase Angle of the Impedance

(c) Circuit Model Fit to the Impedance

(d) Working Electrode Potential Versus Time

Figure B–14. Electrochemical Impedance Spectroscopy, Circuit Model Fit to the Electrochemical Impedance Spectroscopy, and Working Electrode Potential Versus Time Data for 60 GW-day/MTU Burnup Equivalent SIMFUEL Electrode Under 130 psig of 4 Percent H_2 Plus 96 Percent N_2 (Condition 4, Run 2)

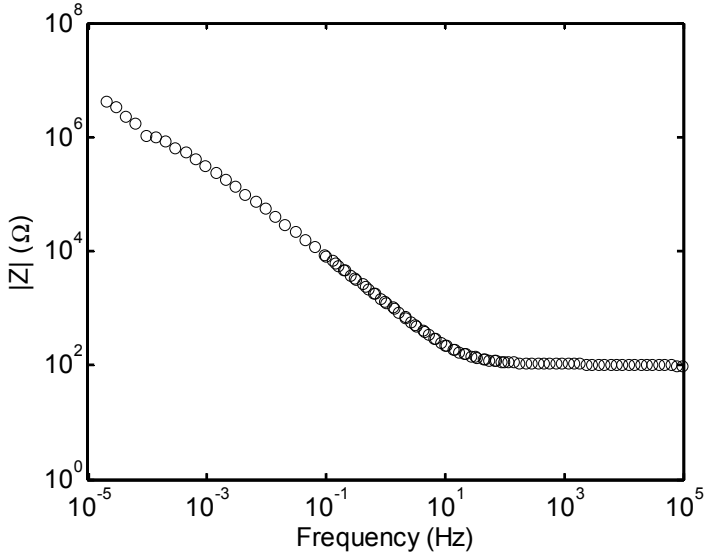

(a) Bode Plot of the Impedance

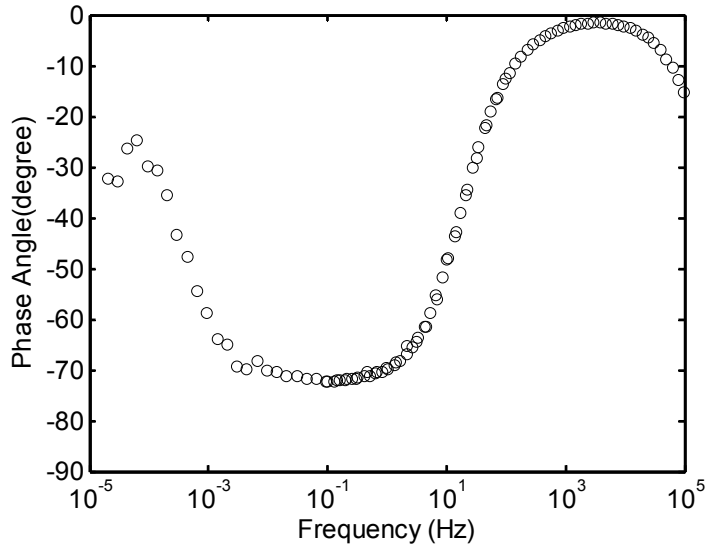

(b) Phase Angle of the Impedance

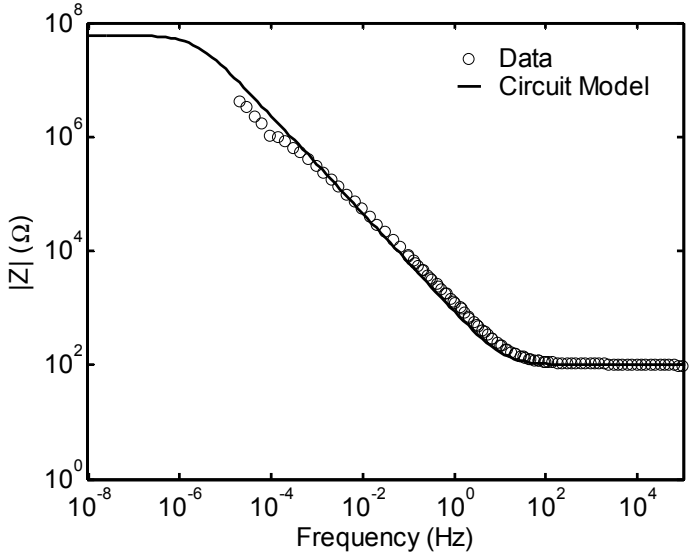

(c) Circuit Model Fit to the Impedance

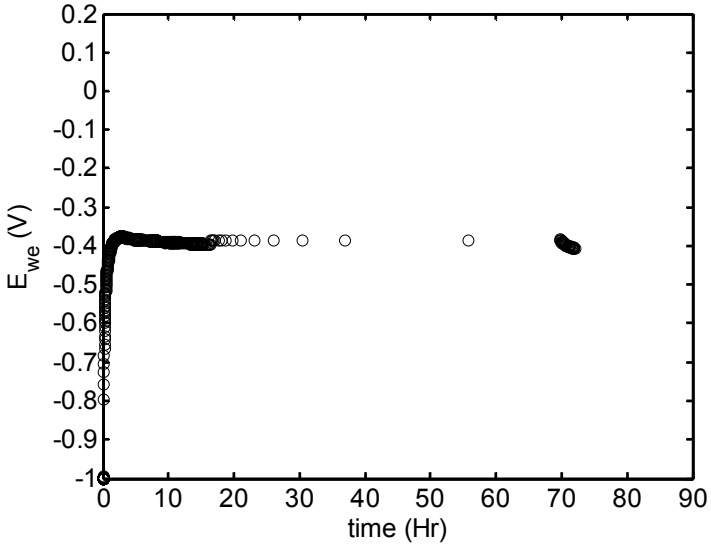

(d) Working Electrode Potential Versus Time

Figure B–15. Electrochemical Impedance Spectroscopy, Circuit Model Fit to the Electrochemical Impedance Spectroscopy, and Working Electrode Potential Versus Time Data for 60 GW-day/MTU Burnup Equivalent SIMFUEL Electrode Under 130 psig of 4 Percent H_2 Plus 96 Percent N_2 (Condition 4, Run 3)

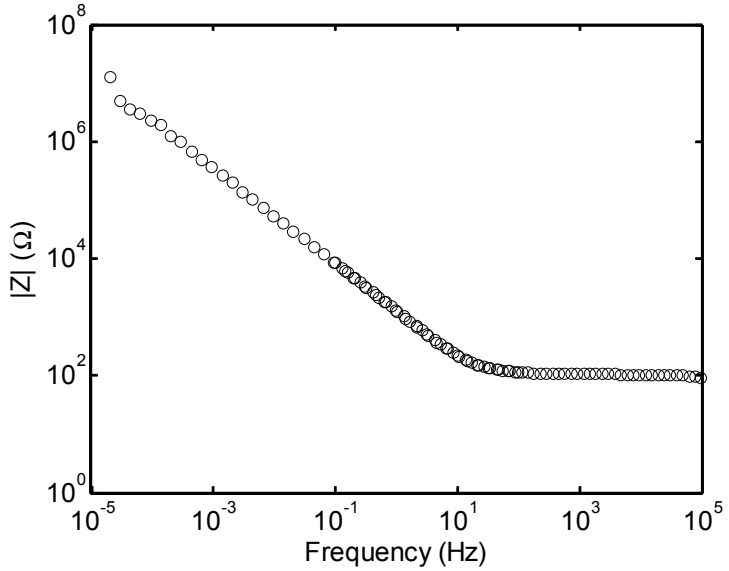

(a) Bode Plot of the Impedance

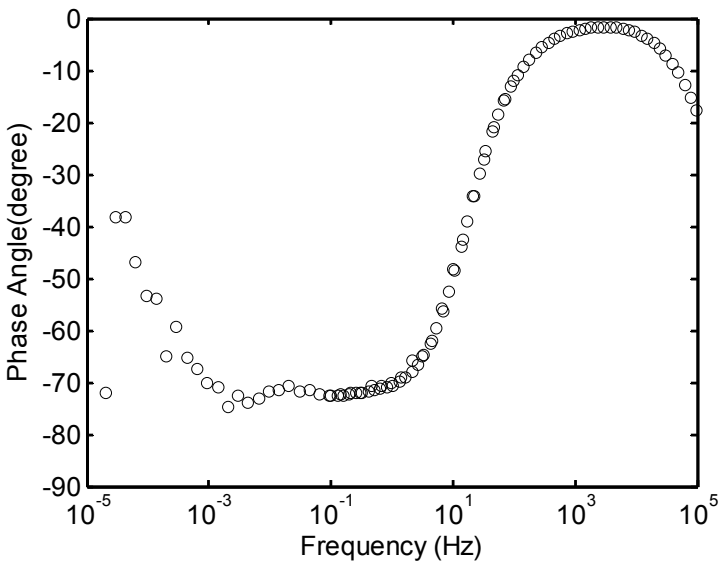

(b) Phase Angle of the Impedance

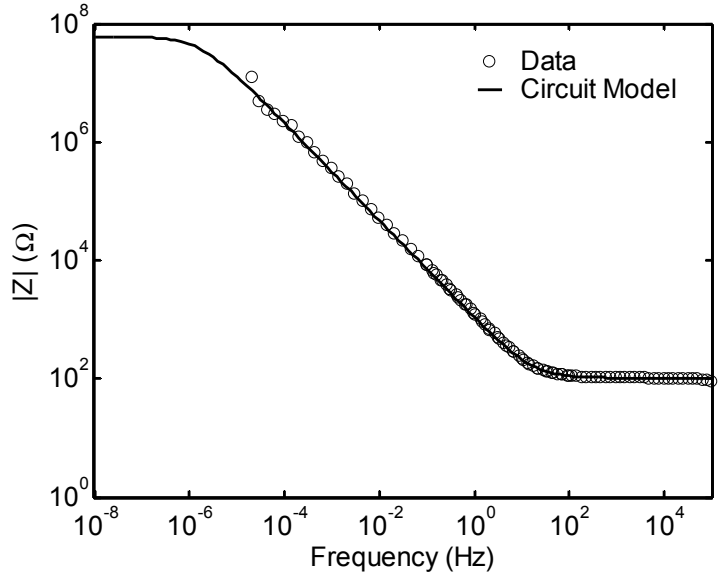

(c) Circuit Model Fit to the Impedance

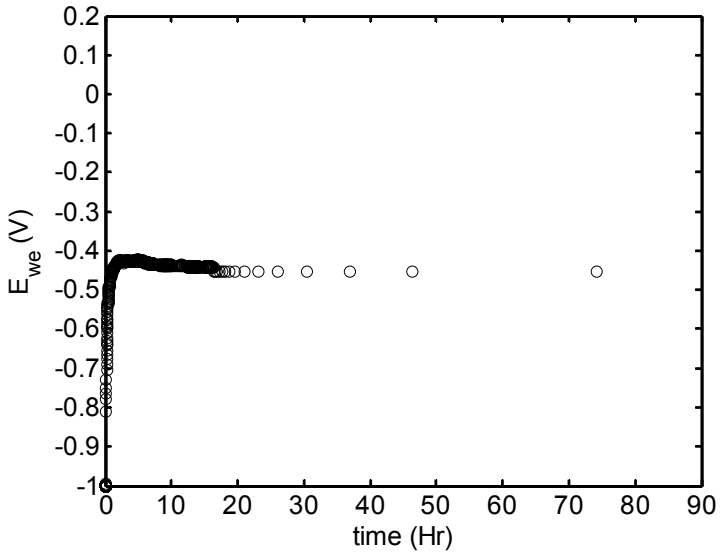

(d) Working Electrode Potential Versus Time

Figure B–16. Electrochemical Impedance Spectroscopy, Circuit Model Fit to the Electrochemical Impedance Spectroscopy, and Working Electrode Potential Versus Time Data for 60 GW-day/MTU Burnup Equivalent SIMFUEL Electrode Under 130 psig of 4 Percent H_2 Plus 96 Percent N_2 (Condition 4, Run 4)

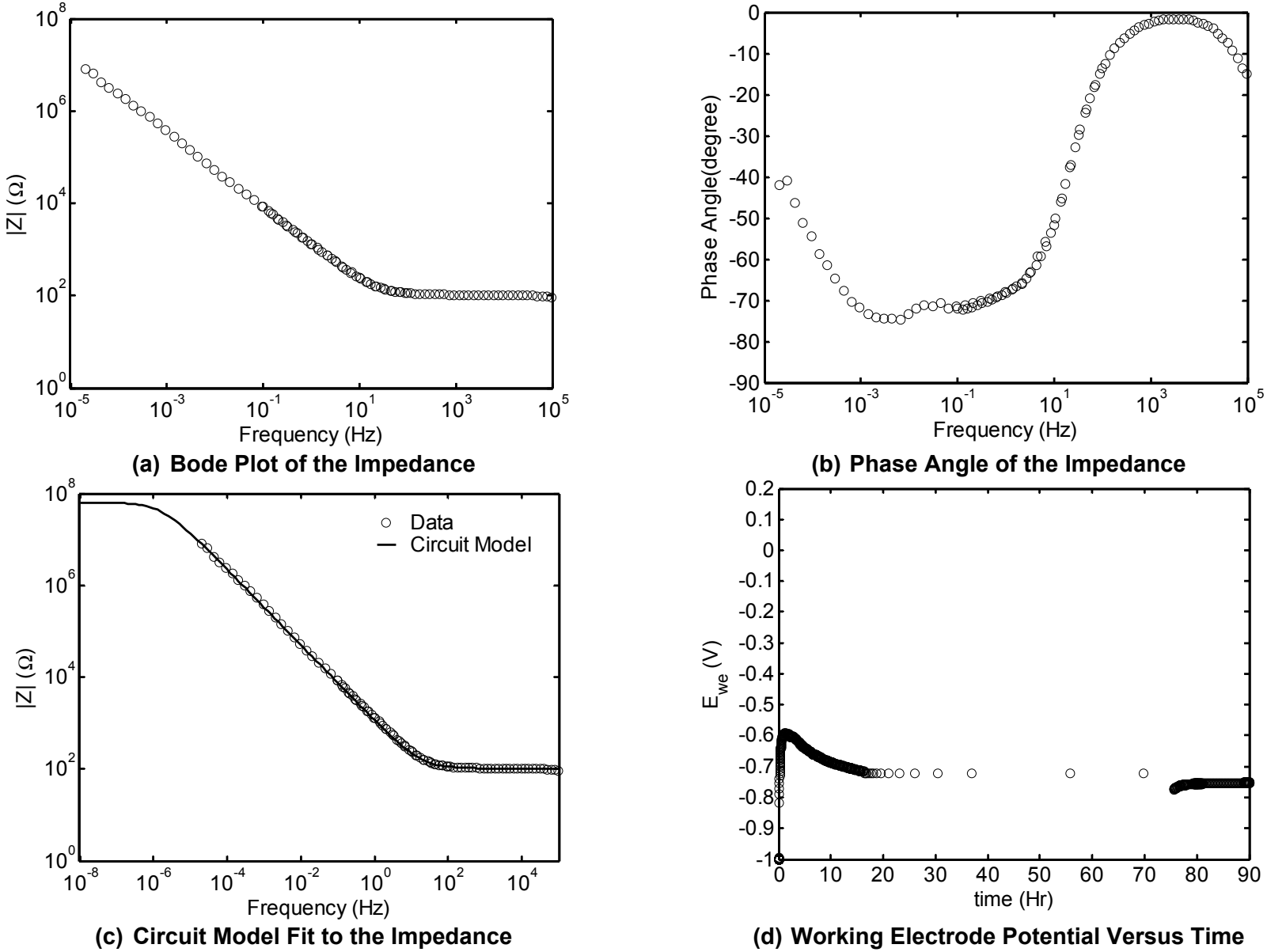

Figure B–17. Electrochemical Impedance Spectroscopy, Circuit Model Fit to the Electrochemical Impedance Spectroscopy, and Working Electrode Potential Versus Time Data for 60 GW-day/MTU Burnup Equivalent SIMFUEL Electrode Under 130 psig of 4 Percent H_2 Plus 96 Percent N_2 (Condition 4, Run 5)

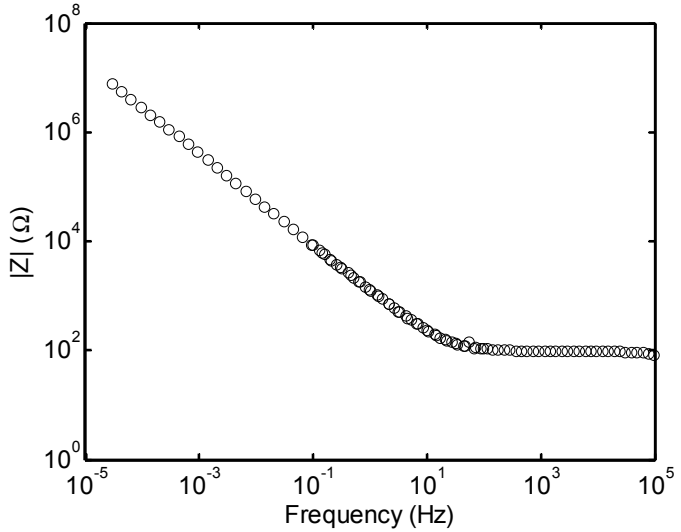

(a) Bode Plot of the Impedance

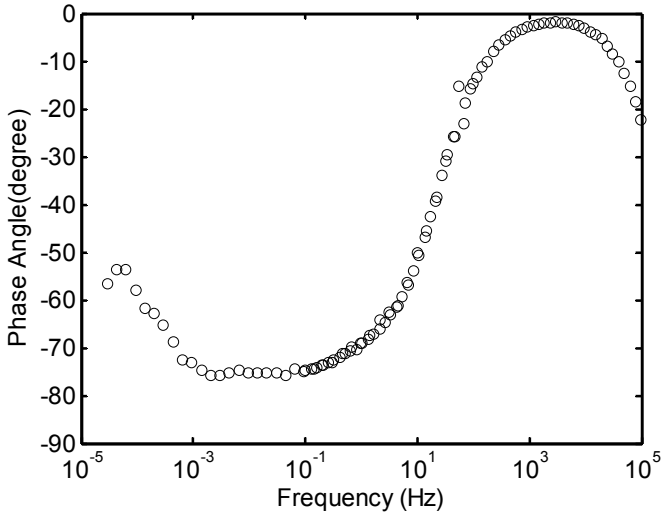

(b) Phase Angle of the Impedance

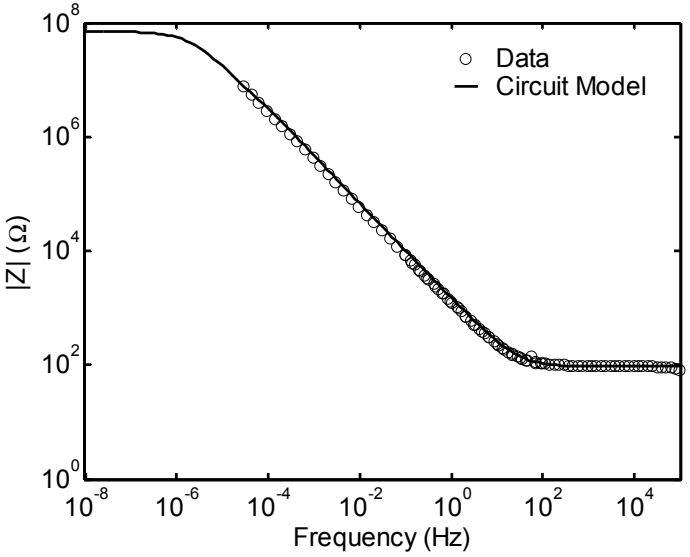

(c) Circuit Model Fit to the Impedance

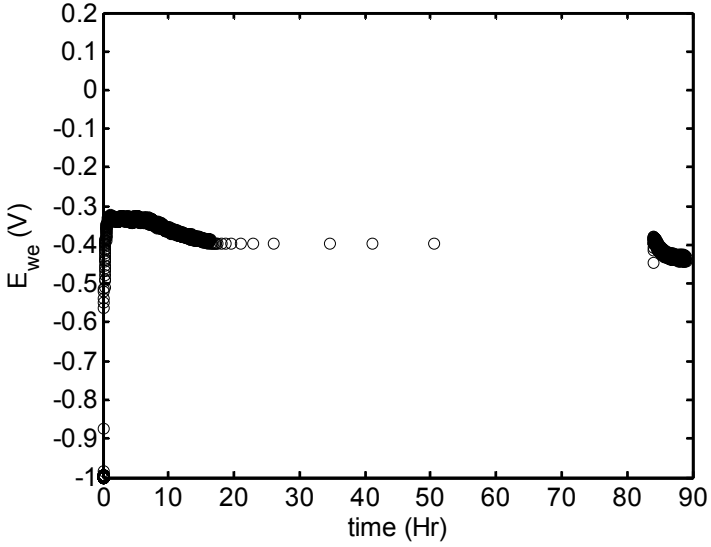

(d) Working Electrode Potential Versus Time

Figure B–18. Electrochemical Impedance Spectroscopy, Circuit Model Fit to the Electrochemical Impedance Spectroscopy, and Working Electrode Potential Versus Time Data for 60 GW-day/MTU Burnup Equivalent SIMFUEL Electrode Under 130 psig of 4 Percent H_2 Plus 96 Percent N_2 (Condition 4, Run 6)